Theoretical Investigations of Optical Polarizations in Chromophoric Aggregates and Nonlocal Charge Distributions in Clusters

A Thesis

Submitted For the Degree of

DOCTOR OF PHILOSOPHY

in the Faculty of Science

by

Ayan Datta

CHEMISTRY AND PHYSICS OF MATERIALS UNIT
JAWAHARLAL NEHRU CENTRE FOR ADVANCED SCIENTIFIC RESEARCH
Bangalore – 560 064

JULY 2006

To my mother

DECLARATION

I hereby declare that the matter embodied in the thesis entitled "**Theoretical Investigations of Optical Polarizations in Chromophoric Aggregates and Nonlocal Charge Distributions in Clusters**" is the result of investigations carried out by me at the Chemistry and Physics of Materials Unit, Jawaharlal Nehru Centre for Advanced Scientific Research, Bangalore, India under the supervision of Prof. Swapan Pati and that it has not been submitted elsewhere for the award of any degree or diploma.

In keeping with the general practice in reporting scientific observations, due acknowledgement has been made whenever the work described is based on the findings of other investigators.

Ayan Datta

CERTIFICATE

I hereby certify that the matter embodied in this thesis entitled "**Theoretical Investigations of Optical Polarizations in Chromophoric Aggregates and Nonlocal Charge Distributions in Clusters**" has been carried out by Mr. Ayan Datta at the Chemistry and Physics of Materials Unit, Jawaharlal Nehru Centre for Advanced Scientific Research, Bangalore, India under my supervision and that it has not been submitted elsewhere for the award of any degree or diploma.

Prof. Swapan Pati
(Research Supervisor)

Acknowledgements

Who we are is not only comprised of the knowledge we have gathered, but also those who have influenced us. Interdependence is as valuable as independence. I am lucky to have been influenced by many incredible and loving people and I express my gratitude to all of them.

First, I remember my family. Mom, thank you for teaching me to never give up, and for being so patient with my curiosity and my desire to take things differently. You got up at five in the morning, 365 days a year whether it was winter or summer for making tiffin for my school. You would stay awake till midnight to make sure that I had put the mosquito net. Dad and brother thank you for sparking my interest in science.

I would like to thank my supervisor, Dr. Swapan K. Pati for all the support, knowledge and encouragement that he has bestowed upon me. During these years I have known Dr. Pati as a principle-centered person. His overly enthusiasm and integral view on research and his urge for providing 'only high-quality work and not less', has made a deep impression on me. The independence and freedom that he has provided me in my work has helped me grow up from a novice to a research worker. He has been very understanding and caring and it has been a wonderful experience working with

him. Besides of being an excellent supervisor, Swapan has been as close as a relative and a good friend to me. I would also thank Anusooya, his wife for being a very helpful and encouraging person.

I thank Prof. C. N. R. Rao, F. R. S, the Chairman of CPMU for all the support and motivation. Whenever I listen to his lectures and talks, I feel rejuvinated and start loving science even more.

I would like to thank all my Integrated Phd. course instructors. I particularly thank Prof. K. L. Sabastain for making contour integrals so easy. I would like to thank Prof. Uday Maitra and Prof. S. Natarajan, the convenors of the Int. Phd course for helping me decide the field of my interest. Also I thank Prof. S. Sastry, Prof. S. Narasimhan, Dr. U. Waghmare for the physics courses. I thank Prof. G. U. Kulkarni for teaching me Hydrogen-bonding and organic crystals. I thank Prof. K. S. Narayan for teaching me how to "attack" a spectra or an experimental result.

I would like to thank Prof. Debashis Mukherjee from *Indian Association for the Cultivation of Science, Kolkata*, Prof. Sourav Pal from *National Chemical Laboratory, Pune*, Prof. T. P. Radhakrishnan *University of Hyderabad* and Prof. Anna Painelli *University of Parma, Italy* for accomodating me in their labs during my brief visits. I also thank Dr. K. K. Rajak *Jadavpur University* for collaboration on H-bonded superexchange systems.

It is a pleasure for me to thank the students with whom I have collaborated on various problems. Thanks to Neena, Daly and Abdul for their cooperation. Special thanks to Daly for being a very good friend.

I have been fortunate to be a part of a very dynamic and friendly environment in my research group. Thanks to Lakshmi, Debu, Sairam, Sudipta,

Sasmita and Mohan for friendly discussions.

I want to thank my friends and everyone else who have helped me along my journey. I thank Prof. Bholanath Mukherjee from my college, Ramakrishna Mission for encouraging me. Kalyan, Arnab, Animesh, Tirthankar, Rudra, Subhas, Tinku and Jana thanks for discussion for the assignments during coursework at IISc. Samrat, you have taught me how to madly love science and I will always remember your attitude towards science and life as such. Partha and Sukhendu, you have been really good to me. I would also like to thank Vivek for the bread toast-omelette breakfasts in the coursework days. I thank Shrinwantu, Shampa, Rahul, Sutirh, Snigdha, Prasenjit, Mousumi, Joydeep, Bhaswati, Moumita, Gargi, Motin, Ashish, Soumya, Ved, Dinesh, Partha, Dhritiman, Meenakshi, Thiru and Vijay for their friendship.

Synopsis

Materials exhibiting large linear and nonlinear optical polarizations are a subject of great interest due to their many potential applications. In this thesis, I have investigated the factors that control such polarizations in the molecular and supramolecular levels. The main emphasis has been to understand the role of weak intermolecular forces like the dipole-dipole, hydrogen-bonding and π-stacking interactions, in controlling the overall polarization responses in such class of materials. Another major theme that has been considered in the thesis is the modeling of the structures and optical properties of various metallic clusters. We have devised strategies to stabilize various metallic clusters through the inorganic route.

The thesis is divided into eight chapters.

The first chapter provides a brief introduction to linear and nonlinear polarizations and their various potential applications. The design of molecular and supramolecular materials possessing high laser damage thresholds with high dielectric constants and fast laser response time have been discussed. Various strategies are discussed for enhancement of the polarization responses in macromolecular aggregates like organic crystals and thin-films structures. A number of computational techniques are also outlined for the calculation of

the static and dynamic electric field induced linear and non-linear response functions.

In the second chapter, a theory is developed based on dipole- dipole interactions to determine the excitation spectra of multichromophoric aggregates in various orientations of the monomers. Numerical calculations are performed on dimers of D-π-A systems like paranitroaniline and their derivatives in various modes of arrangements to quantify the proposed analytical theory. We predict that the head-to-tail arrangement of the dipoles in the aggregate leads to the maximum enhancement in the second harmonic responses (β). Additional H-bonding interactions between the monomers further increases the polarization responses.

The third chapter aims at providing a quantitative estimation of the role of dipolar and H-bonding interactions in controlling the polarization responses in molecular aggregates. These two forces have been optimized for the $(HX)_n$ aggregates (X=F, Cl and Br). It is found that for the strong H-bonded clusters like the $(HF)_n$, planar cyclic rings are formed leading to very small β. However, for H-bonds of intermediate strengths, non-centric structures are formed with appreciable β value. Similar conclusions are also derived from the calculation of β for the linear chains of $(HF)_n$ aggregates. The main inference from this chapter is that the H-bonding in the intermediate energy scales with appropriate directionality will lead to cooperative enhancement in β.

The fourth chapter deals with the conformational orientations of dipolar molecules that are connected through alkane chains which result in confined geometries. Systems like calix[3]arenes provide a nice example to study the

role of dipolar frustration in the odd-membered chromophoric aggregates. The calculations performed on calix[3]arenes suggest that, while the β-value decreases monotonically with increase in the cone-angle of the all-parallel calix[3]arenes, it increases with increase in the cone-angle for the frustrated geometries. Molecular structures as retrieved from the structural database support our conclusions with cone-angle as the unique parameter.

The fifth chapter discusses the variation in β for the dipolar aggregates which are connected by flexible spacers. The specific dipolar orientations are considered for oxo-bridged paranitroaniline dimers (PNA-O-PNA) for a quantitative estimation of dipolar interactions. We suggest molecular systems where the maximum polarization responses can be attained by 'conformationally locking' the dimers through C-C bridges. Additionally, the origin of the odd-even oscillations in the second harmonic generation responses in alkyl bridged di-chromophores are also discussed. A simple theory based on the conformational flexibility of the alkane chains is provided to explain the oscillations in β for these systems. It is shown that for the dipoles connected by even spacers, there is a cancellation of the dipole moment together with β, due to the staggered conformation of alkane chains. However, when the number of spacers are odd, the dipoles have an eclipsed conformation which leads to addition of the dipole vectors with appreciable β.

The sixth chapter compares and contrasts the conventional π- conjugated systems with the all-metal molecular systems like Al_4Li_4 for their nonlinear optical responses. It is shown that the all-metal clusters exhibit polarizations that are orders of magnitude higher than their organic counterparts of similar sizes. This arises primarily due to the poor σ-π separation in the all-metal

molecules which remarkably reduces the optical gap for the all-metal Al_4Li_4 systems. The strong charge-transfer from the alkali metals to the Al_4 ring further enhances the transition dipole moment.

The seventh chapter provides a methodology for separating the σ and π energies in the ground state structures for clusters. Through this method, we are able to assign the overall aromaticity/antiaromaticity within all-metal systems. The method is also utilized to study the σ electron delocalizations in a σ-only clusters like the $(Li)_n$ systems. The $(Li)_n$ clusters exhibit odd-even oscillations in their binding energies as a consequence of frustration and pairing up of the σ electrons for the odd and even membered $(Li)_n$ clusters, respectively. A simple Heisenberg-spin Hamiltonian qualitatively explains the odd-even oscillations in magnetic binding energies.

In the final chapter, strategies are proposed for the possible synthesis of all-metal antiaromatic compounds through the organometallic route like complexations of transition metal ions. Complexation of the 4π Al_4Li_4 clusters with low-valent transition metals like Fe(0) and Ni(0) facilitates metal-to-ligand charge transfer leading to an addition of two extra π-electrons to the Al_4Li_4 rings and making it aromatic. Substitution reactions are also proposed within the conventional sandwich complexes wherein the organic molecules can be replaced by the all-metal systems. We find that, while for the half-sandwich complexes, $(Al_4M_4)Fe(CO)_3$ (M=Li, Na and K), direct substitutions are highly exothermic, for the full-sandwich complexes, $(Al_4M_4)_2$-Ni, the substitution reaction proceeds through a hybrid organic-inorganic intermediate, $(Al_4M_4)Ni(C_4H_4)$ which makes it suitable for synthesis.

Nomenclature

e : Electron

ω : Frequency of applied field

χ : Optical Susceptibility

η : Refractive Index

α : Linear Polarizability

β : First order Hyperpolarizability

γ : Second order Hyperpolarizability

μ : Dipole Moment

$\hbar$: Planck's Constant

ρ : Charge-Density

NICS : Nucleus Independent Chemical Shift

J: Exchange Coupling

RCP: Ring Critical Point

au: Atomic Unit

B3LYP: Becke exchange + 3-parameter Lee-Yang-Parr correlation

H-bonding: Hydrogen Bonding

Contents

List of Figures

List of Tables

Chapter 1

Introduction to linear and nonlinear optical polarizations in molecules and aggregates

1.1 Introduction

A material undergoes distortion when exposed to an external electric field. The atoms develop a separation of charges that leads to creation of instantaneous dipoles which tend to counteract the external field. The electromagnetic radiation thus induces a forced separation of the charges. This leads to a dipolar oscillation in the system, which emits radiation of the frequency of its oscillation. Thus, as the wave field travels through the medium, it induces polarization whose oscillation launches an electromagnetic wave of its own. Since, there can be an out-of-plane component to this new wave, the net result is a phase shift in the emerging wave. This phase shift is the

index of refraction of the material.

Under this external influence, the material becomes polarized with an induced dipole moment. Each constituent molecule of the material acts as a dipole with a dipole moment P_i. The dipole moment vector per unit volume P is given by

$$P = \sum_i P_i \tag{1.1}$$

where the summation is over the dipoles in the unit volume. The induced polarization in a material depends on the strength of the electric field. For a weak field, one can write the polarization as

$$P = \chi E \tag{1.2}$$

where, χ is called the *polarizability* of the medium. The polarizability is related to the dielectric constant (ϵ) of the medium by

$$\epsilon = 1 + 4\pi\chi \tag{1.3}$$

From an atomistic viewpoint, the electric field distorts the electron distribution of an atom or molecule. Thus the molecular polarization can be written as

$$\mu_i = \alpha E \tag{1.4}$$

Here, α corresponds to the polarizability of the atom or molecule. The polarizability of a system is directly proportional to the number of charges present in it.

The wavelike properties of light are described by an oscillating electromagnetic field, *E(r,t)*. Consequently, the material response P, and its linear susceptibility are also time and space varying quantities. Thus, the previous equation (1.2) modifies to

$$P(r,t) = \sum_{r_i} \chi_{rr_i} E(r_i, t) \tag{1.5}$$

It can be seen that the polarization can be induced in a different direction to that of the applied field. This occurs because of the tensorial nature of the polarizability.

1.2 Nonlinear Optical Processes

However, a large number of new phenomena emerged with the invention of Lasers. With sufficiently intense laser radiation, the previous relations require modification. The bulk polarization P, for a strong external field is then defined by a phenomenological power series expansion in terms of the applied electric field as [1–3]:

$$P = \chi^{(1)}E + \chi^{(2)}EE + \chi^{(3)}EEE + \dots \tag{1.6}$$

Here, $\chi^{(n)}$ is the *n*th-order susceptibility of the medium and E represents the total electric-field experienced by the system. The nth-order susceptibility is a tensor quantity of rank (n+1) which has 3^{n+1} elements [4]. Thus, $\chi^{(1)}$ is a second-rank tensor with nine elements, $\chi^{(2)}$ is a third-rank tensor with twenty-seven elements, $\chi^{(3)}$ is fourth-order tensor with eighty-one elements,

and so on. This number is, of course, drastically reduced by symmetry requirements as not all elements are linearly independent and in most practical materials much fewer elements are required to describe the tensor. Thus, at a strong electric field, the optical characteristics of a medium, such as dielectric permittivity and refractive index etc., which depend on the susceptibility, also become a function of the electric field E [5–8].

The possibility of exploiting a monochromatic light beam for the production of nonlinear optical phenomenon was first experimentally shown by Frenken *et al* [9]. They observed ultraviolet light at twice the frequency of a ruby laser (λ=6493 $\mathring{A}$), when the light was made to traverse through a quartz crystal. Also, at the same time there were reports of multi-photon absorption processes through which one could access high energy states that are otherwise forbidden by dipolar transitions, with relatively low-energy photons [10].

These experiments attracted huge attention from the science community and marked the beginning of a rich field called *Nonlinear optics* [11, 12]. The field witnessed a tremendous growth with the development of newer lasers [13,14]. The evolution of lasers from their predecessors, the microwave beam and and the solid state masers, have been due to the phenomenal contribution by Townes, Basov and Prokhorov (they were awarded Nobel prize in 1964 for their discovery of laser) and N. Bloembergen (he was awarded the Noble prize in 1981). In short, lasers are sources of coherent light, characterized by a high degree of monochromaticity, high directionality and high intensity or brightness. With dye lasers, it is possible to cover the range of wavelengths from 350-950 nm continuously, including the whole visible

spectrum. A variety of nonlinear processes, including harmonic generation, extend the range of coherent sources throughout the infrared and into the vacuum ultraviolet.

Nonlinear optical (NLO) phenomena encompasses a broad range of light mediated processes like second harmonic generation, electro-optic Pockels effect, optical rectification, third harmonic generation, optical Kerr effect and intensity dependent refractive index. It should be noted that the nonlinear optical processes were observed even before the discovery of lasers. Processes like the optical Kerr effect and the Pockels effect have been known for a very long period of time.

When an isotropic liquid comprising of asymmetric molecules (like nitrobenzene) is placed in an electric field, the molecules tend to align themselves parallel to the direction of the field. Because the molecules are not symmetrical, the alignment causes the liquid to become anisotropic and as a result bifringent. Thus, a light wave which enters the liquid, splits into two waves traveling at two different velocities with two different refractive indices. Thus the refractive index of a material can depend on the strength of the applied electric field. This is known as an *electro-optic effect*. The first order electro-optic effect (observed in crystals of KH_2PO_4) is known as Pockels effect. It is linear in the ac-field. The quadratic process is called the Kerr effect. A Pockels cell, usually requires a small voltage of 1-5 kV while a Kerr cell requires a high voltage of 10-20 kV.

The manifestation of the nonlinear optical behavior can be clearly seen by substituting a sinusoidal field $E = E_0 + E_1 \cos \omega t$ into the polarization. Substituting this in the previous equation (1.6) gives:

$$P = (E_0 + E_1 \cos\omega t)\chi^{(1)} + (E_0 + E_1 \cos\omega t)^2\chi^{(2)} + (E_0 + E_1 \cos\omega t)^3\chi^{(3)} + \ldots \quad (1.7)$$

Rearranging the equation,

$$P = (\chi^{(1)}E_0 + \chi^{(2)}E_0^2 + \chi^{(3)}E_0^3) + (\chi^{(1)}E_1 + 2\chi^{(2)}E_0E_1 + 3\chi^{(3)}E_0^2E_1)\cos\omega t + (\chi^{(2)}E_1^2 + 3\chi^{(3)}E_0E_1^2)\cos^2\omega t + (\chi^{(3)}E_1^3)\cos^3\omega t + \ldots \quad (1.8)$$

Using the trigonometric relations, $\cos^2\omega t = (1 + \cos 2\omega t)/2$ and $\cos^3\omega t = (\cos 3\omega t + 3\cos\omega t)/4$, one gets

$$P = \chi^{(1)}[E_0 + E_1\cos\omega t] + \chi^{(2)}[E_0^2 + (1/2)E_1^2 + 2E_0E_1\cos\omega t + (1/2)E_1^2\cos 2\omega t] + \chi^{(3)}[E_0^3 + (3/2)E_0E_1^2 + 3E_0^2E_1\cos\omega t + (3/4)E_1^3\cos\omega t + (3/2)E_0E_1^2\cos 2\omega t + (3/4)E_1^3\cos 3\omega t] + \ldots \quad (1.9)$$

The 1st term in the brackets for all $\chi^{(n)}$ are constant factors. They give rise to a dc field across the medium.

1.3 Second-Order Optical Processes

Now let us consider the processes associated with the $\chi^{(2)}$ in details. From eqn (1.9)

$$P^{(2)} = \chi^{(2)}[E_0^2 + (1/2)E_1^2 + 2E_0E_1\cos\omega t + (1/2)E_1^2\cos 2\omega t] \tag{1.10}$$

The coefficient E_0E_1 corresponds to the linear electro-optic effect and is represented as $\chi^{(2)}$(-ω;ω,0). The sign attached to a frequency is negative if the photon is emitted and positive if it is absorbed. The last term which is square in the ac-electric field and and has a frequency of 2ω is known as the second harmonic generation (SHG) process. Considering that two coherent light waves of unequal frequencies ω_1 and ω_2 are traveling in the material, the 2^{nd} and 4^{th} terms from the previous equation (1.10) become

$$\chi^{(2)}(1/2)E_1^2[\cos(\omega_1 - \omega_2)t + \cos(\omega_1 + \omega_2)t] \tag{1.11}$$

Thus, one now has two new frequencies $(\omega_1 + \omega_2)$ and $(\omega_1 - \omega_2)$. This phenomenon is known as *optical mixing*. While, $\omega_1 + \omega_2$ is called the sum-frequency generation (SFG), $\omega_1 - \omega_2$ is called the difference-frequency generation (DFG). The second harmonic generation (SHG) process, actually, is a special case of SFG where the frequencies of the photons from the incident beams are equal ($\omega_1 = \omega_2$). Similarly, *optical rectification (OR)* is a special case of DFG for $\omega_1 = \omega_2$. Thus the OR susceptibility is represented as $\chi^{(2)}$ (0;ω,-ω).

A solution or a glass, in its natural form being random, does not exhibit

any second-order effect. For biological systems, important second- order effects are associated with the interface and with electric field poling. Surface induced second harmonic generation from a biological membrane provides a powerful method for second-harmonic imaging for selectively probing interactions and dynamics involving membranes. The electric-field- induced second harmonic generation provides an excellent probe for membrane potentials and has been found to be very promising for use in *bio-imaging* [15, 16].

1.4 Symmetry Requirement for Second-Order Processes

In 1962, it was proposed by Kleinman that in many nonlinear processes, where all the interacting frequencies are far away from resonances, energy is simply exchanged between the fields and not dissipated in the medium [17, 18]. This amounts to the susceptibility tensors being invariant under any permutation of their Cartesian indices. For instance, in the $\chi^{(2)}$, the symmetry relations give rise to:

$$\chi^{(2)}_{ijk} = \chi^{(2)}_{ikj} = \chi^{(2)}_{jik} = \chi^{(2)}_{jki} = \chi^{(2)}_{kij} = \chi^{(2)}_{kji} \tag{1.12}$$

Thus, due to Kleinman symmetry relations, the number of independent components of $\chi^{(2)}$ reduces from 27 to 10 and that of $\chi^{(3)}$ from 81 to 15.

For a medium to exhibit frequency conversion processes mediated by $\chi^{(2)}$, the medium must have nonzero $\chi^{(2)}$. This condition requires that at a molecular level the nonlinear coefficient, β, must be nonzero. Furthermore, the

orientationally averaged sum of β at all sites that gives rise to the macroscopic $\chi^{(2)}$ should not be zero. These two conditions lead to the following symmetry requirements for the realization of $\chi^{(2)} \neq 0$:

1. For noncentrosymmetric molecules (without any inversion symmetry), β-being an odd rank (3^{rd} rank) tensor, is not zero.

2. The molecules in the bulk form are arranged in a noncentrosymmetric structure. Only then the overall $\chi^{(2)}$ is non-zero.

A molecular design often uses systems like D-π-conjugation-A where a molecular unit involving π-conjugation is connected to an electron donor, D (such as -NH_2), at one end and an electron acceptor group, A (such as -NO_2), to the other end. A classic example of such a system is *para*-nitroaniline. Extensive calculations have been performed on this molecule over the years, since it serves as a model for understanding many NLO phenomenon [19–21].

1.5 Methodologies for preparing a noncentrosymmetric crystal

.

Lot of efforts in the last two decades have been directed towards understanding and controlling the factors that may lead to an acentric crystal with large NLO response functions. It is quite a non-trivial task to arrange molecules in a noncentrosymmetric fashion in the crystal. It requires a combination of chemical intuition, theoretical understanding of intermolecular forces as well as very sound crystal engineering to tailor molecules for such

applications.

D-π-conjugated-A molecular systems show large NLO responses because of the delocalized nature of the π-electrons resulting in low-energy excitonic levels with high oscillator strength. However, these dipolar molecules tend to pack in an anti-parallel arrangement in the crystal, thereby, making the SHG response for the whole crystal almost zero. This drawback has led to search for other molecular materials. The most important of such molecules has been the 3-methyl-4-nitropyridine-1-oxide (POM) shown in Fig 1.2 (a). For this molecule, there is a cancellation of the ground state dipole moment as the dipole moments for the pyridine-1-oxide and the nitrobenzene fragments are equal and opposite. So, the molecules have no urge to crystallize in anti-parallel arrangements. However, for such a system, even though the ground state dipole moment is zero, the excited states are dipolar in nature. Such molecules thus exhibit large β values. The crystal for POM has been found to exhibit a substantial $\chi^{(2)}$ (about two times that of $LiNbO_3$).

In 1993, Zyss et al. have shown that molecules with *octupolar* moments are very promising candidates for NLO applications in crystals [22–24]. For these molecules, even though the ground state dipole moment is zero, the higher order multipoles like the octupolar moment is non-zero. Very similar to that for POM, these molecules also have a non-centrosymmetric arrangements in the crystal structure. Such a molecule exhibiting large octupolar moment is shown in Fig 1.2 (b).

Another way of ensuring noncentrosymmetricity in a crystal is the incorporation of chiral substituents in the molecular structure. Optically pure

Figure 1.1: Molecules which exhibit significant $\chi^{(2)}$ in the bulk crystal.

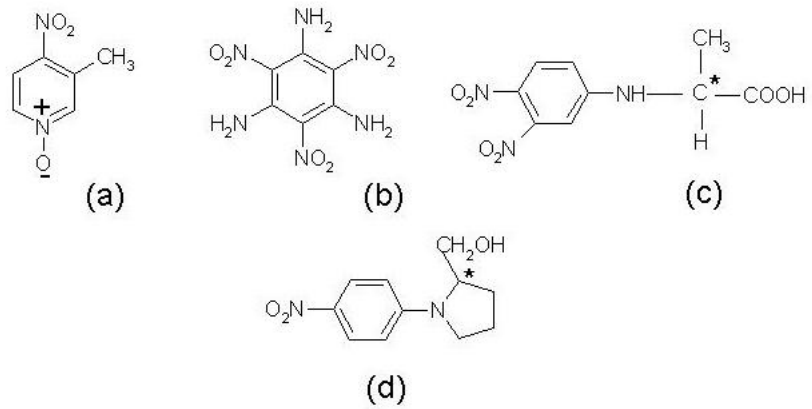

material, compounds which have only left-handed and/or right handed symmetry, are inherently non-centrosymmetric. Such compounds are, in fact, readily available in the nature (amino acids, sugars and alkaloids are well known examples existing only in a single enantiomer). Thus, crystals of these materials are expected to be NLO active. Some of the best known examples are, methyl-2-(2,4-dinitroanilino)-propionate (MAP) and and *N*-(4-nitrophenyl)-*L*-prolinol (NPP). They are shown in Fig 1.2 (c) and Fig 1.2 (d) respectively.

1.6 Third-Order Optical Processes

The third-order polarization component from equation (1.9) has the form

$$P^{(3)} = \chi^{(3)}[E_0^3 + (3/2)E_0E_1^2(1 + \cos 2\omega t) + 3E_0^2E_1 \cos \omega t + (3/4)E_1^3(\cos \omega t + \cos 3\omega t)] \tag{1.13}$$

The $E_0^2E_1$ term corresponds to the dc Kerr effect; the $E_0E_1^2$ term is the ac Kerr effect or the optical Kerr effect and is represented as $\chi^{(3)}$(-ω; 0,0,ω). The E_1^3 term describes third harmonic generation (THG) response. THG is a special case of four wave mixing, which in general can be written as:

$$\chi^{(3)}(-\omega_\sigma; \omega_1, \omega_2, \omega_3)E(\omega_1)E(\omega_2)E(\omega_3) \tag{1.14}$$

where three photons with frequencies, ω_1, ω_2 and ω_3, result in a fourth frequency of ω_σ. For ω_1= ω_2= ω_3, the $\chi^{(3)}$ medium generates a new photon of frequency 3ω. Thus, an incident fundamental light of wavelength at 1064 nm (from an Nd:YAG laser) will produce a third harmonic beam at 355 nm in the UV region. Again, like in the case of second- harmonic generation, it is a coherent process with three incident frequencies and there is no resonance associated with it. Some important processes in nonlinear optical spectroscopy are shown in Table. 1.1.

Table 1.1: Some important processes involving Nonlinear Optical Spectroscopy.

Process	Order	Frequency Relation
Linear Response	1	-ω; ω
Pockels Effect (EO effect)	2	-ω;ω,0
Sum mixing	2	-ω_a; ω_1,ω_2
Optical Rectification (OR)	2	0;ω,-ω
Intensity-dependent refractive index	3	-ω; ω,-ω,ω
Optical Kerr effect	3	-ω_1; ω_2,-ω_2,ω_1
dc Kerr effect	3	-ω; 0,0,ω
Two-photon Absorption (TPA)	3	-ω_1; -ω_2,ω_2, ω_1
Third-harmonic generation (THG)	3	-3ω; ω,ω,ω
Coherent anti-stokes Raman scattering	3	-(2ω_1-ω_2); ω_1,ω_1,-ω_2
General four Wavemixing (FWM)	3	-ω_a; ω_1,ω_2, ω_3
Three-Photon Absorbtion (TPA)	5	-ω_1; -ω_2,-ω_3, ω_3,ω_2,ω_1
nth harmonic generation	n	-nω; ω,ω,.....,ω
Multi-photon Absorption (MPA)	2n-1	-ω; .....-ω,ω.....ω

1.7 Relationship between Macroscopic and Microscopic Polarizations

The classical method to relate the individual molecular polarizations with the bulk susceptibilities is through the *orientated gas-model*. The oriented-gas model is based on the following hypothesis:

1. The molecular polarizations are additive.

2. The charge distribution in each molecule is determined by the intramolecular field only and is consequently independent of motions and distributions introduced by other molecules of the crystal.

Within the framework of the oriented-gas model, for a bulk system (such as liquids, molecular solids or organic glasses) consisting of weakly interacting molecules, the bulk polarization P is derived from the distortion of electronic clouds in constituting molecules. The bulk linear optical susceptibilities $\chi^{(1)}$ and non-linear optical susceptibility $\chi^{(n>1)}$ are, therefore, obtained from the corresponding molecular nonlinear optical coefficients α, β, γ etc, by using a sum of the molecular coefficients over all the molecular sites. The sum should consider their orientational distribution (different orientations at different sites). Let the crystallographic axes be labeled with (I,J,K) and the microscopic polarization axes in the individual molecules be (i,j,k). The angle between the crystallographic axis I and the microscopic axis i_s, is denoted as ${\theta_{Ii}}^{(s)}$. Then it is fairly simple to transform the microscopic α and β into $\chi^{(1)}$ and $\chi^{(2)}$ as:

$$\chi^{(1)} = \frac{1}{N} \sum_{i,j} \sum_{s=1}^{N} (cos\theta_{Ii}^{(s)} cos\theta_{Jj}^{(s)}) \alpha_{ij} \tag{1.15}$$

and

$$\chi^{(2)} = \frac{1}{N} \sum_{i,j,k} \sum_{s=1}^{N} (cos\theta_{Ii}^{(s)} cos\theta_{Jj}^{(s)} cos\theta_{Kk}^{(s)}) \beta_{ijk} \tag{1.16}$$

where the sum index (s) runs upto the number of molecules (N) in the crystal per unit volume. Nonlinear optical interactions in a molecular medium, described by the bulk nonlinear optical susceptibilities, now become primarily molecular properties, described by the values of $\chi^{(1)}$ and $\chi^{(2)}$. Thus, for a material to have interesting NLO activity, both the individual molecular hyperpolarizability and the orientation effects have to be optimized. In general, charge distribution due to π-electrons are readily deformable. Therefore, molecules with conjugated π-electrons give rise to large molecular hyperpolarizabilities (β and γ). In comparison, contribution due to σ-electrons are considerably smaller. However, the factors that govern their interactions in the supermolecule/ crystal are still not very clear.

Additionally, the basic assumptions within the oriented-gas model are themselves quite drastic. For almost all molecular crystals, H-bonding and/or the dipolar interactions are the most important intermolecular forces and although these interactions are quite weak in magnitude, are strong enough to control the crystal geometry of the macromolecular systems. Such intermolecular forces do indeed lead to cooperative enhancement or damping in the polarization responses of the aggregates. Thus, in a strict sense, α and β are not additive quantities. For example, Peris and co-workers have considered head-to-tail arrangement of paranitroaniline and their calculations

have shown large cooperative enhancement in the molecular second-harmonic generation (SHG) coefficients (β). They have also considered chains of HF molecules in both their linear and zig-zag orientations wherein they find cooperative enhancement of β for the linear chains, while cooperative damping for the zig-zag chains [19]. Champagne and co-workers have performed calculations on the crystals of 3-methyl-4-nitroaniline (MNA) wherein they find that such crystals show very strong anisotropy in polarization along the crystallographic axes [20]. For the long axis, where the molecules are arranged in head-to-tail fashion, H-bonding leads to enhanced electrostatic interactions as a consequence of which the transition dipole moment to the charge transfer states increases. This enhances only one diagonal component of β. However, such interactions being absent in the other two directions, lead to reduction in β along those axes.

It is therefore, of fundamental interest, to optimize the parameters that control the bulk nonlinear optical susceptibilities together with the molecular hyperpolarizabilities. There have been a lot of efforts previously to derive the bulk susceptibilities from molecular analogues by both semi-empirical and *ab-initio* methods [25, 26]. However, a proper understanding of the relationship between the orientation and bulk property is still elusive. Recent combined experimental and theoretical work by Custelcean et al. investigates the role of the steric interactions of the alkyl groups in N,N-Dialkylthioureas in fine-tuning the H-bonding interactions in the crystalline environment [27]. Lee et al have performed density functional theory calculations for the charge-density and topological feature like atoms-in-molecules (AIM) on the monomers, dimers, heptamers and X-ray structures of thiourea

S,S-Dioxide, to understand the intermolecular charge density distributions for different sizes of the aggregates [28].

As a whole, from the technology point of view, the synthesis of newer crystals with large nonlinear optical cross section requires an understanding of the processes involved in crystallization together with the forces that stabilize non-centric arrangement of molecules in the crystals and self-assemblies.

1.8 Calculations of Nonlinear Optical Polarizabilities

For the calculation of microscopic nonlinearities, there are many approaches. Only three of them will be outlined here which have been used extensively in the subsequent chapters. These are *Finite Field Approach*, *Sum-Over-States Approach* and *Correction vector method*.

1.8.1 Finite Field Approach

The finite field approach expands the energy of the system in terms of the static field, F as:

$$E(F) = E(0) - \mu_i F_i - \frac{1}{2}\alpha_{ij}[F_i F_j] - \frac{1}{6}\beta_{ijk}[F_i F_j F_k] - \frac{1}{24}\gamma_{ijkl}[F_i F_j F_k F_l] \ldots \quad (1.17)$$

The optical response functions μ, α, β and γ are the 1^{st}, 2^{nd}, 3^{rd} and 4^{th} order derivatives of the energy with respect to the static field respectively. These derivatives are calculated numerically using a five-point formula, where the energies are calculated at five different fields; F =0, F =F, F =2F, F =- F and F =- 2F and a truncated series of the above expansion is used to derive the various order derivatives [29, 30]. For example,

$$\alpha_{ii} = [[\frac{5}{2}E(0) - \frac{4}{3}[E(F_i) - E(-F_i)] + \frac{1}{12}[E(2F_i) - E(-2F_i)]]/F_i^2 \tag{1.18}$$

$$\beta_{iii} = [[E(F_i) - E(-F_i)] - \frac{1}{2}[E(2F_i) - E(-2F_i)]]/F_i^3 \tag{1.19}$$

$$\gamma_{iiii} = [[-6E(0)] + 4[E(F_i) + E(-F_i)] - [E(2F_i) + E(-2F_i)]]/F_i^4 \tag{1.20}$$

Although this method has been quite popular, it suffers from the following limitations:

1. The numerical n-point formula for calculation of the energy derivatives are valid only for very low field strengths like 0.001 V.

2. The energies need to be extremely accurate for the calculation of their derivatives. For example, the calculation of γ_{iiii} requires the energy to be accurate to the order of 10^{-14} eV for even a small field of 0.0001 au. As the molecular integrals in quantum chemical calculations are seldom more accurate than 10^{-12} eV, finite field procedure for hyperpolarizabilities may not be reliable enough.

1.8.2 Sum-Over-States Approach

The sum-over-states (SOS) approach has its basis in a perturbation theory method developed by Ward and Orr to account for the effects of an externally applied electromagnetic field on the motions of electrons [31, 32]. Under the influence of the oscillating field the electrons will be perturbed and the resulting polarization in the molecule can be obtained by the inclusion of the field as a perturbation

$$H^1 = -e(Er)\sin\omega t \tag{1.21}$$

to the Hamiltonian and collecting terms of appropriate orders in the electric field. In this expression, E is the amplitude of the field and r is a coordinate associated with the position of the electrons and is calculated from

$$r = \sum_a r_a \tag{1.22}$$

in which a is summed over all of the electrons and

$$-e.r = \mu \tag{1.23}$$

The polarizability and hyperpolarizabilities are expressed as an infinite sums over various excited states in which the numerators contain dipolar integrals of the type

$$< m|\mu_{p=i,j,k}|n > \tag{1.24}$$

where $m \neq n$. It corresponds to the *transition dipole moment* between the two states m and n.

The expression for the polarizability is then given by

$$\alpha_{ij}(\omega) = \sum_m \frac{e^2}{\hbar}[\frac{< g|\mu_i|m >< m|\mu_j|g >}{(\omega_{mg} - \omega)} + \frac{< g|\mu_j|m >< m|\mu_i|g >}{(\omega_{mg} + \omega)}] \quad (1.25)$$

In this expression g refers to the ground state and m refers to the excited state with $\omega_{mg} = \omega_m$ - ω_g.

The first hyperpolarizability term β[-(ω_p+ω_q);ω_p,ω_q], which is responsible for the second-harmonic generation, is given by

$$\begin{aligned}\beta_{ijk}[-(\omega_p + \omega_q), \omega_p, \omega_q] = P\sum_{mn} \frac{e^3}{2\hbar^2}[&\frac{< g|\mu_i|n >< n|\mu_j|m >< m|\mu_k|g >}{(\omega_{ng} - \omega_p - \omega_q)(\omega_{mg} - \omega_p)} \\ &+ \frac{< g|\mu_j|n >< n|\mu_i|m >< m|\mu_k|g >}{(\omega_{ng} + \omega_q)(\omega_{mg} - \omega_p)} \\ &+ \frac{< g|\mu_j|n >< n|\mu_k|m >< m|\mu_i|g >}{(\omega_{ng} + \omega_q)(\omega_{mg} + \omega_p + \omega_q)}] \quad (1.26)\end{aligned}$$

The symbol P indicates that the summations must be performed over all permutations of the Cartesian indices i, j and k, with the electric field frequencies ω_p and ω_q. This summation generates terms that are products of transition dipole moment matrix elements and also sums and differences of dipole moments between the ground and excited states as well as between various excited states. The above expression simplifies into an intuitively appealing expression if one considers the properties of the molecule to be approximated by a simple two-level model. The two-level model is discussed in details in the next chapter.

The second hyperpolarizability term $\gamma(\omega_t;\omega_r,\omega_q,\omega_p)$ is expressed as

$$\gamma_{kjih} = P\sum_{mnv}\frac{e^4}{4\hbar^3}[\frac{<g|\mu_k|v><v|\mu_j|n><n|\mu_i|m><m|\mu_h|g>}{(\omega_{vg}-\omega_r-\omega_q-\omega_p)(\omega_{ng}-\omega_q-\omega_p)(\omega_{mg}-\omega_p)} + \frac{<g|\mu_j|v><v|\mu_k|n><n|\mu_i|m><m|\mu_h|g>}{(\omega_{vg}+\omega_r)(\omega_{ng}-\omega_q-\omega_p)(\omega_{mg}-\omega_p)} + \frac{<g|\mu_j|v><v|\mu_i|n><n|\mu_k|m><m|\mu_h|g>}{(\omega_{vg}+\omega_r)(\omega_{ng}+\omega_r+\omega_q)(\omega_{mg}-\omega_p)} + \frac{<g|\mu_j|v><v|\mu_i|n><n|\mu_h|m><m|\mu_k|g>}{(\omega_{vg}+\omega_r)(\omega_{ng}+\omega_r+\omega_q)(\omega_{mg}+\omega_r+\omega_q+\omega_p)}] \quad (1.27)$$

The computation of the polarizabilities thus involves the evaluation of various dipole moment operators μ_{nm} and the energies, then summing over all the terms. These sums are actually infinite sums over all the excited states. However, in practice, one often utilizes the sum over the appropriate excited states.

1.8.3 Correction-Vector (CV) Method

In practice, the SOS method can only be expected to be successful if there is rapid convergence as the excited states of increasing energy are added to the perturbative expansion. This criteria is satisfied to a reasonable extent in the case of linear polarizability, where the main contribution comes from a small number of excitations associated with charge transfer across the system. However, this is not so in the case of first and second hyperpolarizabilities, where the slow convergence leads to greater difficulties as a very large number of excited states have to be considered. This makes the calculations for the hyperpolarizabilities extremely slow.

Another method developed by Soos and Ramasesha [33,34], for the computation of NLO coefficients, involves the variational calculation of the first and second order correction vectors $\phi_i{}^{(1)}(\omega_1)$ and $\phi_{ij}{}^{(2)}(\omega_1,\omega_2)$ to the unperturbed ground state in the presence of a perturbation. These vectors can be solved from the two inhomogeneous linear equations as:

$$(H - E_0 + \omega_1 + i\epsilon)|\phi_i^{(1)}(\omega_1) >= \tilde{\mu_i}|G > \tag{1.28}$$

$$(H - E_0 + \omega_2 + i\epsilon)|\phi_{ij}^{(2)}(\omega_1) >= \tilde{\mu_j}|\phi_i^{(1)}(\omega_1) > \tag{1.29}$$

where H is the unperturbed Hamiltonian, E_0 is the ground-state energy, ω_1 and ω_2 are frequencies and $\tilde{\mu_i}$ is the component of the dipole displacement operator, $\tilde{\mu_i}$=$\hat{\mu_i}$-$< G|\hat{\mu_i}|G >$ and ϵ is the average lifetime of the excited states. Once the correction vectors are calculated, the NLO coefficients can be readily determined as:

$$\alpha_{ij}(\omega) = (< \phi_i^{(1)}(\omega_1)|\hat{\mu_j}|G > +(< \phi_i^{(1)}(-\omega_1)|\hat{\mu_j}|G > \tag{1.30}$$

$$\beta_{ijk}(\omega_1,\omega_2) = P_{ijk}(< \phi_i^{(1)}(-\omega_1-\omega_2)|\hat{\mu_j}|\phi_k^{(1)}(\omega_2) >) \tag{1.31}$$

$$\gamma_{ijkl}(\omega_1,\omega_2,\omega_3) = P_{ijkl} < \phi_i^{(1)}(-\omega_1-\omega_2-\omega_3)|\hat{\mu_j}|\phi_{kl}^{(2)}(-\omega_1-\omega_2,-\omega_1) > \tag{1.32}$$

where P_{ijk} and P_{ijkl} are the permutation operators. The tumbling average

quantities, $\bar{\alpha}$, $\bar{\beta}$ and $\bar{\gamma}$ are defined as:

$$\begin{aligned} \bar{\alpha} &= \frac{1}{3}\sum_{i}(\alpha_{ii}) \\ \bar{\beta} &= \sqrt{\sum_{i}\beta_i\beta_i^*}; \qquad \beta_i = \frac{1}{3}\sum_{j}(\beta_{ijj} + \beta_{jij} + \beta_{jji}) \\ \bar{\gamma} &= \frac{1}{15}\sum_{ij}(2\gamma_{iijj} + \gamma_{ijji}) \end{aligned} \tag{1.33}$$

where the sums are over the coordinates x, y, z $(i, j = x, y, z)$ and β_i^* refers to the conjugate of β_i vector. The advantage of defining the tumbling average NLO coefficients is that they allow quantitative comparison of the calculated coefficients with experimental systems for three-dimensional molecules or aggregates.

For the present thesis, the computations are limited to those NLO properties which are mostly governed by the polarizations of the electronic states. That is to say that the electric field does not distort the lattice nor does it couple to the vibronic structure of the system [35, 36].

Chapter 2

Excitation spectra of molecular aggregates: Davydov splitting and its consequences on nonlinear optical response functions

2.1 Introduction

The development of materials with large nonlinear optical (NLO) properties is a key to controlling the propagation of light by optical means. In particular, the response of the materials to the application of the electric field has found tremendous applications in designing materials for NLO devices. These devices are being used in numerous applications, from lasers to optical

switches and electronics.

Some of the best NLO properties are displayed by the organic π-conjugated materials [37,38]. The organic materials are of great interest because of their low cost, ease of fabrication and integration into devices. One of the advantage in working with organic materials is that they allow one to fine tune the chemical structures and properties for the desired nonlinear optical properties. Because of a delocalized π-electron system, the macroscopic NLO polarizabilities of these materials are in almost all cases, governed by the NLO characteristics of the constituent molecules. This is an added advantage of modeling organic systems with optimally required NLO properties.

It would thus be of fundamental interest to explore theoretically the dependence of NLO response functions in organic aggregates to changing the nature and arrangement of the constituent chromophores. The energy shift due to the formation of various packing geometries reflect the change in polarization of the local environments. In this chapter, an exciton theory based on Davydov splitting is presented for N molecular aggregates with a varying orientations of monomeric molecules. Paranitroaniline (PNA) and 2-methyl-4-amino-nitrobenzene have been selected as models for the numerical calculations [1].

[1]Paper based on the work reported in this chapter has appeared in *J. Chem. Phys.* **118**, 8420 (2003)

2.2 Exciton model for the molecular aggregates

In this section, a basic model which can explain the electronic excitations of one dimensional molecular aggregates is discussed. As it is quite well known in the field of strong correlations, an excitonic state is the result of electron correlation and the exciton theory is an interaction theory between these excitonic states. In a self-assembled aggregates with low packing densities, the excitons are considered to be Frenkel type excitons where the electron and hole of a monoexcitation are located on the same molecular site. To develop a simple theory, composite molecules are considered, which includes van der Waals dimers, trimers and higher order aggregates. As has been pointed out in a number of previous works [39, 40], if the direct overlap between the chromophoric molecular orbitals (M.O.) is negligible, the exciton interactions can be expressed in the direct product basis of the chromophoric M.O.s.

Let us begin our discussion with the zeroth order Hamiltonian. The Hamiltonian for the mth molecule alone in an aggregate can be written as

$$H_m = \sum_k |k_m > (E^{k,m}) < k_m| \tag{2.1}$$

where k_m specifies the kth electronic state of the mth molecule. The wavefunction for the N number of molecules (in an aggregate) can be approximated as a linear combination of product functions $|k_1, k_2, \ldots, k_m, \ldots, k_N >$, where the k_m's are the kth electronic states for the molecule m. If the electronic exchange interactions are considered, the excitations will be the

admixtures of charge transfer states which correspond to Wannier type excitons. However it is assumed here that the intermolecular distances are large enough to make electron exchange effects quite negligible, at least in low order. The ground state of N molecules is then the tensorial product of the molecular ground states.

$$|G>=|G_1, G_2, \ldots, G_m, \ldots, G_N> \tag{2.2}$$

Each molecular excitation gives rise to a band of N degenerate product states in the zeroth order. For excitation e in the mth molecule, it reads

$$|m, e>=|G_1, G_2, \ldots, G_{m-1}, e_m, G_{m+1}, \ldots, G_N> \tag{2.3}$$

In general the spatial structure of an aggregate is not quite well defined. However translational symmetry can be assumed to be valid in case of a molecular crystalline system. Here, the case of a perfect molecular aggregate is considered. The exciton coupling interaction term is denoted as $H_{m,n}$ for the interaction between the monomers, m and n. The energy expressions are derived with the general $H_{m,n}$ terms. For the N monomeric molecules, energy matrix for any excitation e, for the perturbation $H_{m,n}$ will have the

general form

$$[E_{mn}] = E_G(N-1) + \begin{bmatrix} E_e & H_{1,2} & H_{1,3} & \dots & H_{1,N} \\ H_{2,1} & E_e & H_{2,3} & \dots & H_{2,N} \\ H_{3,1} & H_{3,2} & E_e & \dots & H_{3,N} \\ \vdots & \vdots & \vdots & \vdots & \vdots \\ H_{N,1} & H_{N,2} & H_{N,3} & \dots & E_e \end{bmatrix} \tag{2.4}$$

where E_G and E_e are the ground state energy and energy for the excitation e respectively. The matrix is assumed to be symmetric so that $H_{m,n} = H_{n,m}$.

However the above matrix can be solved exactly only for a few cases. Imposing either periodic or open boundary condition in a one-dimensional case, the energies of the N perturbed states can be written as,

$$E(q) = (N-1)E_G + E_e + 2H_{m,m+1}\cos q + 2H_{m,m+2}\cos 2q + 2H_{m,m+3}\cos 3q + \dots \tag{2.5}$$

where the energies are written in momentum space, q. Note that, both for periodic and open boundary conditions, the q-space energies are same, although the wavefunctions are completely different.

An analytical solution of the above expression can be obtained only for the nearest neighbor case. Assuming $H_{m,m+1}$ as the strongest coupling and neglecting all other types of coupling, the width of the excitation band e can be estimated to be $4H_{m,m+1}$ for periodic and $4H_{m,m+1}\cos(\pi/N+1)$ for the open chain case. However, if all the other ($|m-n| > 1$) $H_{m,n}$ couplings are considered, the width will be increased by 25% of the nearest

neighbor values. Moreover, the allowed transition is different for two different boundary conditions. For an open chain, the allowed transitions are to the states with $q = \pi/(N+1), 2\pi/(N+1), \ldots, N\pi/(N+1)$. For the periodic chain, however, the transitions are to the momentum states with $q = 0, \pi/N, 2\pi/N, \ldots, (N-1)\pi/N$ values. The expressions for $H_{m,n}$ coupling are considered next and followed by this, the consequences of the arrangement of monomer molecules on the allowed electric dipole transitions are discussed.

For dipolar molecules, the strongly allowed transition would be to the lowest exciton state and the coupling interactions can be approximated at large distances by a point dipole model. Assuming all molecules to be same, the coupling interactions can be written as

$$H_{m,n} = \frac{\vec{M}_{ij}.\vec{M}_{ij}}{r_{mn}^3} - \frac{3(\vec{M}_{ij}.\vec{r}_{mn})(\vec{M}_{ij}.\vec{r}_{mn})}{r_{mn}^5} \tag{2.6}$$

where $\vec{M}_{ij}$ is the transition moment from state i to state j of the monomer molecule and r_{mn} is the distance between the two molecular centers m and n. It is to be noted that both the transition dipole and the molecular axis($\vec{r}_{mn}$) are vectorial quantities. Thus, the magnitude of the interaction term will depend crucially on the relative orientations of the dipolar molecules as well as on the axis joining their centers. We shall give here a purely quasi-classical vector treatment to this interaction as we assume electrostatic interaction between the transition moments.

2.3 Excitation Spectra in the Molecular Aggregates

A number of cases can be analyzed where the dipolar molecules are arranged in various orientations. Let us assume that in the aggregate the chromophores are arranged as shown in Fig. 2.1 (upper panel). The directions shown there correspond to the polarization axis of the corresponding chromophores. The aggregate is constructed such that the chromophores are oriented with an angle ϕ between them and each monomer creates an angle θ with its molecular axis. It is quite simple to derive the splitting energy in this case from equation (2.6),

$$\Delta E = 2\frac{M_{gs}^2}{r_{mn}^3}(\cos\phi - 3\cos^2\theta) \tag{2.7}$$

Therefore a singlet excited state of the monomer molecule would split according to the angles, (θ, ϕ). Let us now derive the splitting patterns in the simplest aggregation for that of a dimer. The ground state and the excited state in two monomers can be represented as $|g_1>$, $|e_1>$ and $|g_2>$, $|e_2>$ respectively. On the formation of the head to tail arrangement of a dimer (θ, ϕ=(0,0) as shown in Fig. 2.1(a)), the ground state of the dimer $|G>=|g_1.g_2>$ is stabilized due to favorable dipole-dipole attraction while the excited state splits into $|E_1>=\frac{1}{\sqrt{2}}.[|e_1.g_2>+|g_1.e_2>]$ and $|E_2>=\frac{1}{\sqrt{2}}.[|e_1.g_2>-|g_1.e_2>]$. Since, dipolar interaction is attractive for this case, $|E_1>$ is lower in energy than $|E_2>$. The dipole-allowed transition occurs from $|G> \rightarrow |E_1>$, while transition is forbidden to the $|E_2>$ state. Clearly, the transition energy is smaller than the gap for the monomers and

thus this mode of aggregation leads to red-shift in the adsorption spectra. Strong absorption corresponding to $\sum_e \frac{1}{E-E(e)}|M_{ge}|^2$ will appear for transition to this state.

For the case of repulsive dipolar interactions as shown in Fig. 2.1(b), the ground is destabilized, while the excited states are: $|E_1>=\frac{1}{\sqrt{2}}.[-|e_1.g_2>-|g_1.e_2>]$ and $|E_2>=\frac{1}{\sqrt{2}}.[-|e_1.g_2>+|g_1.e_2>]$. In this case, $|E_1>$ is higher in energy that $|E_2>$. Thus, the allowed transition ($G \rightarrow |E_1>$) involves larger energy and the spectra will be blue shifted.

Apart from the linear arrangement of the dipoles, a very common orientation of dipoles are the parallel and anti-parallel stacking arrangements of the dipolar chromophores. They are shown schematically in Fig. 2.1(c) and Fig. 2.1(d) respectively. For the parallel arrangement [2(c)], the ground state of the dimer $|G>=|g_1.g_2>$ is destabilized due to unfavorable dipole- dipole repulsion while the excited state splits into $|E_1>=\frac{1}{\sqrt{2}}.[|e_1.g_2>+|g_1.e_2>]$ and $|E_2>=\frac{1}{\sqrt{2}}.[|e_1.g_2>-|g_1.e_2>]$. However, now due to dipole-dipole repulsion, $|E_1>$ is destabilized in comparison to $|E_2>$ and $|G> \rightarrow |E_1>$ represents the dipole allowed transition. For the anti-parallel arrangement, the ground state as well as the $|E_1>=\frac{1}{\sqrt{2}}.[|e_1.g_2>+|g_1.e_2>]$ state are stabilized and the dipole allowed transition occurs from $|G> \rightarrow |E_1>$. Other than the ideal cases shown in Fig. 2.1 (a,b,c and d), for intermediate angular orientation (different ϕ and θ) of the dipoles, it becomes fairly simple to find the excitation spectra for the dimers using the above formalism. Note that, for such cases, both the states E_1 and E_2 become accessible from the ground state, with varying oscillator strengths depending on the transition electric dipoles.

Figure 2.1: [Top Portion] Schematic representation of exciton splitting due to dipole-dipole interactions for various molecular orientations. The arrows indicate the vector quantities. ϕ is the angle between the dipoles and θ is the angle between the dipole and its molecular axis. [Bottom Portion] Dimer configurations (a, b, c and d). Orientations of the monomer dipoles in a composite system, with D→ A representing dipolar axis. Each molecule has two levels $|G>$ and $|E>$ and the arrows between states indicate the allowed transitions. Splitted states of the composite systems are denoted as dashed lines.

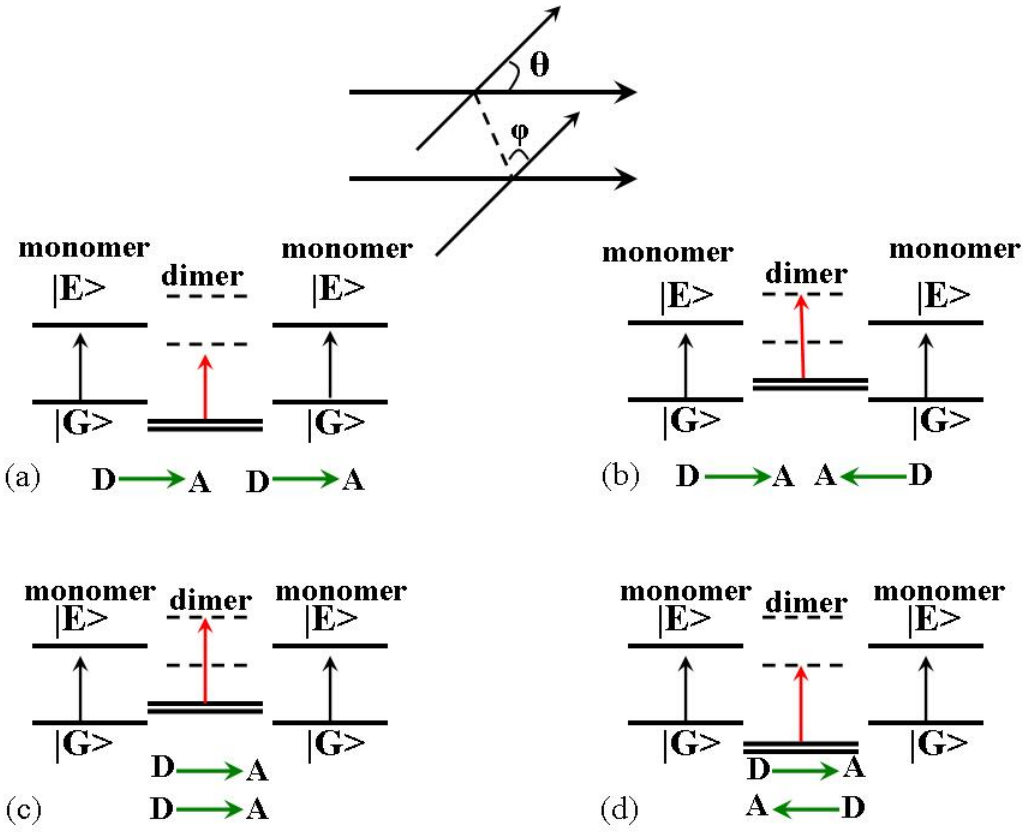

2.4 Dimer Geometries

To obtain a quantitative understanding in general cases with high to low packed monomer densities in an aggregate, numerical calculations are performed for the ground and excited singlet states of a few composite molecules. Computation work on a large aggregate is quite impossible so only double molecules are considered. However, a dimer gives information which would be useful in predicting its behavior in a large aggregate structure. Three model chromophoric molecules are considered to estimate their aggregation effects quantitatively. They are shown in Fig. 2.2 (A). In van der Waals and hydrogen bonding aggregates, the observed electronic spectra correspond to the exciton type interactions. As the exciton states are the fundamental excitations of interacting systems, for an accurate analysis, it is very important to know the correlated electronic spectra of the systems thoroughly. It is quite possible that some states which are weak in the monomer molecule may become active in the double molecule, due to reduced symmetry. This asks for a reliable quantitative interpretations.

Figure 2.2: (A) Structure of the three molecules considered for the quantitative estimations (B) The distance, d, for each of the four dimeric configurations. In each case as shown, the distance is between the two inter-monomeric neighboring N-atoms.

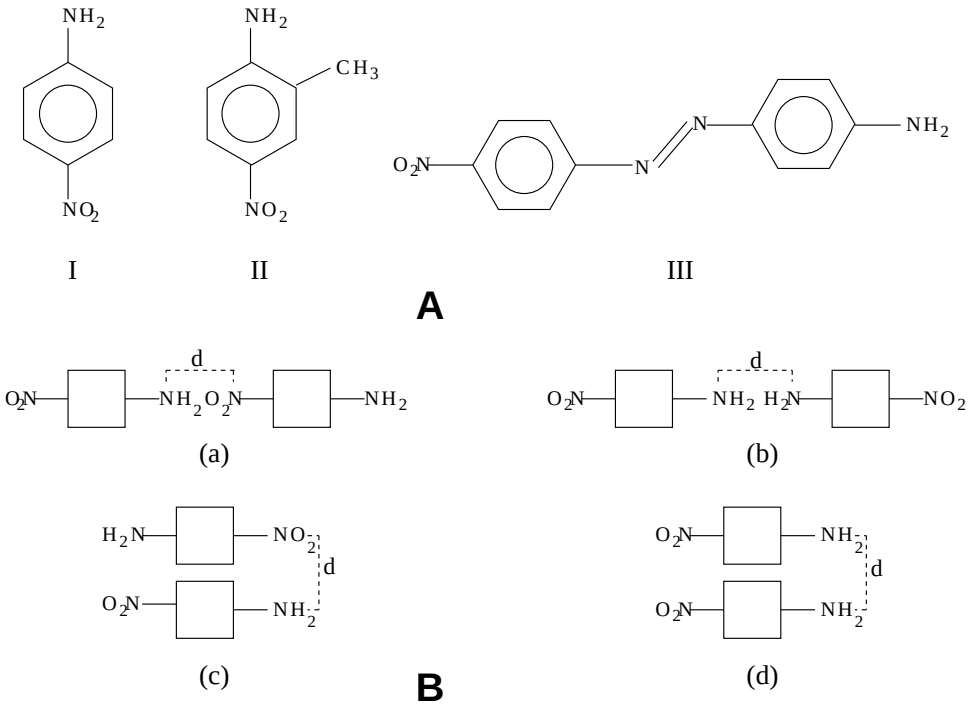

Geometries of the monomer molecules were optimized using AM1 parameterized Hamiltonian, a part of semi-empirical MOPAC package. No symmetry constraints were used in the optimizations. However, for the dimer configurations, although the optimized monomers are used, the composite structures are not optimized. These geometries were used to compute the SCF MO energies and then the spectroscopic properties using the Zerner's INDO method [41]. The levels of CI calculations, with singles (SCI) and multi-reference doubles CI (MRDCI) is varied, to obtain a reliable estimate of the second order optical response functions. The later method is particularly important since it includes correlation effects substantially. The MRDCI approach adopted here has been extensively used in earlier works, and was found to provide excitation energies and dipole matrix elements in good agreement with experiment [42, 43]. As reference determinants, those determinants are chosen which are dominant in the description of the ground state and the lowest one-photon excited states [44]. The MRDCI results include 4 reference determinants including the Hartree-Fock (HF) ground state. For each reference determinant, 5 occupied and 5 unoccupied molecular orbitals are used to construct a CI space with configuration dimension of 800 to 900. To calculate NLO properties, the correction vector method is used, as described in the introduction chapter [33]. Given the Hamiltonian matrix, the ground state wave function and the dipole matrix, all in CI basis, it is straightforward to compute the dynamic nonlinear optic coefficients using either the first order or the second order correction vectors. Details of this method have been discussed in the first chapter.

To study the double molecules, the optimized monomers are first generated. Then, by translating and (or) rotating in long axis direction, two of the same molecules are put together. The distance between these two monomers is such that no covalent bonding is possible between the intermonomeric nearest-neighbor atoms. Electronic excitation energies and spectroscopic properties are computed using the same formalism developed in the previous section.

The NLO properties for organic charge-transfer complexes like D-π-A can be captured very nicely by a two state model [45]. This model assumes that the electronic properties of the molecule are determined by a ground state and a low-energy charge transfer excited state. Polarization results primarily from the mixing of the charge-transfer state with the ground state through the interaction of the molecule with the electric field. In the two-state formalism, the complicated β expression reduces to:

$$\beta_{two-level} = \frac{3e^2}{2\hbar} \frac{\omega_{12} f \Delta\mu_{12}}{(\omega_{12}^2 - \omega^2)(\omega_{12}^2 - 4\omega^2)} \tag{2.8}$$

where ω_{12} is the frequency of optical transition between states 1 and 2, f is the oscillator strength and is the square of the transition moment between the ground state and the charge transfer excited state $<1|er|2>$ and $\Delta\mu_{12}$ is the difference between the ground-state and the excited-state dipole moments. From this expression, it is evident that as the optical gap (energy difference between the ground state and the 1st dipole allowed state) decreases (which can be implemented by increasing the conjugation length of the molecule) the magnitude for β increases. For the favorable head-to-tail arrangement

of the chromophores, the exciton level energies to the lowest dipole allowed state reduces. As a result, the optical response functions increase.

Before the results on double molecules are presented, the dipole moments and the polarizabilities obtained from our MRDCI method are compared with earlier ab *initio* calculations. For the PNA, the dipole moment from our MRDCI calculations (2.8au) compare fairly well with the ab *initio* value($\sim$ 3au). At a frequency of 0.028838au, the ab *initio* calculations give the polarizabilty $\sim$ 90au, compared to 57au from our calculations, for the PNA. For other frequencies too, the trend is very similar; for frequencies 0.077au, 0.1098au and 0.150au, the ab *initio*(MRDCI) values are 100(63), 107(73) and 134(115) respectively [46, 47]. For 4-amino-4′-nitro azobenzene, the higher level calculations with large basis functions give a value of static linear polarizability close to 160au. At a small frequency (0.028au), our estimation gives a value of 140au. The hyperpolarizabilities too are comparable for the PNA molecule; for a frequency of 0.005au, the ab *initio* estimation gives 892au [19] while our calculations for the same frequency give 821au. It is to be noted that these values from the ab *initio* calculations vary $\pm$20% depending on the basis states used. Since MRDCI numbers have also been used to quantify the experimental results, and given the comparisons above, it is believed that the results presented below give an accurate picture for double molecules at various distances and configurations.

2.5 Results and Discussions

Paranitroaniline is used as the first model molecule (molecule-I in the Fig. 2.2). The monomer molecule has a weak absorption band at 0.15798au with an oscillator strength of about 0.01, and a strong absorption band at about 0.169au with the oscillator strength $\sim$ 0.43. The linear polarizability and the EFISH (electric field induced second harmonic) coefficients (product of transition dipole and the first hyperpolarizability, $\mu\beta$) of the monomer are 45au and 2604au respectively at an electric field frequency of 0.00367eV. For the detailed comparisons of the interaction effects, four configurations of the PNA double molecules are considered, out of which two are *in-plane* and the other two are *out-of-plane* configurations. These four configurations are also shown in Fig. 2.2 (B).

In the Table. 2.1, the dependence of the ground state dipole moment, lowest singlet excitation gap, oscillator strength of the excitonic singlet, the linear polarizabilities and the EFISH coefficients($\mu\beta$), as a function of the nitrogen to nitrogen distance between two PNA molecules are shown in all the four configurations (see Fig. 2.2B for the definition of distance, d, in various cases). Note that the β is the tumbling average quantity, defined as $\beta = 1/3(\beta_{xyy} + \beta_{yyx} + \beta_{yxy})$.

Table 2.1: The dependence of the ground state dipole moment (μ_G in au), lowest singlet excitation gap (gap in au), oscillator strength (f), linear polarizability and the first hyperpolarizability (both in units of au), for a range of inter-PNA N-N distance, dist in $\mathring{A}$. Four dimer configurations have been considered (see Figure 2.2, for the configuration structures).

θ=0 and ϕ=0						θ=180 and ϕ=0					
dist	μ_G	Gap	f	α	$\mu\beta$	dist	μ_G	Gap	f	α	$\mu\beta$
2.5	10.25	.111	1.65	104	39999.5	2.9	0.0	1.84	1.63	60.3	0.0
2.6	10.09	.119	1.63	101	39831.2	3.0	0.0	1.84	1.63	60.6	0.0
2.7	9.809	.132	1.60	96.5	38430.1	3.1	0.0	1.84	1.63	60.9	0.0
2.8	9.589	.142	1.56	93.1	36715.1	3.2	0.0	1.84	1.63	61.1	0.0
2.9	9.412	.148	1.53	90.4	35113.8	3.3	0.0	1.84	1.63	61.2	0.0
3.0	9.274	.155	1.40	88.4	33726.4	3.4	0.0	1.83	1.64	61.5	0.0
3.2	9.074	.158	1.49	85.3	31556.5	3.6	0.0	1.83	1.64	61.7	0.0
3.5	8.897	.161	1.47	82.3	28845.3	3.8	0.0	1.83	1.64	61.9	0.0
3.8	8.799	.163	1.45	79.6	27953.7	4.0	0.0	1.83	1.65	62.2	0.0
4.0	8.866	.161	0.97	79.6	21612.4	4.5	0.0	1.82	1.66	62.7	0.0
4.5	8.791	.163	0.94	78.3	20406.9	5.2	0.0	1.82	1.67	63.1	0.0
5.0	8.740	.164	0.92	76.9	19551.7	5.6	0.0	1.82	1.67	63.3	0.0
6.0	8.673	.166	0.90	74.9	18396.2	6.0	0.0	1.81	1.67	63.6	0.0
7.0	8.630	.168	0.88	74.3	17672.9	6.6	0.0	1.81	1.67	63.8	0.0
8.0	8.602	.169	0.86	73.6	17117.9	8.8	0.0	1.80	1.68	64.3	0.0
9.0	8.579	.169	0.86	72.9	16849.5	9.7	0.0	1.80	1.68	64.6	0.0

θ=0 and ϕ=90						θ=180 and ϕ=90					
dist	μ_G	Gap	f	α	$\mu\beta$	dist	μ_G	Gap	f	α	$\mu\beta$
3.9	8.052	.131	1.59	55.6	16390.0	4.0	0.0	.165	0.910	74.9	0.0
4.0	8.064	.131	1.60	56.0	16644.7	4.2	0.0	.165	0.880	73.5	0.0
4.5	8.091	.133	1.63	57.2	17463.5	4.5	0.0	.165	0.870	72.8	0.0
5.0	8.119	.134	1.64	58.2	18196.1	4.7	0.0	.166	0.870	72.8	0.0
5.5	8.146	.135	1.65	59.1	18832.9	5.2	0.0	.167	0.870	72.8	0.0
6.0	8.170	.136	1.65	59.9	19387.8	5.7	0.0	.168	0.870	72.8	0.0
6.5	8.190	.137	1.66	60.6	19860.1	6.2	0.0	.168	0.860	72.8	0.0
7.0	8.205	.137	1.66	61.2	20270.3	6.7	0.0	.169	0.750	72.8	0.0
7.5	8.221	.138	1.67	61.7	20616.1	7.1	0.0	.170	0.580	72.8	0.0
8.0	8.237	.138	1.67	62.2	20916.3	7.6	0.0	.170	0.530	72.2	0.0
8.5	8.245	.138	1.67	62.5	21171.1	8.1	0.0	.171	0.510	72.2	0.0
9.0	8.253	.139	1.68	62.8	21389.4	8.6	0.0	.171	0.500	72.2	0.0
9.5	8.264	.139	1.68	63.1	21575.8	9.1	0.0	.172	0.487	72.2	0.0
10.	8.268	.140	1.68	63.3	21739.6	9.6	0.0	.172	0.478	72.2	0.0
20.	8.319	.140	1.69	64.8	22795.1	10.	0.0	.172	0.470	72.2	0.0

In Fig. 2.2 (B), the configurations (b) and (c) have a center of symmetry as the dipolar angle is 180°. The dipoles are facing opposite to each other resulting in exact cancellation of the corresponding dipoles of PNA monomers. Furthermore, in configuration (b), the same two groups (NH_2 in this case) are in the line next to each other, which results in repulsive interactions at short distances. On the other hand, in configuration (c), at short distances, there are attractive interactions due to π-stacking interactions. In the other two configurations, namely in (a) and (d), the corresponding monomeric dipoles create a 0° angle, resulting in a favorable quadrupolar configurations. However as in configuration (b), similar repulsive interactions exist at short distances in configuration (d) due to the same groups being next to each other.

Hydrogen bonding interactions stabilize the composite systems. Small positive and negative charges develop at the electropositive (hydrogen) and electronegative (nitrogen in our case) ends respectively in the composite structure. The distances are such that there exist rooms for formation of two hydrogen bonds (strength being strongest to weakest), at least in the configuration (a), for N-N distances of up to $3.8\mathring{A}$. The splitting of the excitonic levels, where hydrogen bonding is possible, corresponds to the combined effects of the dipole-dipole as well as the attractive Coulomb interaction due to hydrogen bonding. Specifically, the Coulombic interactions play a major role in its quantitative estimation, due to the large charge transfer possibilities in the hydrogen-bonded configurations. Hydrogen bonding also effects the ground state dipole moment of the composite molecule. This is the very reason for which in case (a), the ground state dipole reaches twice it's

monomeric value only at large distances. However the repulsion due to the same group at close distances (cases b and d) reduces the ground state dipole of the double molecule. For case (a), the excitonic gap reduces while oscillator strength, α and $\mu\beta$ increase dramatically at small distance values where hydrogen bondings are possible. Due to hydrogen bonding, the $\mu\beta$ value is almost 14 times greater than the monomeric $\mu\beta$. Considering the two-level β value, which is proportional to both $\Delta\mu$ and f, the Frenkel exciton estimate would give $\mu\beta \sim 22745$au at small distances. For case (d), at large distances, the $\mu\beta$ value is what is expected from exciton theory. However, at small distances, because of the repulsion between the same groups, the $\mu\beta$ of case (d) is close to the $\mu\beta$ of (a) at large distances. Other cases are not quite interesting but note the excitation energy gap for cases (b) and (c). For case (c), π-stacking is very weak at a N-N distance of $\sim 4\mathring{A}$, while for case (b), the repulsion energy is very high for all the distances. The zero value of $\mu\beta$ signifies the symmetry effects as well as our computational accuracies, for both cases (b) and (c).

The configuration (a) is an asymmetric dimer. The exciton theory based on dipole-dipole interactions provide a small shift (maximum $\sim$ 0.011au) even at small distances, with oscillator strength of the order 0.4. The strong red-shift at small distances is mainly due to hydrogen bonding. The lowest singlet excited state in the dimer is excitonic in character. These excitations have appreciable intensity and are associated with an appreciable dipole moment change, along the long axis of the dimer. The calculated low-energy excitonic character can be associated with the long-wavelength features observed in J-band aggregates [48, 49]. Previously a linear increase in the β

value was reported for HF linear polymeric configurations [19]. Coupled with the discussion above, one can thus safely conjecture that the PNA aggregates with hydrogen-bonded chromophores lying *in-line* can give rise to a large β value, with a one-photon absorption frequency deep inside the IR-region [19]. A few experimental confirmatory examples of such planer (although not exactly *in-line*) monomeric stacks, with large SHG coefficients have been reported earlier [50, 51].

As the splitting energy strongly depends on the oscillator strength, two other dipolar molecules in their planar optimized structures are also considered. These molecules have high oscillator strengths. For 2-methyl paranitroaniline, the oscillator strength is 0.5, while it is 1.6 for the 4-amino-4′-nitro azobenzene. In Fig. 2.3, the lowest excitation gap and the $\mu\beta$ value at an electric frequency of 0.00367au have been plotted for the double molecules (II) and (III) (as referred in the Fig. 2.2 (A)). The geometries of the dimer configuration is considered at the most favored arrangement, i.e, the $\theta = 0$ and $\phi = 0$ configuration. Also given are the monomeric counterparts of the same quantities in each of the figure panel. As expected, due to the *in-line* arrangements of monomer molecules, the quantities like hyperpolarizabilities increase drastically for the composite molecules, while the singlet-singlet gap reduces considerably.

The present semi-empirical calculations go beyond the PNA dimer considered in *ab initio* calculations [19]. However, the same optimized geometry of the PNA dimer is considered as suggested by Peris et al to study the dispersion behavior. The N-N distance is considered to be $3.6\mathring{A}$ in the head-to-tail arrangement as in configuration (a), Fig. 2.2 (B). It is found that

Figure 2.3: Plot of the excitation gap (in au) and $\mu\beta$ (in units of au), as a function of the distance, d (in $\mathring{A}$). The upper panel (open and filled circles) is for the dimer with molecule-(II) as monomer and the lower panel (open and filled diamonds) is the same with molecule-(III) as monomer. In both cases, the $\mu\beta$ values are calculated for the oscillating frequency, $\omega = 0.00367$au.

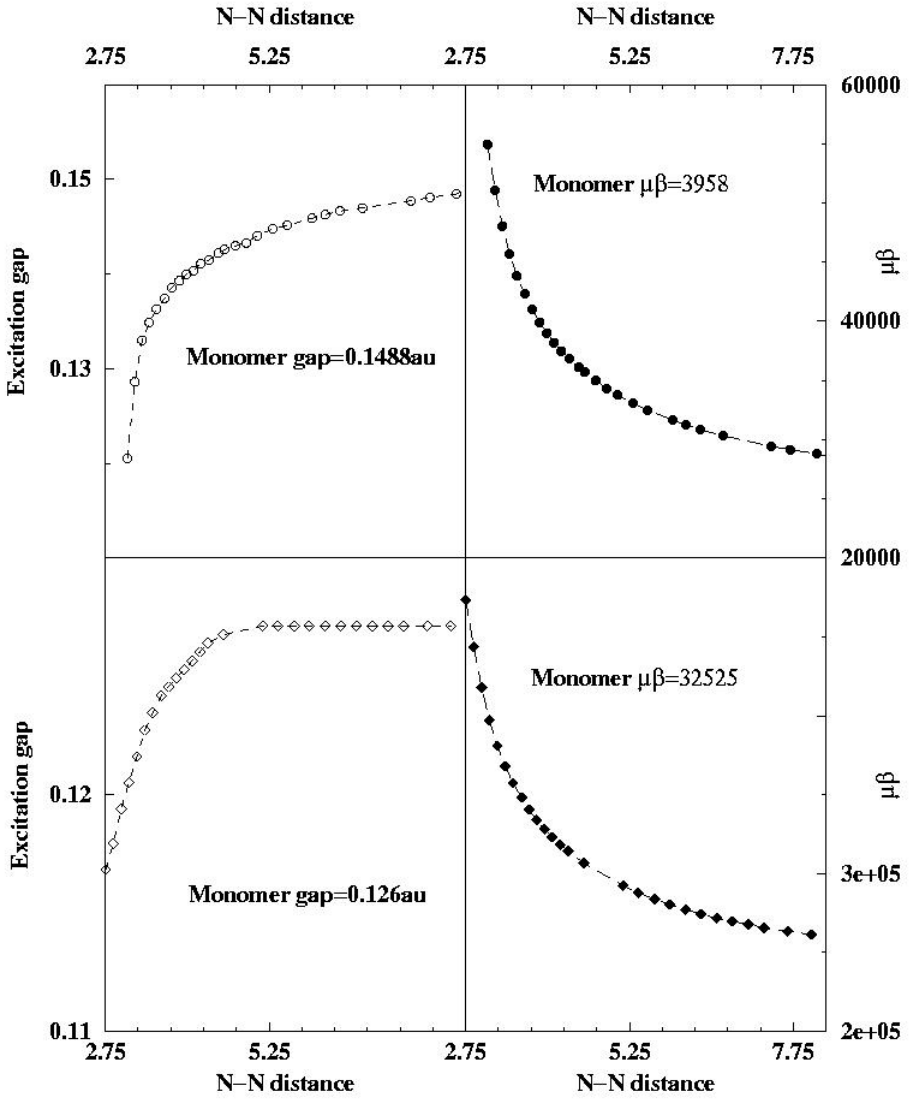

Figure 2.4: Dispersion curves for $\mu\beta$ (in units of au) for dimeric configurations of three molecules (see text for details); PNA dimer (filled circles), 2-methyl-paranitroaniline dimer (filled diamonds) and 4-amino-4′-nitro azobenzene dimer (filled triangles). Frequency is in au unit.

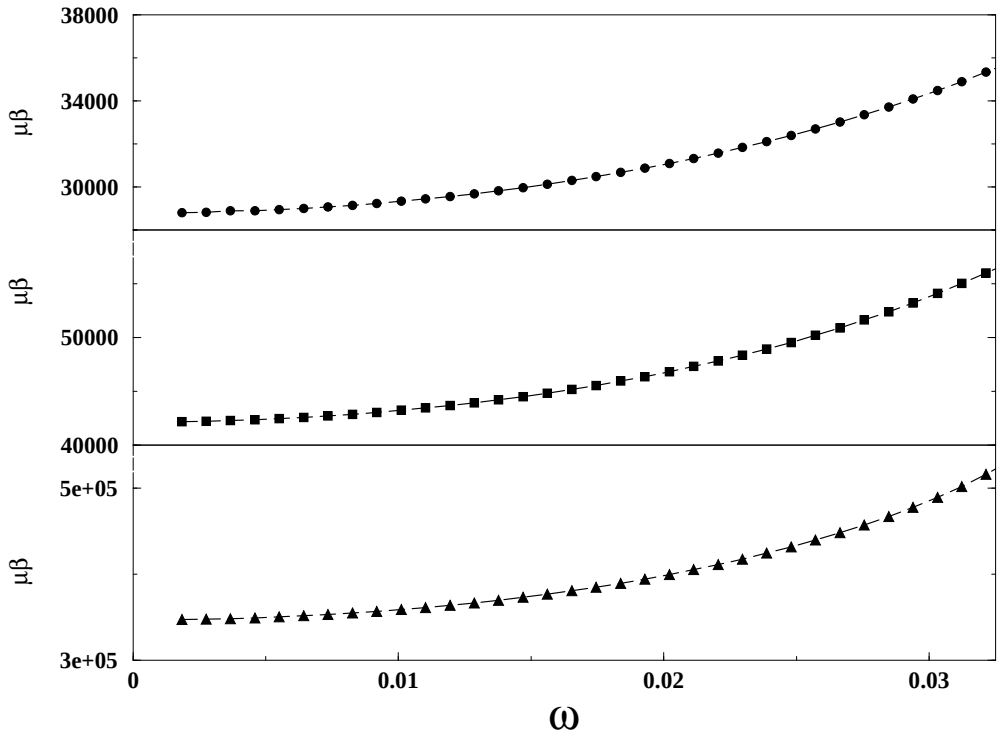

the molecules are hydrogen bonded most efficiently at this distance and the dimers are in their global minimal energy. For the other two molecules, similar distances are considered as in $(PNA)_2$. On these dimer geometries, the dependence of $\mu\beta$ on the frequency of the applied electric field is computed. The frequencies are chosen such that the system remains quite away from any resonance. Note that, for β, the one-photon resonance occurs at frequency corresponding to one-half of the one-photon gap. In Fig. 2.4, the EFISH coefficients ($\mu\beta$) for a frequency range, 0.00183au to 0.0349au are presented. For all three dimers, the $\mu\beta$ increases smoothly with the increase in frequency. The scaling is verified by fitting the data in frequency power, which gives an exponent ~ 2 for all three cases.

2.6 Conclusions

To conclude, extensive computations of a few dipolar organic molecules have been carried out on a number of dimeric configurations to understand the aggregation effect. Although our results are based on semi-empirical computation, the use of a number of reference configuration interactions account for a substantial correlation effects, and thereby give rise to qualitatively (if not exact quantitative) accurate picture for double molecules at various distances and configurations. It is found that the best arrangement is the *in-line* head-to-tail arrangement, which gives rise to an enormous increase in nonlinear optical properties. It is also shown that such a structure is extremely stabilized through hydrogen-bond formation and exciton-exciton interactions.

This dimer configuration is associated with an appreciable absorption intensity, and for an aggregate, this would appear deep in the IR-region. For at least two molecules, PNA [52, 53] and 2-methyl-paranitroaniline [54, 55], the crystal structure shows that they crystallize in the most favored arrangement as per our discussion, but the whole crystal structure becomes unsuitable for serious consideration. This can be avoided through the self assembly techniques [8], building arrays of the compounds in the desired pattern. The problems associated with such self-assembly is the relatively low packing densities [56]. This could however be avoided to some extent by connecting the monomers through efficient hydrogen-bondings or π-stacking, to form an infinite network of one-dimensional chains or co-facial planer structures. However, to achieve this, the molecular characteristics of the constituent monomers and their surrounding interaction effects have to be properly optimized. It is stressed that even if the monomers can not be arranged exactly *in-line* with each other, the effects discussed here will still be observed to some extent below a certain critical angle. To determine this critical angle, one simply requires knowledge about the phase relations between each of the transition dipole pairs. Therefore, a synthetic scheme well suited for the best dipolar arrangements of various monomers can be fine tuned to obtain large nonlinear optical properties at extremely low-energy.

Chapter 3

Understanding the role of dipolar and H-bonding interactions in fine-tuning the optical response functions in molecular aggregates

3.1 Introduction

As discussed in the last chapter, the dipole-dipole interactions have strong effects on NLO properties of aggregates through excitonic splitting. The role of H-bonding in governing the NLO properties of various supramolecular aggregates have, however, rarely been investigated in details. The strength of the hydrogen bonding is generally understood on the basis of its partition

into various contributions, like the electrostatic energy, exchange repulsion energy, polarization energy and charge-transfer energy [57]. Out of these terms, the charge-transfer(CT) effects are very important in controlling the NLO responses as such terms govern the strength of the transition dipole moment from the ground state to the optically active states. The CT salts are therefore quite well-known as technologically important NLO materials [58]. Although, the charge-transfer efficiency in hydrogen bonding are comparatively smaller than the CT-salts, the very fact that the H-bonding itself can be tuned under various environmental conditions like solvation and polarity, result in various degree of charge-transfer efficiencies.

Recently, Wu and co-workers have studied chains of urea molecules upto septamers and their calculations show that intermolecular H-bonding are quite significant in controlling the β and that proper inclusion of electron correlations at the Moller-Plesset 2 (MP2) level lead to enhancement of 15 percent in β value from the additive value as derived from the oriented gas-model [59]. However, calculations on the H-bonded dimers of aromatic carboxylic acids with various donor functionalizations by Sarma et al. show that the extent of intermolecular interactions due to H-bonding does not lead to cooperative NLO properties [60]. Thus, the contribution of H-bonding to the collective NLO responses in aggregates seems to be unclear. A proper understanding can be gathered through the systematic variation in the strengths of H-bonding.

In this chapter, the effect of H-bonding on second order polarizabilities (β) for a series of linear molecular assemblies is critically examined. A model system: HX (X=F, Cl,Br) has been chosen for the analysis. HX provides a

nice variation of the strength of bonding between the molecules, (HF > HCl > HBr). While HF chains have the strongest H-bonding, interactions in HBr chain is seemingly dipole-dipole type. Additionally, pure dipolar aggregates such as linear CO chains have also been considered. The HF chains show large cooperative damping in β from the additive values and provide clear signatures for the H-bonding effects. Weakly H-bonded systems like the HCl and HBr chains, in contrast, have similarities with the pure dipolar chain and have polarizations that are close to being additive [1].

3.2 Optimized structures of finite HX (X=F, Cl and Br) clusters

We have considered HF, HCl and HBr clusters at different levels of theory. For the geometry of a single monomer unit of HX, electron correlation at different levels are considered: DFT (B3LYP and B3PW91) and MP2. The basis sets are varied from the 6-31G level to the Dunning's correlation consistent polarized valence double zeta basis level augmented with diffused functions (aug-cc-pVTZ). The B3LYP/aug-cc-pVQZ level of theory provides a value of d_{HF} (μ_G) = 0.92$\mathring{A}$ (1.81 D), d_{HCl} (μ_G) = 1.28$\mathring{A}$ (1.15 D) and d_{HBr} (μ_G) = 1.42$\mathring{A}$ (0.83 D). These bond lengths compare fairly well with the experimental results, 0.917$\mathring{A}$ (1.86 D), 1.274$\mathring{A}$ (1.11 D) and 1.414$\mathring{A}$ (0.788 D) respectively [61]. Thus, all further calculations are performed using these bond lengths derived at the B3LYP//aug-cc-pVQZ level.

[1]Papers based on the work reported in this chapter have appeared in (1). *J. Mol. Struct. (Theochem)* **756**, 97 (2005). (2) *J. Chem. Theory Comput.* **2** 30 (2006).

We have also optimized the structures of the aggregates: $(HF)_n$, $(HCl)_n$ and $(HBr)_n$. The extent of electron correlations was varied from the B3LYP and B3PW91 to the MP2 level to confirm the global minimal energy of these structures. The geometries obtained from our calculations are shown in Fig. 3.1, Fig. 3.2 and Fig. 3.3 for $(HF)_n$, $(HCl)_n$ and $(HBr)_n$ respectively. For both HF and HCl clusters, our reported structures are very similar to those obtained from previous works in the literature [62]. For HBr, a frequency analysis was additionally performed to verify the ground state geometries. Structures of different symmetries were used as starting points to reach to the global minimal energy ground state. However, it has to be admitted that these structures have other geometries that are very close in energy to those reported here.

As can be seen, there is a very strong cooperative interaction between the molecules as all the geometries have cyclic forms. The advantage of forming a cyclic structure arises because of the ability to form hydrogen bonding between the terminals which otherwise remain open for a non-cyclic system. The cyclic forms are stabler by $\approx$ 2-3 kcal/mol compared to the acyclic structures for HF. For example, for n=3 and n=4 although a non-cyclic geometry ensures the participation of 2 and 3 lone-pairs of halides respectively in H-bonding, the ends remain free. A cyclic form thus ensures the highest number of connections for the H-X...H pairs.

However, the overall stability of the cyclic form decreases in the order HF >HCl > HBr, following the trend in H-bonding strength. The variation in the strength of the H-bonding also has effects on the individual structure. For example, while for HF, all the cyclic structures are planar due to stronger

Figure 3.1: Optimized structures of HF clusters (B3LYP/aug-cc-pVQZ level optimization).

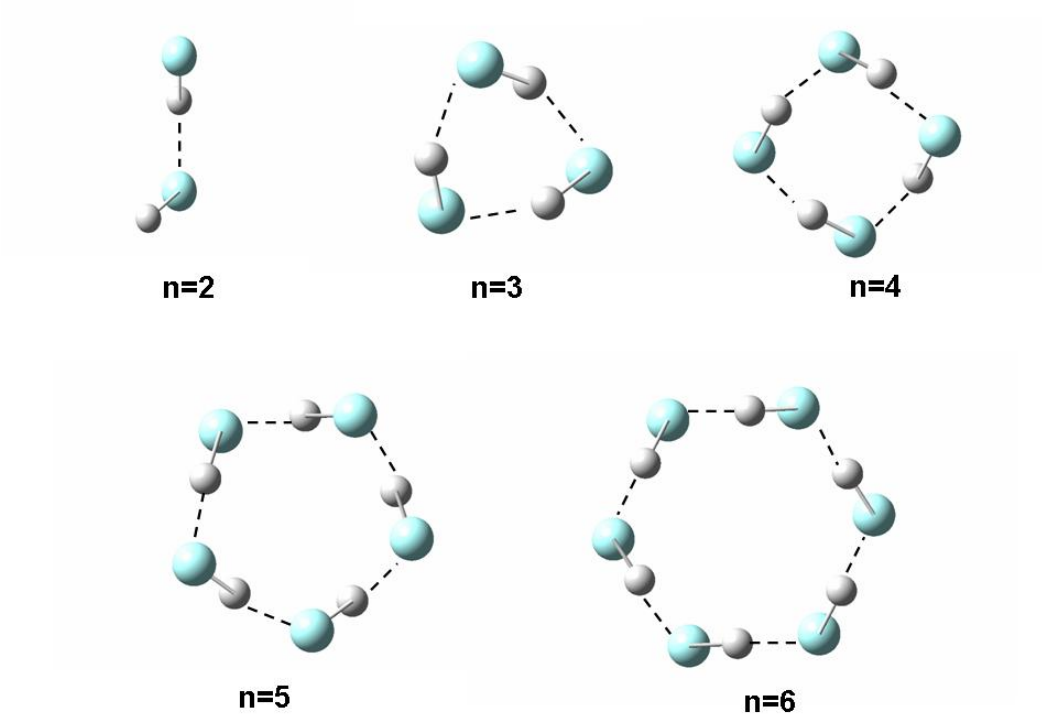

Figure 3.2: Optimized structures of HCl clusters (B3LYP/aug-cc-pVQZ level optimization).

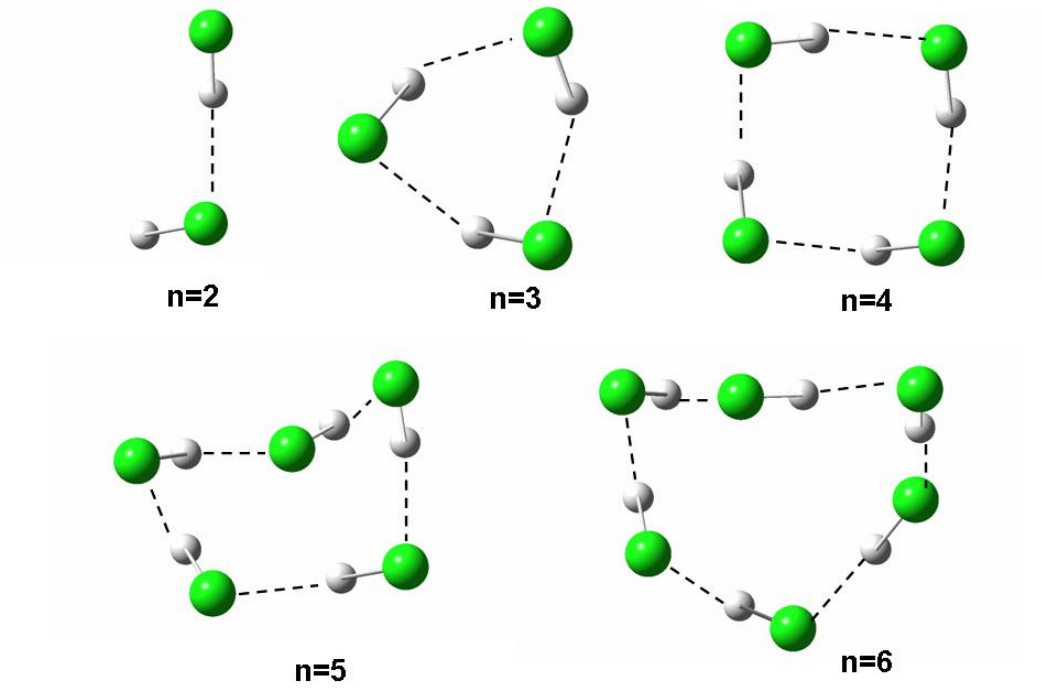

Figure 3.3: Optimized structures of HBr clusters (B3LYP/aug-cc-pVQZ level optimization).

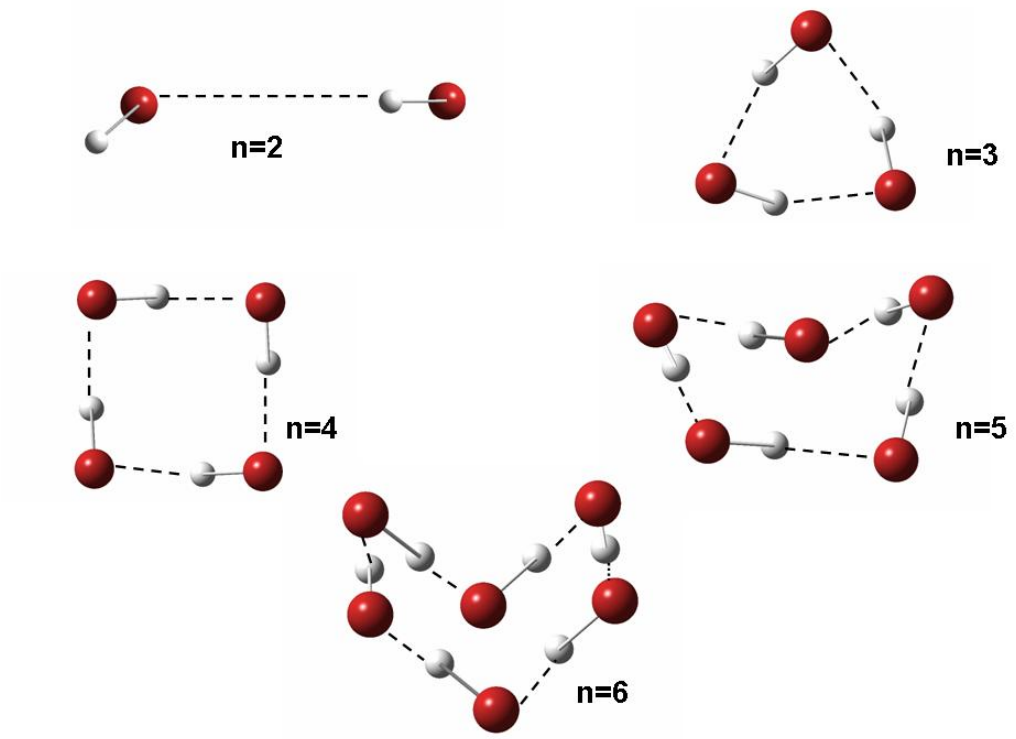

H-bonding, HCl and HBr have non-planar puckered structures for the larger cyclic systems: n=5 and 6. $(HCl)_5$ has an envelope-like structure while $(HBr)_5$ has a half-chair like structure. Such structures are well-known for the organic five-membered molecules like cyclopentane with almost equienergetic envelope (C_s symmetry) and half-chair form (C_2 symmetry) [63]. Also, the minimum energy structure for $(HF)_8$ (not shown) was found to have a highly symmetric crown type geometry (D_{4d}) similar to that for cyclooctane. It is very interesting to note that these H-bonded systems also show similar steriochemical features as in organic π-bonded molecules.

For n=6, $(HF)_6$ has a hexagonal planar structure while for $(HCl)_6$ and $(HBr)_6$, the structures are non-planar half-open book type. Formation of non-planar structures indicate the presence of strong non-bonded interactions between the lone-pairs of electrons (3 each) on the Cl and Br, which are not quenched by the formation of weak H-bonds.

For an analysis of the energetics associated with these structures, the binding energies for the clusters are calculated as; $\Delta E_{0,n}$: = $nE_0[(HX)]$ - $E_0[(HX)_n]$. The binding energies are corrected for the zero-point vibrational energy (ZPVE) and the basis set superposition errors (BSSE). BSSE was eliminated using the counterpoise correction(CP) scheme [64, 65]. Fig. 3.4 shows the binding energies for the $(HF)_n$, $(HCl)_n$ and $(HBr)_n$ for n=1 to 6, at the B3LYP/aug-cc-pVQZ level. The binding energy increases with increase in the cluster size. HF clusters are bound strongest while the HBr clusters are weakly bound.

Figure 3.4: Variation of binding energy, ΔE for different sizes of optimized clusters for HF, HCl and HBr.

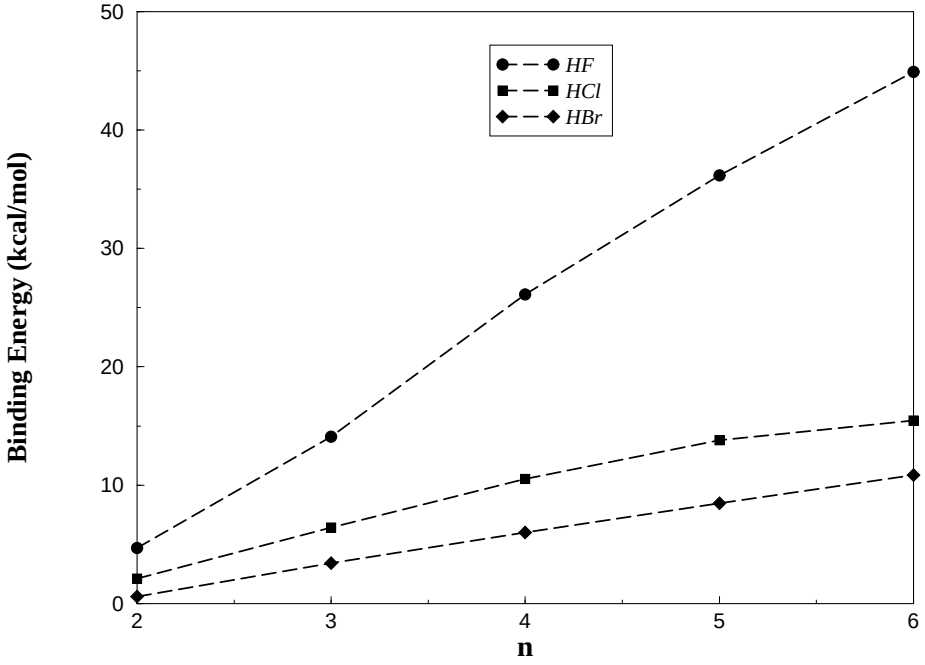

3.3 Nonlinear optical responses in linear HX and CO chains

From the discussion above, it is clear that the H-bonded clusters have a strong preference for a cyclic architecture. However, such cyclic geometries lead to centrosymmetricity, thereby reducing substantially the even-order NLO (like β) responses. Many NLO active materials like urea, PNA and MNA have a linear arrangement of the chromophores connected by H-bonds. Therefore, to model the H-bonding effect in a single linear chain, a linear chain for $(HX)_n$ is considered here. The distance between each HX unit is kept constant for all chain lengths. Fig. 3.5 shows the linear chains considered. The H-X...H distances are also shown. These are the average H-X...H distances derived from literature.

For an analysis of the energetics associated with these linear structures, the binding energies for the clusters are calculated using the definition: $\Delta E_{0,n}$ = $nE_0[(HX)]$ - $E_0[(HX)_n]$. All the energies are again corrected for zero-point vibrational energy (ZPVE) corrections and the basis set superposition errors (BSSE). Fig. 3.6 shows the binding energies in HF, HCl and HBr linear clusters at the B3LYP/aug-cc-pVQZ level (for cluster sizes upto n=6). The binding energies for the HF chain increases with increase in the cluster size. However, the binding energy remains almost constant for the HCl chain and for the HBr chain, the binding energy decreases with increase in the chain length. The negative binding energies for the HBr clusters arise essentially due to fact that the stable clusters of the $(HBr)_n$ are cyclic and the linear chains are the high energy structures. However, the linear HBr chains

Figure 3.5: Structures for the linear chains of HF, HCl and HBr. The distances (in $\mathring{A}$) between each monomer is kept constant as shown in the figure.

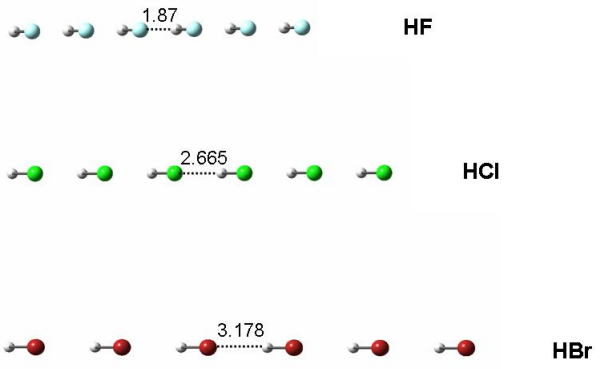

act as model to mimic the H-bonding in the weak interactions limits for chromophores arranged in a 1-dimensional manner. It is thus interesting to examine the nonlinear optical properties for these three limiting cases of stability in these linear chains.

The linear and the nonlinear optical coefficients for these clusters are computed using the finite-field method at an external electric field of 0.001 au. The 1^{st} hyperpolarizabilities (β) for the three cases show entirely different pictures (seen clearly from Fig. 3.7). For the $(HF)_n$, β increases initially till n=3 and then decreases. As already mentioned, there is a very strong H-bonding and such local maxima shows a clear signature of H-bonding effects. For HCl and HBr however, there are no signs of decrease in β with increase in the chain length. HCl chain shows a sharp increase till n=3 and then

Figure 3.6: Variation of binding energy, ΔE for different sizes of clusters for HF, HCl and HBr in linear chains.

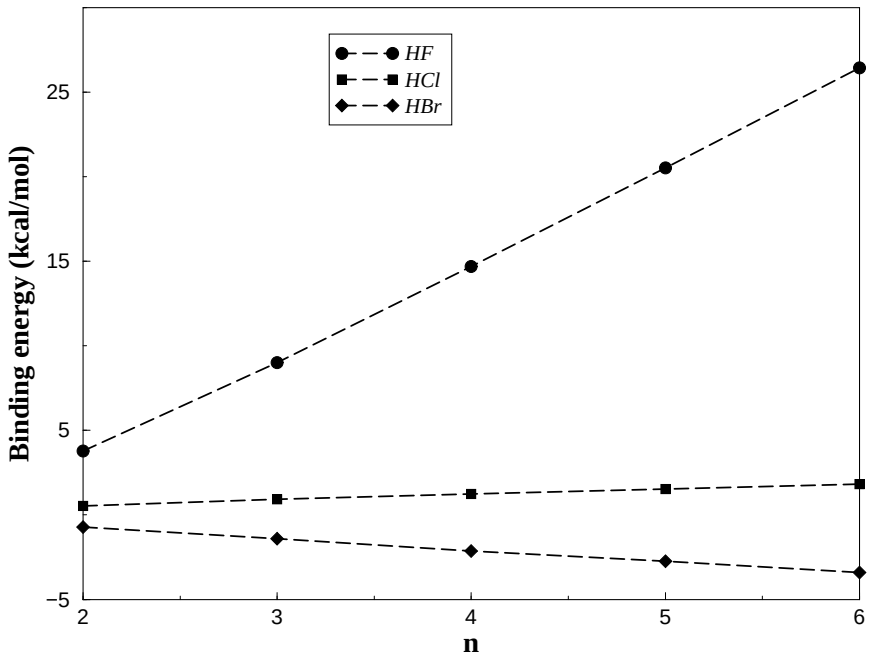

increases slowly. A rapid increase implies that H-bonding is still active for HCl at smaller oligomeric length but unlike HF, the bonding is not strong enough to reduce β with increase in n. For HBr, however, there is an uniform increase in β with the increase in chain length and the profile shows no discontinuity, indicating that H-bonding is very weak for all values of n and does not lead to any additional polarization effects.

For a clear comparison of these H-bonded aggregates with a purely dipolar aggregate, the NLO coefficients of a linear CO chain are also calculated. The distance between each CO unit in linear chain is considered to be 3.95 $\mathring{A}$, while the CO bond-length is found to be 1.13 $\mathring{A}$. The large CO...CO distance indicates pure dipole-dipole interactions. This CO linear chain mimics interactions in many NLO crystals constituted of π-conjugated molecules like PNA and MNA without however the H-bonded interactions. Thus, an analysis based on only a dipolar aggregate allows one to understand the effects of the dipolar component in a more detailed manner. For the CO chain, β shows a linear increase with increase in the nuclearity. Thus, when there are no effects of H-bonding, β has a linear profile. The deviation from the dipolar interactions increases in the order HBr $<$ HCl $<$ HF. In the limiting cases of weak H-bonding, the 1^{st} hyperpolarizability is mainly governed by the dipolar interactions. However, the decrease of β with increase in n must have a H-bonded origin which shows large cooperative phenomena of decreasing β with increasing n. It is interesting to note that the interactions with various length scales can lead to completely different NLO features.

3.3.1 Analysis

For a quantitative understanding of the cooperative nature of various interactions, the β of a molecular chain β_n is compared with n isolated molecules, nβ_1 (where β_1 is the SHG of a single monomer). These two quantities are plotted in Fig. 3.7 for all the four systems. HF shows a highly nonlinear profile in β_n with large deviation from the linear multiples of monomers (nβ_1). The polarization of the whole system decreases with strong H-bonding between monomers. HCl also shows a deviation wherein the β_n increases with the increase in n but the increase is slower although the slope is positive. The cases for HBr and CO are very similar. For both of them, β_n has a larger value than nβ_1 implying that the contribution of dipole-dipole interactions (Davydov splitting) towards polarizations helps increase β_n, in contrast to "strong" H-bonding. Thus, cooperative damping in the NLO properties decrease with decrease in the strength of H-bonding for linear 1-D aggregates.

The reduction in the magnitude of β_n with increase in n for HF can be traced to the change in the polarizations of the ground state in comparison to the dipole allowed excited state. It is found that for the HF chains, there is a large increase in $\Delta\mu$ ($\mu_{excitedstate}$ - $\mu_{groundstate}$) at small chain lengths (n=2), but a steady decrease in its magnitude with the increase in the chain length. For CO however, the $\Delta\mu$ increases with increase in chain length. From the two-level expression for β, an increase in the magnitude of $\Delta\mu$ implies large β. This explains the initial increase of β for HF at small chain length (cooperative phenomena) and the monotonic increase of β for CO, with increase in n. For the weaker H-bonded systems like HCl and HBr, the

Figure 3.7: Variation of β_n (solid line, with circles) and nβ_1 (dotted line) for HF, HCl, HBr and CO. Note the close similarity in profiles for HBr and CO.

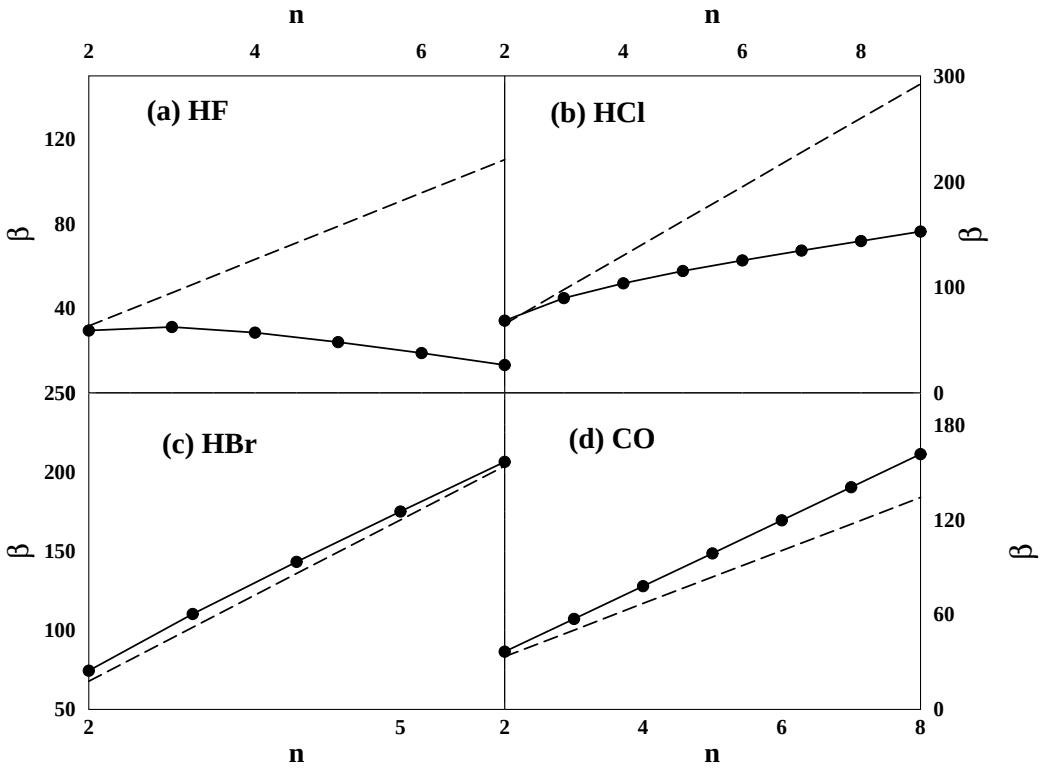

$\Delta\mu$ profiles progressively tends towards the purely dipolar CO profile.

To further understand the reason behind such a large polarization at small chain lengths for the strongly H-bonded systems, the Mulliken charge densities on the electronegative F-atom are calculated with the increase in the chain length, both in the ground and the lowest optically excited state. In the ground state (GS), $\delta^-{}_F \approx$ -0.5 for all chain lengths. In the excited state(ES), however, only for the monomer (HF), there is a strong feature of change in polarity (increased ionicity). For example, for HF (n=1), $\delta^-{}_F$ (ES) $\approx$ +0.316. But as n increases, the average ionicity decreases. Thus, for n=2, only one of the F atoms is ionic and the other F atom remains at $\delta^-{}_F \approx$ -0.5, similar to that in the GS. With further increase in n, the ionic contribution decreases further. Since for every n, there is only one F atom which is polarized in the excited state, the reduction in average ionicity with increase in n is of the order $\sim$ 1/n. Note that, the F atom which is polarized in the excited state is involved in hydrogen bonding with the neighboring H atom while its own hydrogen partner remains at the chain end without being involved in H-bonding. Interestingly, out of three types of F atoms in the $(HF)_n$ chain, the leftmost H-F is different and so is polarized. This is purely due to the chain nature of the aggregates and explains the decrease in $\Delta\mu$ as well as the β with the increase in n for HF. Thus, the boundary conditions play a very important role in determining the local polarizations in an aggregate. CO, on the otherhand, is predominantly covalent and thus the ionic contribution in the ES is small. $\delta^-{}_O$ is $\approx$ -0.29 both in the GS and the ES and no local polarization effects are found. On the application of an electric field, all the π-electrons in the $(CO)_n$ are polarized, resulting in

increase of β with increase in n.

Similar conclusions can also be made for the optimized structures for the H-bonded systems. For the optimized structures shown in Fig. 3.1, Fig. 3.2 and Fig. 3.3, most of the cyclic structures (at small n) have centrosymmetric architectures and as a result β values are quite small. This is particularly true for HF that has the strongest H-bonding amongst all. Thus, while a linear H-bonded chain creates a favorable situation for NLO activity (for HCl and HBr), the actual preference of a cyclic structure reduces the polarization responses. However for HCl and HBr, the larger cyclic structures have a noncentrosymmetric structure and β is non-zero, however, much smaller [almost $(\frac{1}{5})^{th}$] compared to their linear analogues.

3.4 Conclusions

Several important conclusions can be drawn from this work. Our computations based on linear and quasi one-dimensional chains serve as a thumb-rule model for estimation of interactions in actual crystalline geometries for most NLO active H-bonded compounds.

(i) Our energy calculations for the three hydrogen bonded species show that there is a strong preference for the cyclic structures. Such a cyclic structure although stabilizes the system, incorporates centrosymmetricity in the geometry thereby reducing the second harmonic response functions. However, for macromolecular aggregates of π-stacked molecules like PNA or MNA, a linear chain of H-bonds are sustained in the crystal.

(ii) We found that it is favorable to have H-bonding in the intermediate

regime (HCl...HCl)/(HBr...HBr) for large NLO coefficients across 1-D chains. A very strong H-bonding as that for HF...HF is found to reduce the NLO response functions. Although there is an enhancement of β even for pure dipolar aggregate like CO...CO, such chains are not stable. This is a very important result since in most crystals as well as in biological systems like DNA and proteins, intermediate H-bonding like N-H...O and N-H...N are the most predominant interactions. Thus, a relatively weak H-bond creates an ideal balance between the actual stability of the aggregate and increase in the NLO response functions.

Chapter 4

Nonlinear optical responses of multichromophoric aggregates in confined geometries: A case study for calix[3]arenes

4.1 Introduction

Much effort have been directed towards the synthesis of calix[n]arenes in the last decade [66]. In these class of systems, the individual chromophores are arranged in the form of 'baskets' by connecting the constituent molecules by linkers like $(CH_2)_n$ or $(CH_2O)_n$. Thus, these compounds provide an innovative strategy of arranging the chromophores in a parallel arrangement [67]. Moreover, one can even increase the number of chromophores in such an

assembly by changing 'n'. The inter-dipolar angle can be varied by functionalizing the lower and upper rims of the 'baskets' with groups of different sizes. The overall structure is then controlled by steric classes of interactions. It would thus be very interesting to ask how the individual dipoles of the chromophores interact in such a multi-molecular assembly and how such interactions and molecular properties translate into controlling the overall NLO properties of the calix[n]arenes. Although there has been a substantial effort in designing calix[n]arenes with large NLO responses [68], a proper understanding from a molecular viewpoint is still to be attained. To the best of our knowledge, there has been only a few works to model the NLO properties of these systems so far [69, 70] [1].

4.2 Model for Calix[3]arene

In this chapter, modeling the NLO properties in calix[3]arenes is undertaken by studying the dipolar interactions in a similar geometrical arrangement with a hydrogen fluoride trimer, $(HF)_3$. The dipole interaction is varied by (i) changing the inter-dipolar angle amounting to opening up of the 'baskets' and (ii) increasing the inter-dipolar distance. Additionally, since the most favorable arrangement from a dipole interaction point of view is the anti-parallel arrangement, similar calculations are performed for such a 'frustrated' dipolar system, $(HF)_3$, with two dipoles in the parallel arrangement while the third one in the anti-parallel orientation with the other two. We find that for such a 'frustrated' arrangement, with the basket opening up,

[1] Paper based on the work reported in this chapter has appeared in *Chemistry. A European. J.* **11**, 4961 (2005).

a favorable hydrogen-bonding interaction develops, which further stabilizes the system. Finally, the calculations on the true calix[3] arene systems have been performed and we have compared these results with the model $(HF)_3$ system.

4.3 Theory

Three HF molecules are arranged parallel to each other so that the lower base (lower rim) has three H atoms and the upper base (upper rim) has three F atoms. The three H and the three F atoms in each rim form two equilateral triangles. The geometry is shown in Fig. 4.1 (A). This is the all-parallel arrangement for the dipoles, applicable for a parallel cylindrical arrangement as in calix[n]arenes.

However, the most stable arrangement of such a dipolar arrangement is the anti-parallel arrangement. Systems like calix[4]arene have a significant percentage of the anti-parallel form (u,d,u,d; u,u,d,d) apart from the all-parallel cone geometry (u,u,u,u or d,d,d,d) [71]. Such a relaxation from the all-parallel to the anti-parallel arrangement is possible only for calix arenes with even number of chromophores, n=4,6,8 etc. For odd number of dipoles in the assembly, such a relaxation is however, not possible. For example, for n=3,5,7 etc. the dipoles are in a *frustrated* arrangement where the overall dipole-moment for the relaxed geometry does not vanish. The individual chromophores in calix[n]arenes are connected by short bridges that prevent random orientations of the dipoles. The simplest of such an arrangement is the $(HF)_3$ system shown in Fig. 4.1 (B). In fact, the $(HF)_3$ system is the

Figure 4.1: Arrangement of dipoles in a basket-type geometry for (A) parallel and (B) anti-parallel geometries. (a) Parallel dipoles with inter-dipolar angle, θ=0^0, (b). Geometry as the dipoles open up, the lower rim radius remains constant and the upper rim radius changes, (c) Fully opened basket with inter-dipolar angle, θ=120^0.

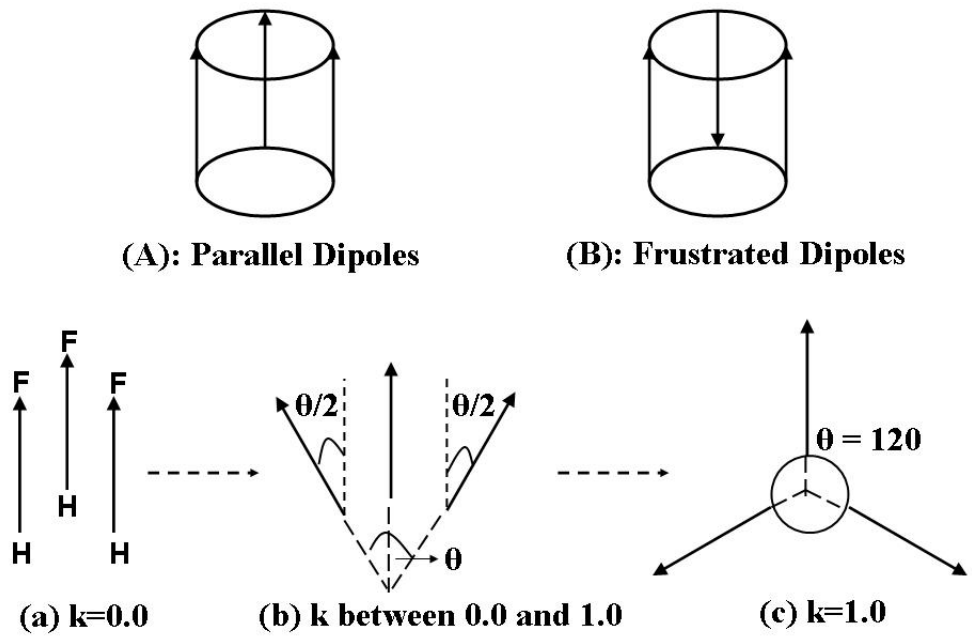

simplest case for a molecular assembly that can be studied for both parallel and frustrated cases simultaneously.

The inter-dipolar angle for real molecular systems is controlled by the steric bulk of the groups on the lower and the upper rim of the cylinder. Increasing the bulkiness of the groups in the upper rim while keeping the steric bulk of the lower rim constant, increases the inter-dipolar angle, with opening up of the basket. Thus, with opening, the system with a cylindrical symmetry is converted into a conical-shaped geometry.

For modeling the opening up of the cylinder for both the parallel (A) and frustrated dipoles (B), the lower rim with corresponding three atoms are kept constant and the coordinates of the three atoms in the upper rim are varied. The radius of the upper rim can be increased by translating the corresponding atomic coordinates according to: X=X+kX, Y=Y+kY and Z=Z-kZ, while keeping all the three molecular (HF) bond lengths fixed. The Z-axis corresponds to the internuclear axis and k is the flattening parameter which varies from 0 to 1.0. While the k=0 case corresponds to the perfect cylindrical arrangement for an inter-dipolar angle, θ=0^0 [see Fig. 4.1(a)], the k=1.0 signifies the other extreme, where, the cylinder becomes completely flat (Z coordinates are zero) so that all the six atoms (3H and 3F) are on the same plane, forming a circular disk. For such a case (k=1.0), the inter-dipolar angle, θ=120^0 [see Fig. 4.1(c)]. For all intermediate values of k, between 0.0 to 1.0, the cylinder is progressively opened up and the inter-dipolar angle, θ increases from 0^0 to 120^0 [see Fig. 4.1(b)].

4.4 Ground state dipole moment

With the dipoles opening up, the total ground state dipole moment changes as a function of the inter-dipolar angle. A general dipole moment expression for the combined effect of three dipoles can be written as

$$\mu_G = \sqrt{\mu_a^2 + \mu_b^2 + \mu_c^2 \pm 2\mu_a\mu_b\cos\theta_{ab} \pm 2\mu_b\mu_c\cos\theta_{bc} \pm 2\mu_c\mu_a\cos\theta_{ca}} \quad (4.1)$$

where μ_a, μ_b and μ_c are the dipole moment vectors for three dipoles a, b, c and θ_{ab}, θ_{bc} and θ_{ca} represent the angles between the corresponding dipoles. Note that, the dipolar angle determines the phase (+ve for parallel and -ve for frustrated arrangement) of the dipoles.

For the present case when all the dipoles are same (homomolecular system), μ_a=μ_b =μ_c=μ_i and θ_{ab}=θ_{bc}=θ_{ca}=θ_{ij}. In the parallel orientation [4.1 (A)], all the vectors remain in-phase. Thus, the total dipole moment is given by

$$\mu_G = \sqrt{3\mu_i^2 + 6\mu_i^2\cos\theta_{ij}} \quad (4.2)$$

For θ_{ij}=0^0, the μ_G has a maximum value of $3\mu_i$. When θ_{ij} increases from 0^0 to 120^0, the μ_G decreases monotonically to zero.

In the frustrated arrangement [4.1 (B)], two of the inter-dipolar angles are out-of-phase and one of them is in-phase. Thus the total dipole moment is

$$\mu_G = \sqrt{3\mu_i^2 - 2\mu_i^2\cos\theta_{ij}} \quad (4.3)$$

For this geometry, the μ_G increases from μ_i (for θ_{ij}=0^0) to $2\mu_i$ (for θ_{ij}= 120^0). Thus, for such a frustrated dipolar system, the ground state dipole moment

is a monotonically increasing function of the inter-dipolar angle.

4.5 Excitonic splitting for a multidipolar aggregate

The above expressions for the dipole moments are purely classical without any correlation among the dipoles. However, for systems with nonzero ground state dipole moment, there exists a strong dipole-dipole interaction. This dipole-dipole interaction leads to a large excitonic coupling and the effects are most prominent in the excited state of the molecules. A general scheme of such interactions has been considered in details in chapter 2. Here we outline a scheme of interaction between the three dipolar molecules as shown in Fig. 4.2. For such an aggregate, while the ground state, G,[$|G>=|g_1g_2g_3>$] is stabilized with respect to the monomer ground states [g_i], the excited states [e_i] which remain degenerate at infinite distance between the monomers, undergo splitting into three states, (E_1 [$|E_1>=2|e_1g_2g_3>$ - $|g_1e_2g_3>$ - $|g_1g_2e_3>$], E_2[$|E_2>=|g_1e_2g_3>$ - $|g_1g_2e_3>$] and E_3 [$|E_3>=|e_1g_2g_3>$ + $|g_1e_2g_3>$ + $|g_1g_2e_3>$]), when they are brought closer (see Fig. 4.2). Interestingly, out of these three states, two states (E_1 and E_2) are degenerate while E_3 is non-degenerate and symmetric. The extent of splitting, ΔE, however depends on the strength of dipole-dipole interactions, given by

$$\Delta E = \sum_{i,j} 2\frac{M_{gs}^2}{r_{ij}^3}(\cos\theta_{ij} - 3\cos^2\psi_i) \tag{4.4}$$

where M_{gs} is the transition dipole from the ground state to the excited singlet state of the monomer, r_{ij} is the inter-dipolar distance between the molecules i and j and the summation index runs over all the three molecules. The aggregate is constructed such that the orientation angle between any two monomers is θ_{ij} [θ_{ij}=θ_{12}=θ_{23}= θ_{31}=θ] and each monomer creates an angle ψ_i with its molecular axis [also ψ_i =ψ_1=ψ_2=ψ_3=ψ]. From the above expression, it is evident that a singlet excited state of the monomer molecule would split according to the intermolecular angles (θ) and molecule-dipole angles (ψ). For linear molecules or Donor-π-Acceptor type chromophores with a *para* orientation (for example, paranitroaniline), the dipolar axis and the molecular axis are collinear with ψ=0^0.

With the increase in the inter-monomer angle corresponding to the flattening up of the basket, there is a variation in the oscillator strength in the three states, E_1, E_2 and E_3. For the parallel case, at θ=0, E_3 is the only dipole allowed state with large oscillator strength, since it corresponds to the *in-phase* combination of all the three dipoles. However, as the inter-dipolar angle increases, in addition to E_3, E_1 and E_2 also become dipole allowed, more so, for large flattening angle. For the frustrated assembly, however, all the states are dipole allowed at θ=0 and as θ increases, the E_1 and E_2 become strongly allowed (higher oscillator strength) while the transition to E_3 becomes progressively weaker.

Figure 4.2: Excitonic splitting in a trimolecular dipolar aggregate due to dipole-dipole interactions. $|G>$ and $|E_1>$, $|E_2>$, $|E_3>$ represent the unnormalized eigenfunctions for the ground and excited states respectively in the assembly. Each $|g_i g_j e_k>$ is a direct product state of the aggregate involving the monomer states $|g_i>$, $|g_j>$ and $|e_k>$ of the monomers i, j and k respectively.

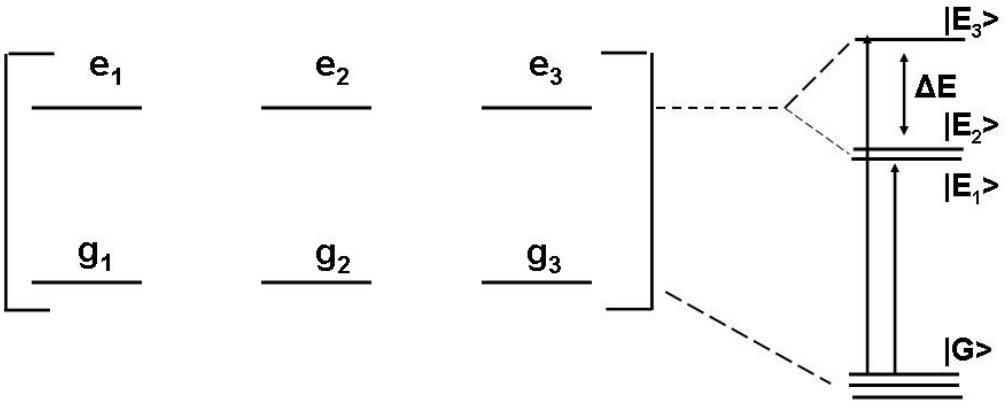

4.6 Results and Discussions

We have computed the dipole moment and the equilibrium ground state bond-length for hydrogen fluoride molecule (HF). Electron correlation has been taken into account through two different methods: The Becke'e three parameterized hybrid DFT method (B3LYP) and the MP2 methods. In order to compare the effects of electron-correlation as well as basis set effects, the level of basis set is varied from the 6-31G to aug-cc-pVQZ for both the two methods. The experimental values for the R_{eq} and dipole moment of HF are 0.920 $\mathring{A}$ and 1.80 Debye respectively [61]. The B3LYP/aug-cc-pVQZ level reproduces the experimental results quite well with R_{eq}=0.920 $\mathring{A}$ and μ(HF)=1.8084 Debye.

In the previous section, the analytical expressions for the total ground-state dipole moments have been derived as a function of the inter-dipolar angle. Since it does not include any correlation effect, the ground-state dipole moments for the $(HF)_3$ assembly at various inter-dipolar angles are computed using the B3LYP/aug-cc-pVQZ method. The variation of the dipole moment with the inter-dipolar angle for the all-parallel geometry of the dipoles (case A in Fig. 4.1) is plotted in Fig. 4.3. The inter-dipolar distances (d) are varied from 1.5 $\mathring{A}$ to 4.5 $\mathring{A}$. For comparison, the same plot for the analytical classical dipole moment is also shown.

At small inter-dipolar distances like 1.5 $\mathring{A}$, the computed dipole moment shows a very large deviation from the non-interacting analytical value. For example, at θ=0^0, the magnitude of the total dipole moment is only 3.9721 Debye compared to the analytical 5.4252 Debye, a reduction of 27 percent.

Figure 4.3: μ_G as a function of the inter-dipolar angle, θ for the parallel dipolar assembly.

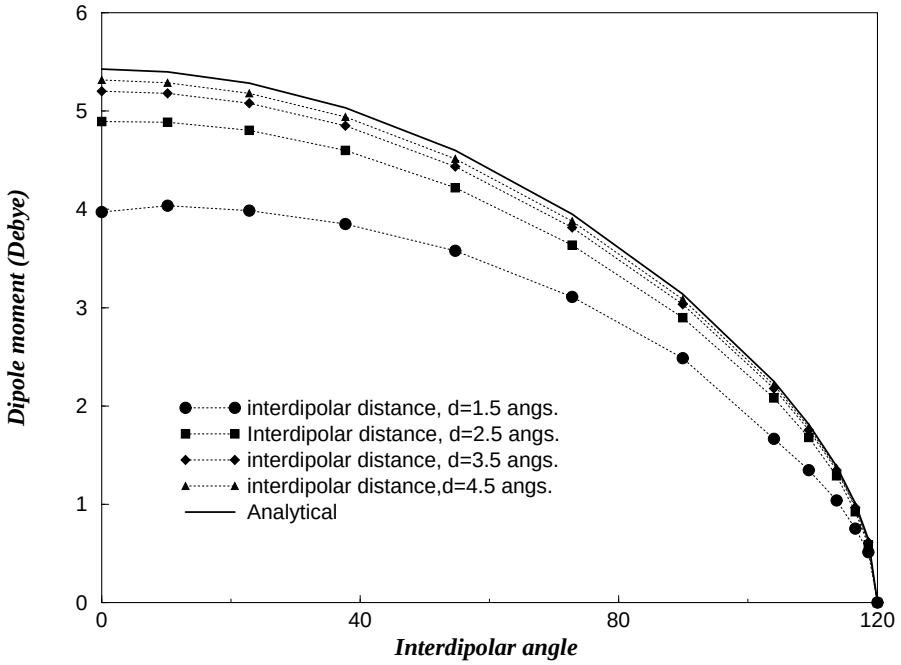

But, as the basket opens up, the deviation decreases and both the computed and the analytical values converge to 0 Debye for θ=120^0. This signifies the role of electronic correlations for the $(HF)_3$ assembly at small inter-dipolar distances and small inter-dipolar angles. But, as the inter-dipolar distance (d) between the HF monomers increases (around d$\sim$ 4.5 $\mathring{A}$), the intermolecular interaction decreases and the system transforms into a classical dipolar assembly.

The variation of μ_G for the frustrated dipolar system (B) shows very interesting features (see Fig. 4.4). At small inter-dipolar angles, the calculated dipole moments differ from the classical values, particularly for small d values. This is similar to the case for parallel dipoles. However, contrary to the parallel dipoles (see Fig. 4.3) where, with increase in the dipolar angle, the deviation becomes less prominent, the frustrated dipolar systems show very large deviation from the classical dipole moment values for large θ. The deviation is the largest for the case of small inter-dipolar distance of 1.5$\mathring{A}$.

As the basket starts to open up, two of the hydrogen atoms in two HF molecules come close to the fluorine atom of the third HF molecule. Initially the F...H-F angle is 90^0 but as the dipoles flatten up, the F...H-F angle increases towards 180^0. Such a linear F...H-F conformation has been found to be most suitable for the H-bonding interaction [72]. Therefore, with the increase in the inter-dipolar angle, the H-bonding interaction increases. The effect is most profound for the inter-dipolar distance of 1.5$\mathring{A}$ as the F...H-F bond is strongest at such distances. H-bonding interaction is primarily electrostatic in nature with δ^- on the F atoms and δ^+ on the H atoms. Not only the linearity, the distance between the electronegative atom and

Figure 4.4: μ_G as a function of the inter-dipolar angle, θ for the frustrated dipolar assembly.

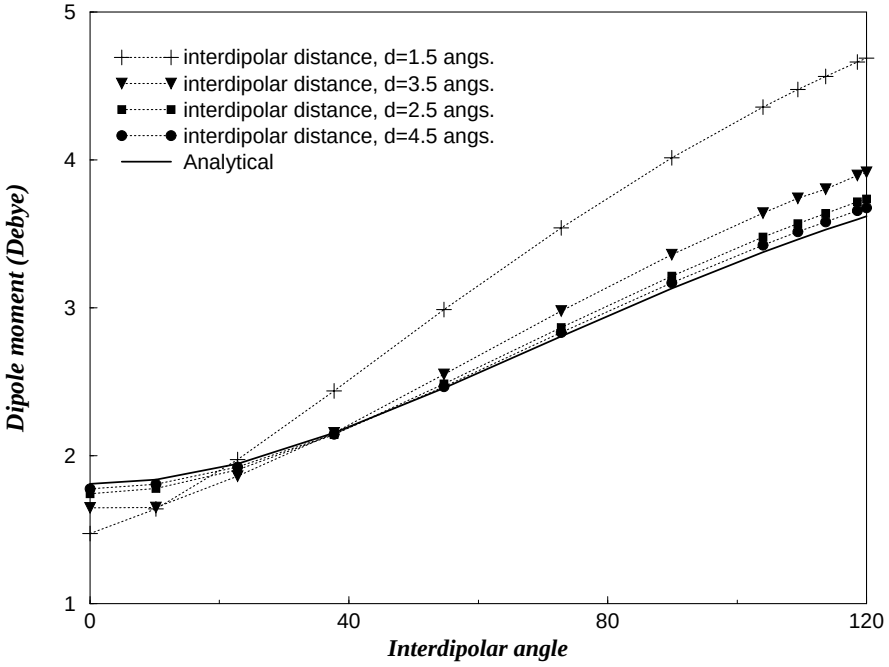

hydrogen atom also is crucial for effective charge transfer. Therefore, there is an overall enhancement of 30 percent in the dipole moment magnitude compared to the non-interacting value in the ground state dipole moment at small inter-dipolar distances and large θ values. However, as the inter-dipolar distance increases, the H-F...H bond becomes weaker and there is very little enhancement in the dipole moment from the classical value.

From the above discussion, it is clear that the extent of exciton splitting as well as the ground state dipole moment depend on the angular orientation of the dipoles. It will be novel to study such effects on the variation of the nonlinear optical properties for such systems.

For a quantitative estimation of the optical gap and the non-linear optical response property like the 1^{st} hyperpolarizability (β) for the geometries at the various inter-dipolar angles, the frequency dependent hyperpolarizability are calculated at 1064 nm corresponding to the experimental Nd:YAG frequency using the well-established TDHF formalism with 6-31G(d,p) basis set. The level for the basis set is varied from 6-31G(d,p) to 6-311G++(d,p) without any significant change in the magnitudes for the optical gap or β. The optical gap and β values are thus reported at the level of TDHF/6-31G(d,p).

In Fig. 4.5, the HOMO-LUMO gaps are plotted as a function of the inter-dipolar angle for the $(HF)_3$ (all-parallel system, case A, in Fig. 4.1) for a number of inter-dipolar distances. It is further verified that the HOMO-LUMO gap from TDHF/6-31G(d,p) actually corresponds to the optical gap found from ZINDO-CI calculations. The optical gap is calculated as the energy difference between the geometry relaxed ground state and the lowest optically allowed state with substantial oscillator strength. This corresponds

Figure 4.5: Optical gap as a function of the inter-dipolar angle, θ for the parallel dipolar assembly at TDHF/6-31G(d,p) level.

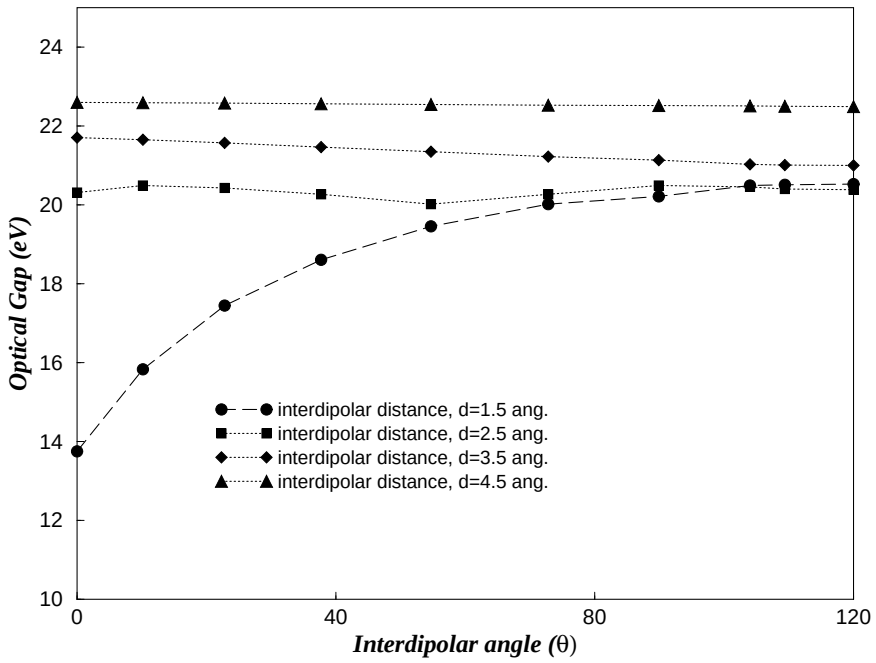

to the vertical optical absorption gap. It is found that, for the $(HF)_3$ system at a small inter-dipolar distance of 1.5 $\mathring{A}$, the optical gap is only 14 eV compared to 21 eV for large inter-dipolar distance, for a small inter-dipolar angle, $\theta = 0$. As the inter-dipolar angle increases, the gap for the small inter-dipolar distance increases up to $\theta \approx 70^0$, after which the optical gap saturates to a value of 21 eV. For larger inter-dipolar distances of 2.5 $\mathring{A}$, 3.5 $\mathring{A}$ and 4.5 $\mathring{A}$ there is no excitonic splitting and the gap remains almost constant at 21 eV. To quantify the extent of splitting in the $(HF)_3$ system, the optical gap for a single HF molecule is computed. The gap is $\approx$ 22 eV. Thus our results show that it is possible to reduce the optical gap to 60 percent of the monomer value in an aggregate. Such a remarkable effect can be realized by only fine tuning the inter-dipolar distance and the associated phase angle.

Similar features are also seen for the frustrated dipolar assembly, which is shown in Fig. 4.6. The optical-gap increases from 16 eV to the monomer (non-interacting) limit of 22 eV after an inter-dipolar angle of $\approx 70^0$. For larger inter-dipolar distances, there is no excitonic splitting and the gap remains constant at 22 eV. Note that, for small inter-dipolar distance of 1.5 $\mathring{A}$ and for $\theta = 0$, the frustrated case (case B in Fig. 4.1) shows larger gap (16 eV) compared to the all-parallel geometry (A) (14 eV) due to H-bonding stabilization of the ground state for the former.

The variation of the first hyperpolarizability (β) is investigated as a function of the inter-dipolar angle and the distances between them for the parallel orientations. At a small inter-dipolar distance of 1.5$\mathring{A}$, the magnitude of β decreases very rapidly with the increase in the inter-dipolar angle till $\theta \approx 30^0$ [Fig. 4.7(a)]. After such a initial steep decay, β decreases monotonically and

Figure 4.6: Optical gap as a function of the inter-dipolar angle, θ for the frustrated dipolar assembly at TDHF/6-31G(d,p) level.

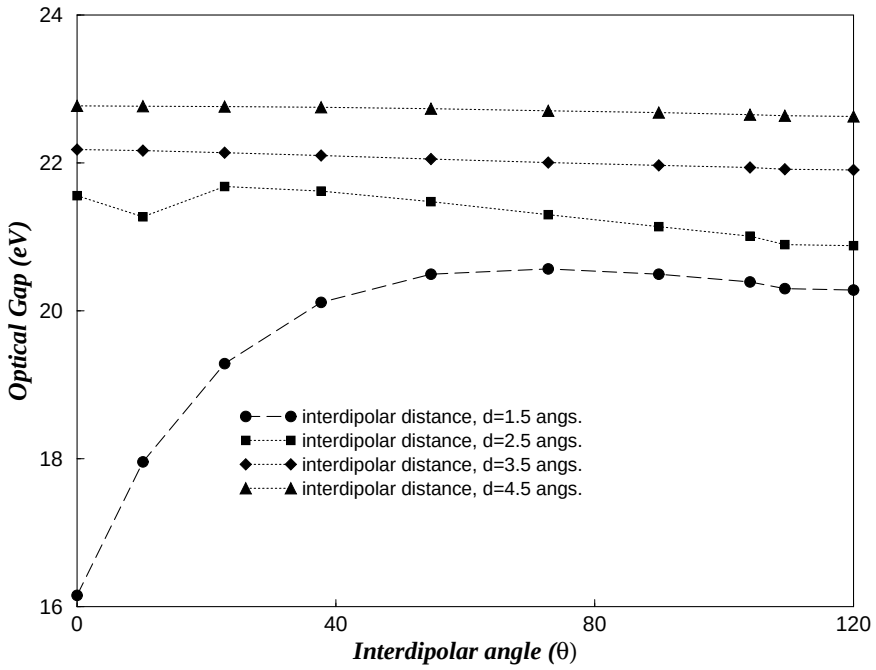

reduces to zero at $\theta = 120$. Thus, the β profile shows a clear signature of two parameters. At smaller inter-dipolar angles ($\theta < 50^0$), it is the optical gap that controls the magnitude of β. In fact, for smaller θ, the plot is similar to the plot for the optical gap (mirror image) which increases and then saturates (see Fig. 4.5). Since, the optical gap appears in the denominator in the β expression, the optical gap and the β have an inverse relationship, clearly visible by comparing Fig. 4.5 and Fig. 4.7(a). At larger inter-dipolar angles, however, when the optical gap almost saturates, the dipole difference (effectively the difference between the ground state and the excited state dipole moment) controls β. This is again clearly seen by comparing Fig. 4.7(a) and Fig. 4.3.

However, with the increase in the inter-dipolar distances, the optical gap becomes constant and saturates to the monomer limit. For such cases, the dipole moment difference between the ground state and the excited state (with the maximum oscillator strength) plays the major role in determining β with the increase in inter-dipolar distance. This is seen in the Fig. 4.7(b). For the inter-dipolar distance of $2.5\mathring{A}$, the plot for β shows a monotonic decrease and decays to zero at $\theta = 120$. If the optical gap was solely responsible for β, then the graph would have looked flat.

At large inter-dipolar distances, optical gap saturates, so that the magnitude of the excitonic splitting is no more important. However, the question remains whether the excited state is more polarizable than the ground state. In fact, we find that it is the $\Delta\mu_{12}$ which governs the magnitude of β at intermediate dipolar angles for large inter-dipolar distances. The signatures for such dipole moment controlled β is also seen for higher inter-dipolar distances

Figure 4.7: Variation of β with respect to the inter-dipolar angle at varying inter-dipolar distances for parallel orientation at TDHF/6-31G(d,p) level. β is in atomic units.

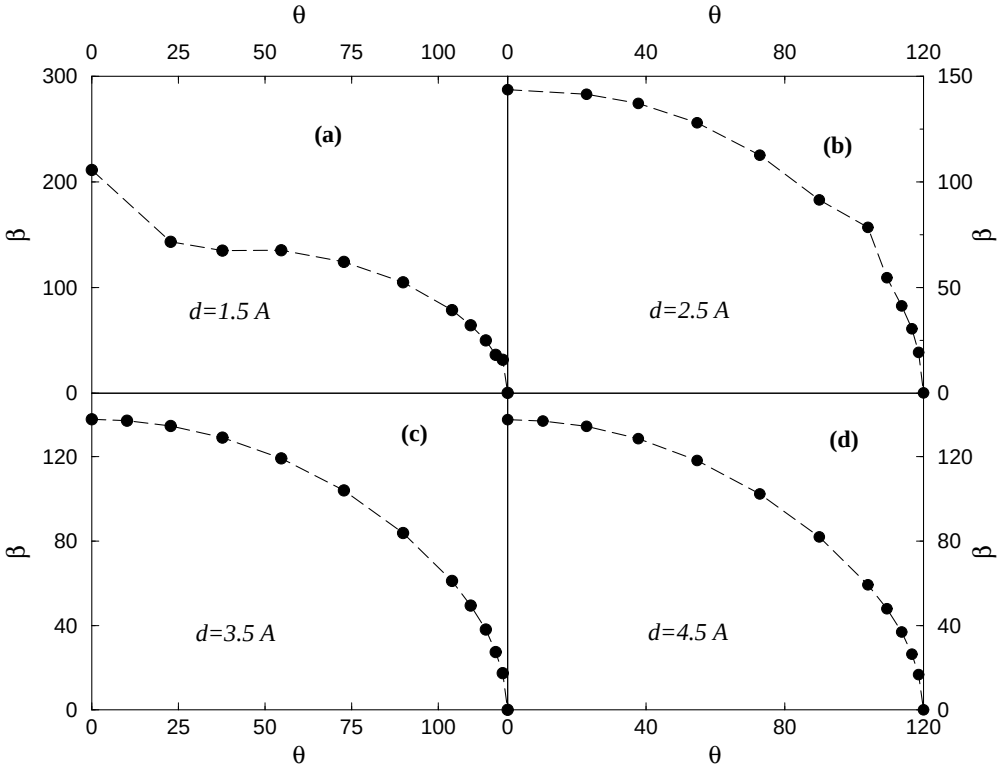

which also decay monotonically to zero at $\theta = 120$. The β value for distances $3.5\mathring{A}$ and $4.5\mathring{A}$ are shown in Fig. 4.7(c) and Fig. 4.7(d), respectively for the parallel dipolar assembly.

The frustrated dipolar assembly (case B in Fig. 4.1) also exhibit very similar qualitative trends. For a small inter-dipolar distance of $1.5\mathring{A}$, β decays with the increase in the inter-dipolar angle till $\theta \approx 30^0$ (Fig. 4.8(a)). Such a steep decrease is also due to the increase in the optical gap at such inter-dipolar angles. However, after the saturation of the optical gap, β is entirely controlled by the dipole moment which increases with the increase in the dipole moment (Fig. 4.4). At larger inter-dipolar distance of $2.5\mathring{A}$ (Fig. 4.8(b)), $3.5\mathring{A}$ (Fig. 4.8(c)) and $4.5\mathring{A}$ (Fig. 4.8(d)) where the optical gap saturates, β shows a monotonic increase with the increase in the inter-dipolar angle again due to similar features in dipole moment (see Figure 4.4).

4.7 Analysis of calix[3]arenes

Until now, the case for a model system of $(HF)_3$ with three dipolar units has been discussed. Molecular species like calix[3]arenes have a similar arrangement for the chromophores and by suitable functionalization at either end of these constituent units, these chromophores can be made dipolar. A simple prototype calix[3]arene that can serve as the model for any other higher order (n>3) and more involved examples of such calix[n] arenes is considered here. Fig. 4.9 shows the two molecules (i) and (ii) that have been considered for the computations. The geometries were optimized at the *ab-initio*

Figure 4.8: Variation of β with respect to the inter-dipolar angle at varying inter-dipolar distances for frustrated orientation at TDHF/6-31G(d,p) level. β is in atomic units.

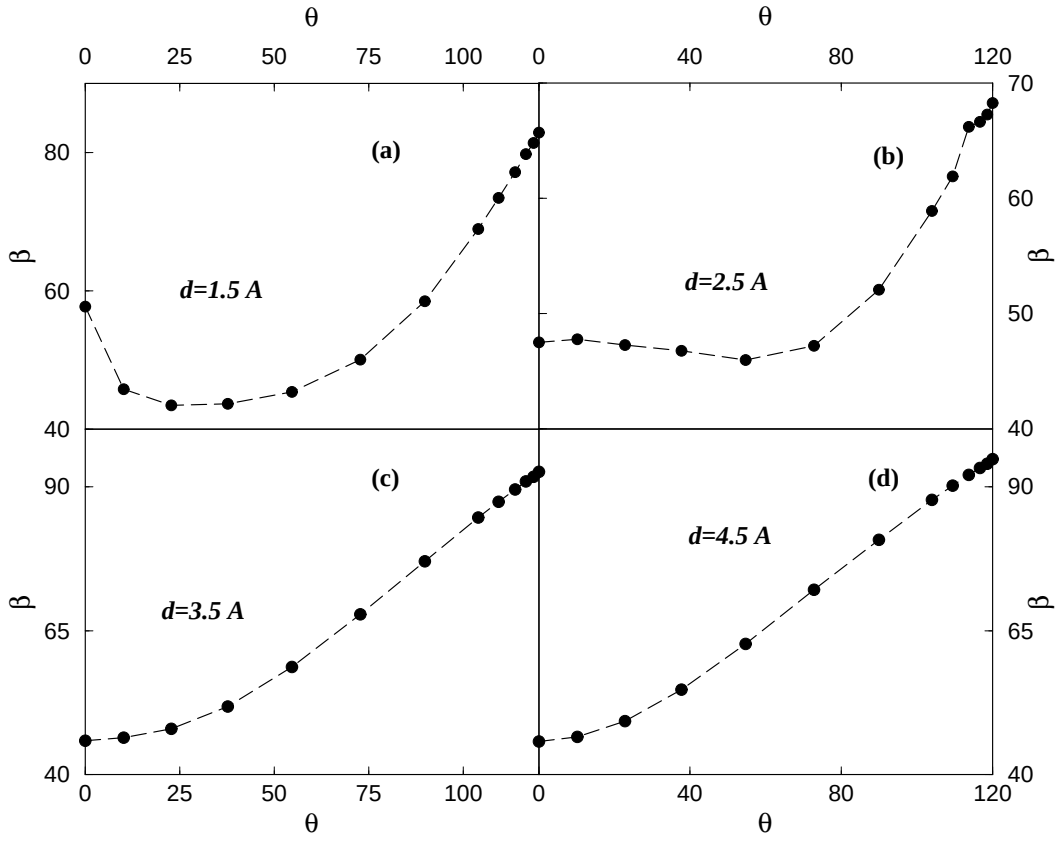

level using the B3LYP method at a 6-31G++(d,p) basis set. The geometry optimized synthon, $(CH_3)_3$C-Ph-NO_2, is also shown. Such a monomer is selected, because, the steric interaction between the *tert*-butyl groups will prevent the aggregate to flatten. Additionally, three synthons are connected by -CH_2-CH_2-CH_2- units. Such a linker is useful, since, it is optically inert and does not involve in extended π-conjugation between the chromophores. Thus the changes in the optical properties in the aggregate and the individual monomer can be understood within the excitonic model.

(i) has a parallel orientation for the dipoles. As can be seen from the structure, the monomers do not make the same phase angle with each other as the structure relaxes from the exact parallel arrangement to a relaxed geometry. For (ii), a similar case of frustrated dipolar geometry is considered that has been discussed earlier in the context of $(HF)_3$. Two of the $(CH_3)_3$C-Ph-NO_2 moieties are parallel while the third one remains anti-parallel to the other two. Energy minimization for the structure leads to a relaxation from the all unidirectional orientation. The dipole moment of the monomer is 5.92 D while the aggregate (i) has a dipole moment of 13.1 D. One can calculate the average cone angle, θ_{ij} for such an arrangement using equation (4.2), as both μ_G and μ_i are known. It is found that for structure (i), θ_{ij}=71.57^0. Note that, the individual dipoles do not make an uniform angle with respect to each other and thus θ_{ij} is not an uniquely defined angle due to relaxation in the optimized structure. This is true for all the real molecular architectures in calix[n]arenes. However, θ_{ij} does provide a very simple "thumb-rule" parameter for defining the cone angle and the dipole interaction for such otherwise complicated geometries. For (ii), the net dipole moment for the aggregate is

Figure 4.9: Structure of the synthon, $(CH_3)_3$-Ph-NO_2; (i), the all-parallel dipolar aggregate; (ii), the frustrated dipolar aggregate; (iii), geometry from crystal structure of a molecule in all-parallel arrangement of dipoles. H not displayed in (i),(ii) and (iii) for sake of clarity. The light green arrow shows the direction of the computed dipole moment. Atom color code: H=white, C=black, N=blue and O=red.

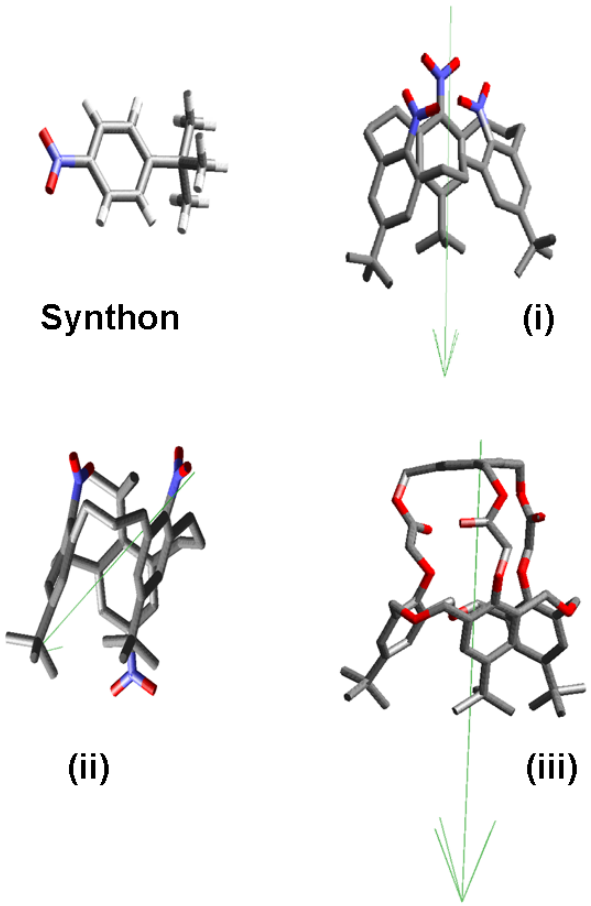

4.67 D, less than that for a single molecule and the dipolar axis for (ii) (seen as a green arrow) does not coincide with the cylindrical axis of the geometry. Using equation (4.3) for (ii), θ_{ij} is found to be 67.80^0.

For these molecules, the SCF MO energies and then the spectroscopic properties were computed using the Zerner's INDO method. The levels of CI calculations are varied, with singles(SCI) and multi-reference doubles CI (MRDCI), to obtain a reliable estimate of the second order optical response functions. All the calculations have been performed for the frequency 1064 nm corresponding to the Nd:YAG laser.

For the parallel arrangement of the monomers, (structure (i) in Fig. 4.9) excitonic splitting due to dipole-dipole interactions is substantial, $\Delta\beta$ ($\beta_{molecule}$ - $3\beta_{monomer}$) = 705 au (see Table. 4.1). Note that there is a large increase of β compared to its monomer value of 7593.2 au, even though inter-dipolar angle, θ_{ij}, is quite large. However, for structure (ii), $\Delta\beta$ = -3734.1 au, supporting the fact that dipolar axis and the cylindrical axis do not coincide due to relaxation of the structure.

For a more conclusive comparison of the evolution of the 1^{st} hyperpolarizability with respect to the inter-dipolar angle, the magnitude of β with the increase in the inter-dipolar angle, θ_{ij}, is computed. This is done by removing the -CH_2-CH_2-CH_2- connectors between the chromophores and then flattening the calix[3]arene similar to what has been done for $(HF)_3$. The profile is shown in Fig. 4.10. $\beta_{calix[3]arenes}$ shows a monotonic decay with the increase in the inter-dipolar angle and decays to zero at θ = 120. It is very interesting to note that similar features appear for the all-parallel $(HF)_3$ assembly too. Thus the $(HF)_3$ model system serves as a very good template

for studying interactions in real supramolecular assembly.

4.8 CSD search

For high NLO responses, the inter-molecular conformation of the dipoles should be parallel or almost parallel. To find real molecular systems where such a single orientation is possible, a search was carried out using the keyword 'calix[3]arene' in the Cambridge Structural Database [73] (CSD version, 5.25, November 2003 release). Structures of low quality (R > 10 %), disordered or in which the position of H atoms have not been determined, were excluded. A total of 4 structures were reprieved. Of these, two of the structures, CSD code: DIPWEE [74] and QETWAN [75] maintain a parallel-like orientation of the monomer chromophores. These two molecules maintain such a parallel arrangement for entirely two different reasons. DIPWEE has a large cavity size that incorporates a fullerene which prevents crossover to the frustrated dipolar form. However, due to large cavity, it gives rise to a large cone angle conformation. From the analysis based on the $(HF)_3$ geometry, it has been shown that structures with a large cone angle are not suitable for efficient NLO applications. Thus, the calculations for this molecular crystal was not pursued further.

Table 4.1: Ground state dipole moment (in Debye) and first hyperpolarizability (in atomic units) for individual constituent and their aggregates in calix[3]arenes.

Molecule	μ_G	β
$(CH_3)_3$-Ph-NO_2	5.920	7589.727
(i) trimer: parallel	13.093	23474.100
(ii) trimer: frustrated	4.670	19035.087
(iii) trimer: crystal geometry	6.650	32076.640

QETWAN, on the otherhand is the simplest yet extremely interesting. The structure has been shown in Fig. 4.9 (iii). It has all the three individual chromophores in the same parallel orientation. The fourth chromophore on the top is functionalized at the *meta*- positions such that it acts as a stitch for the rest of the three and forces a parallel orientation for the dipoles through 'conformational locking'. The light green arrow is the ground state dipole moment axis and it passes almost exactly through the central axis of this basket and thus is very suitable candidate that supports our dipolar model based on $(HF)_3$. The compound has the highest magnitude for the 1^{st} hyperpolarizability among all the systems considered for this work (β = 32076.64 au).

4.9 Conclusions

In this chapter, an analytical theory for the variation of the ground state dipole moment on the orientation of the dipoles with cyclic boundary conditions has been developed. 'Cone-angle' is proposed as a unique parameter by

Figure 4.10: Variation of β with respect to the inter-dipolar angle for the parallel orientation of the monomers in calix[3]arene at the ZINDO/MRDCI-CV level. β is in atomic units and θ is in degrees.

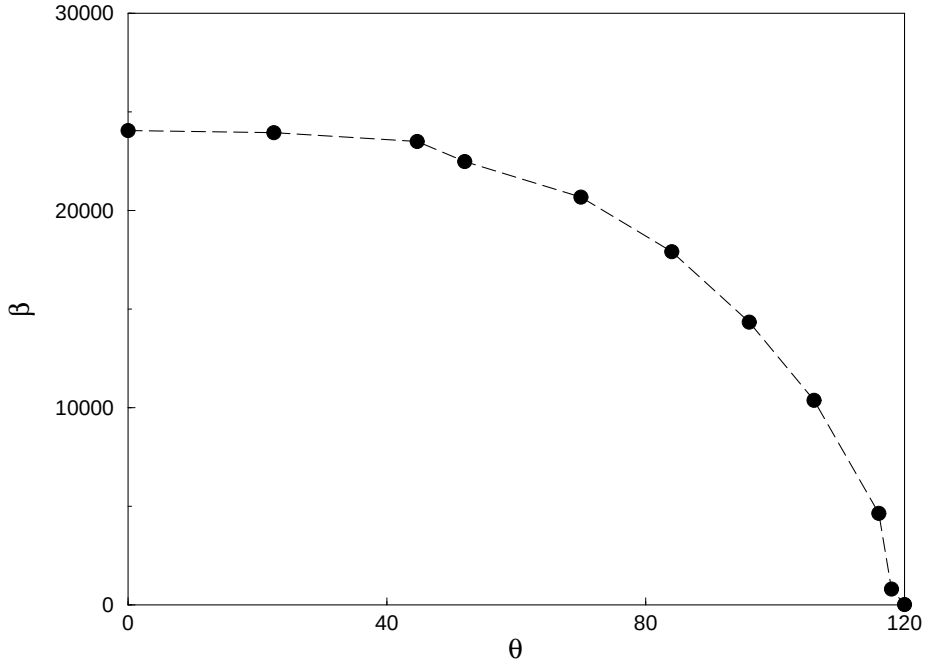

which many interesting phases of aggregation can be derived. The numerical calculations for the ground-state dipole moments on the small model dipolar aggregates of $(HF)_3$ (parallel and frustrated cases) show that these analytical expressions are very reliable provided the molecular orbitals of the individual species do not overlap with each other.

The numerical calculations for the optical properties like β show a very large role of excitonic splitting at small dipolar distances, as a result of which, β decays very rapidly. At large inter-dipolar distances, however, β shows a monotonic decrease due to similar decrease in the ground state dipole moment. The calculations provide the means of finding nonlinear polarizabilities for various cone angles, applicable for real molecular entities. Finally, the calculation on calix[3]arenes show that indeed the dipolar orientation model is very suitable for studying actual molecular baskets where the conical symmetry is preserved.

Chapter 5

Dipole Orientation Effects in oxo-bridged dinitroanilines and odd-even oscillations in nonlinear optical responses in alkyl bridged dichromophores

5.1 Introduction

From the discussions in the previous chapter in the context of calix[3]arenes, it is clear that the NLO properties of aggregates of chromophores connected through -$(CH)_2$ or oxygen atom can be understood reasonably well through the exciton theory. These connectors, in fact, act as harmless stitches. However, since they are flexible, lead to many different orientations in the dipoles.

The NLO responses of these orientations would be expected to be different due to various dipolar phase combinations. For a clear understanding of the effects of such specific orientations, the NLO properties of a few dipolar chromophores are calculated in this chapter.

The case for a dimer composed of D-π-A molecules like paranitroaniline (PNA) that are connected through an oxygen bridge is first discussed. The molecule considered is PNA-O-PNA. The interest in this system stems from the fact that the two PNA molecules can be arranged in side-by-side fashion through connectivity in the *ortho*-position by an oxygen atom resulting in a non-centrosymmetric system. Similar compounds have been synthesized by several groups [76, 77]. However, due to the sp^3 hybridized nature of the bridged O-atom, the interdipolar angle is quite large. This in turn reduces the hyperpolarizability for the dimer from the additive values of two monomers. However, it is proposed that a new molecule where the monomers are connected by an additional C-C linkage leads to *conformational locking* of the monomers in almost an all-parallel orientation, resulting in large hyperpolarizability for the dimer.

In the next case, two dipolar chromophores are considered that are separated by an alkyl bridge. The number of groups in the alkyl bridge is varied to obtain a quantitative estimate of the orientation of the dipoles, together with its effect on NLO properties of the system. Since, dipolar orientations are strongly dependent on the conformations of the intervening methylene groups, the overall dipole moment as well as the 1^{st} hyperpolarizability (β) show an odd-even oscillations with the variation in the number of methylene groups. Such odd-even oscillations are well-known in literature for many

physical properties like the melting points of organic solids [78] and the orientation of alkanethiols in self-assembled monolayers (SAMs) [79]. Also, there have been recent experimental reports of odd-even oscillations in NLO properties of organic molecules similar to those discussed here [80] and even in different molecular systems [81].

The oscillations in the physical properties such as melting point are generally understood on the basis of packing efficiencies in the van der Waals solids. The alkanes with odd-number of carbon atoms are packed less orderly than their even counterparts. However, oscillations in the electrical properties like hyperpolarizabilities are difficult to understand as they are very sensitive to both the nature of ground state and the excited states. Herein, it is shown that such oscillations arise due to conformational flexibility of the intervening alkane chains between the dichromophores[1].

5.2 O-bridged PNA dimer: PNA-O-PNA

The ground state optimized structure for such a molecule is shown in Fig. 5.1(A). The two PNA molecules are orientated in two different planes with an interdipolar angle (ϕ)of 43.4^0, calculated at the AM1 (Austin Model 1) level. Additional frontier orbital analysis shows that there is almost no overlap within the π-electrons of the two PNA rings [82] and thus, the dipole moment of the dimer can be accurately described by the classical vector addition scheme with an appropriate phase factor.

Fixing one PNA molecule and rotating the other PNA molecule along the

[1]Papers based on the work reported in this chapter have appeared in (1) *J. Phys. Chem. A* **108**, 320 (2004). (2) *J. Phys. Chem. A* **109**, 4112 (2005).

Figure 5.1: (A) Ground state optimized structure of PNA-O-PNA at the AM1-level. ϕ represents the interdipolar angle (B) Optimized structure of PNA-O-PNA bridged through C-C linkage at *meta*-position. (C) Molecular structure of PNA-O-Si$(CH_3)_2$-O-Si$(CH_3)_2$-O-PNA as retrieved from the Cambridge Crystallography Database (CCDC).

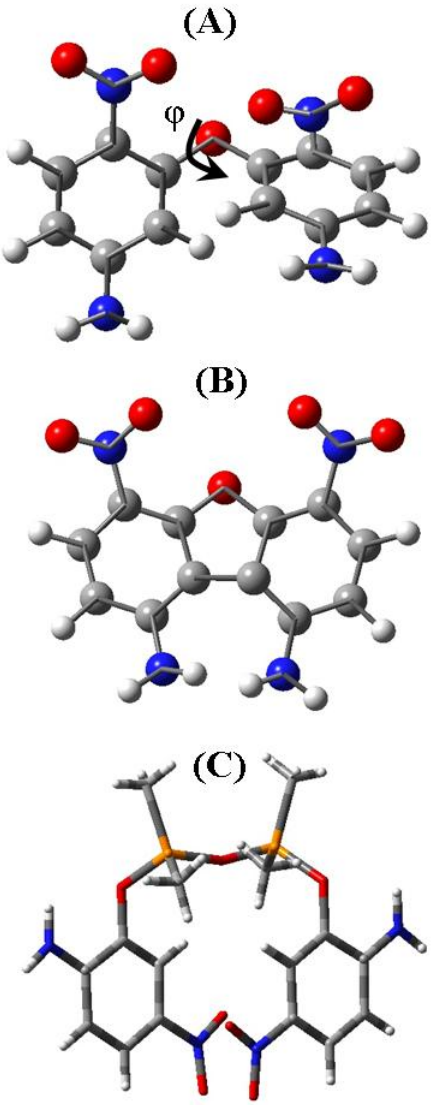

O-PNA axis changes the interdipolar angle (ϕ) from 0 to 120 degrees. The conformation for ϕ=0^0 corresponds to the parallel side-by-side arrangement of the dipoles while ϕ=120^0 corresponds to an almost anti-parallel arrangement. Thus, it is interesting to ask what happens to the second harmonic response of the molecular dimer as one changes the interdipolar angle (ϕ). Molecules with different interdipolar angles can be synthesized by suitable substitution of alkyl groups on the rings that can stabilize specific orientations of ϕ or by replacing one of the PNA rings by meta-nitroaniline (MNA) or ortho-nitroaniline (ONA).

In Fig. 5.2 (Top panel), the total ground state dipole moment μ_G (in Debye) for PNA-O-PNA is plotted with variation in the interdipolar angle. As can be seen, the dipole moment decreases with increase in the interdipolar angle. This can be easily understood by considering the combined effects of ground state dipoles of each monomer. If the two dipoles are parallel and in the same plane, the *in-phase* combination (ϕ=0^0) of the resultant dipole is the sum of the two individual dipoles.

The bridged oxygen atom in fact does not play any significant role in determining the nonlinear optical coefficients. It basically controls the distance between the two nitroaniline dipoles. Due to its high electronegativity, it just increases the total dipole moment of the dimeric systems (it is roughly 1 Debye increase purely because of oxygen) to the same extent for all values of the dihedral angle, ϕ. The minimum distance between the dipolar axes of the molecules is more than 4 $\mathring{A}$, thereby, ensuring that no explicit intermixing of the π molecular orbitals of the chromophores occur validating the exciton theory based on the dipole-dipole interaction model as discussed in chapter

Figure 5.2: [Top Panel] Variation of the ground state dipole moment (μ) (in Debye) with increase in the interdipolar angle (in degrees). [Lower Panel] Variation of the EFISH coefficient ($\mu\beta$) (in esu-units) with increase in the interdipolar angle (in degrees).

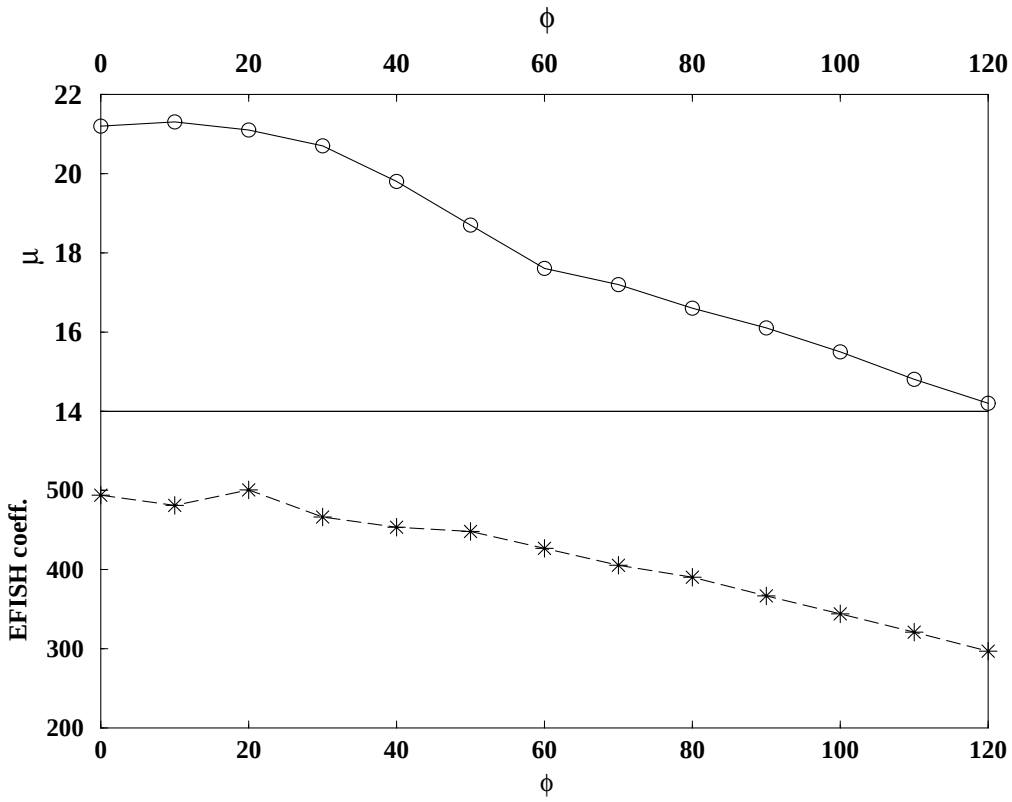

2. Thus, even though the semi-classical theory of dipole-dipole interaction does not take into account the electronic properties of the bridged O atom, it is found that the qualitative trend in splitting energy as a function of the angle, ϕ, is almost the same with those obtained from singles-configuration interactions (SCI) calculations for the di-nitroaniline systems.

For the calculations of the optical coefficients, an excitation frequency of 1064nm (1.17eV) which corresponds to the frequency of the Nd-YAG lasers is used. The variation in EFISH (electric field induced second harmonic coefficients) coefficients with the increase in the dihedral angle (ϕ) is shown in Fig. 5.2 (Lower Panel). The trend is very similar to that for the ground state dipole moment in Fig. 5.2 (upper panel). To be precise, the magnitude of EFISH coefficient decreases with increase in the torsional angle for the PNA-O-PNA.

The results compare fairly well with the experimental values reported earlier. For example, the calculated β for the optimized geometry *Bis (2-amino-4-nitrophenyl) ether* (ϕ=43^0) is β=16.4×10^{-30}esu. The experimental value for the same molecule with Hyper-Rayleigh Scattering (HRS) technique at the Nd:YAG frequency has been reported to be 22.0×10^{-30}esu [76].

A very important aspect of the above discussion is to design the di-nitroaniline system so that the maximum NLO activity can be attained. The highest EFISH coefficients (494.4×10^{-30}esu) is obtained for PNA-O-PNA with zero dihedral angle. Such a high value of EFISH coefficient is not possible to be realized from the PNA-O-PNA molecular system as the optimized geometries of the di-nitroaniline molecules discussed above are not planar due to steric repulsions. Therefore, the best way to achieve this would

be is to connect the oxo-bridged rings by a carbon-carbon bond in the *meta* position. Optimizations of this structure, (shown in Fig. 5.1 (B)) at the AM1 level of theory, confirms that the nitroaniline rings are almost planar with the dihedral angle ϕ very close to zero. Thus one can make the two dipoles parallel to a large extent by bridging the two rings by a covalent bond. The EFISH coefficients for this bridged structure is 471.5×10^{-30}esu, which is close to the parallel ($\phi = 0$) PNA-O-PNA dipole value of 494.4×10^{-30}esu [82].

To further verify the existence of dimers of PNA, a detailed search for such structures in the Cambridge Crystallographic database was performed. A very interesting system, similar to our theoretically considered structure is found to be PNA-O-Si$(CH_3)_2$-O-Si$(CH_3)_2$-O-PNA (CSD id: TOFPIN.cif) (see Fig. 5.1 (C)) [77], where the monomers are connected by a siloxane bridge. Presence of such siloxane backbone provides large thermal stability and mechanical strength to the dimer. Being rigid, this backbone locks the two monomers in non-centrosymmetric orientations with an interdipolar angle of 36^0.

5.3 Study on Dipole-$(CH)_2$-Dipole

To understand the relationship between SHG coefficients and the geometrical orientations of the intervening methylene groups in dipole-$(CH)_2$-dipole systems, a set of molecular systems are considered as shown in Fig. 5.3 (A). All the geometries have been optimized using the AM1 parameterized Hamiltonian available in the Gaussian 03 set of codes. Some of the compounds (with smaller alkyl units) have already been synthesized in good yields and well

Figure 5.3: (A) Molecular structure of the system considered; (B) Orientation of the dipoles for odd and even chains.

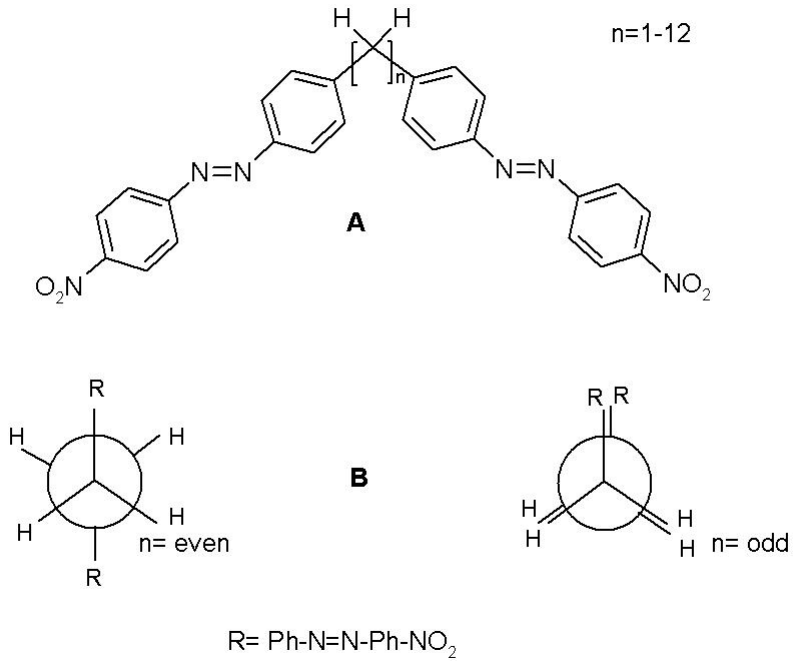

characterized, although, single crystalline forms are not available. The geometries obtained by the AM1 calculations have been compared with those obtained using the DFT based methods at B3LYP/6-31G+(d,p) level for the smaller sized chromophore with n=2. It is found that the geometries obtained by both the methods have similar bond lengths and bond angles. To further verify that the geometries do correspond to the global minima, the geometry for an experimentally synthesized molecule very similar to one considered by us: 4,4′-Diamino-2,2′-dinitrodiphenylmethane [83] is also optimized. Even at the AM1 level, the geometry and the bond lengths/angles turn out to be same as found experimentally (XRD data).

R-CH_2-CH_2-R, R=Ph-N=N-Ph-NO_2, is the simplest symmetric case which can be considered to understand the conformational orientations, as shown in Fig. 5.3 (B). Rotation along the central C-C bond produces different conformations. For a torsional angle, ϕ=0, the situation corresponds to an eclipsed geometry while for ϕ=180, the conformation is staggered. In Fig. 5.4, the potential energy profile for the system with increase in torsional angle is plotted. The most stable point in the potential energy surface (PES) corresponds to ϕ=180 (staggered orientation in the dipoles) while the most unstable case corresponds to ϕ=0 (the eclipsed form). Also, there exists a local minima between ϕ=60 and 80 and a local maxima at ϕ=120. This is similar to the *gauche butane* interaction well-known in literature [63, 84]. This arises due to the stronger non-bonding interaction between R and H at an angle of ϕ=120, compared to the weak R, R interactions in the gauche form at $\phi \approx$ 60.

For $n = 2$, the energy difference between the staggered and eclipsed form is 8 kcal/mol while that between the staggered and the gauche form is 1.04 kcal/mol. For comparison, the differences are 4.4-6.1 kcal/mol and 0.9 kcal/mol respectively for butane. For a longer chain, however, since there are more number of CH_2 groups, the degrees of freedom are much larger, allowing it to be in a state of random relaxed geometry without much constraints. In the same figure (Fig. 5.4), the PES for the longest chain considered in the work: n=12 is also plotted. Note that, for such a large methylene bridge, there is no well-defined torsional angle parameter. However, for the sake of comparison, the central C-C bond, C(6)-C(7) is twisted. It has a lower energy difference between the staggered and eclipsed form (6.5 kcal/mol) and

between the staggered and gauche form (0.84 kcal/mol), as expected.

For both n=2 and n=12, the energy difference between the eclipsed and the staggered forms are more than the thermal energy at room temperature. The staggered form is the lowest energy orientation for all the systems in the n=even cases. However, since the gauche conformation lies at a local minima, for longer chains, this conformational form becomes thermally accessible. A gauche form is interesting because it induces helicity in a linear chain. Such helical chains being chiral has been shown to exhibit good NLO responses [85–87].

The odd-chains however, show remarkable contrast. For the odd-chains, the favorable arrangement corresponds to an eclipsed orientation for the dipoles. This is explicitly shown in Fig 5.3 (B). One can understand this phenomenon from the simple fact that all the alkyl units being in sp^3 environment introduce staggered geometry for all central units but eclipsed orientation between the extreme ends where the dipoles are located. So, the odd-chains will have an eclipsed orientation for the dipoles. For the even chains, however, there is no such frustration in the dipole orientations and all the units including the end dipoles remain staggered. Such a remarkable variation between the eclipsed and staggered conformation can be achieved by only changing the number of spacers between the dipoles.

Figure 5.4: Potential energy (in kcal/mol) as a function of twist along the central C-C single bond: for n=2, solid line (circles) and n=12, dashed line (diamond).

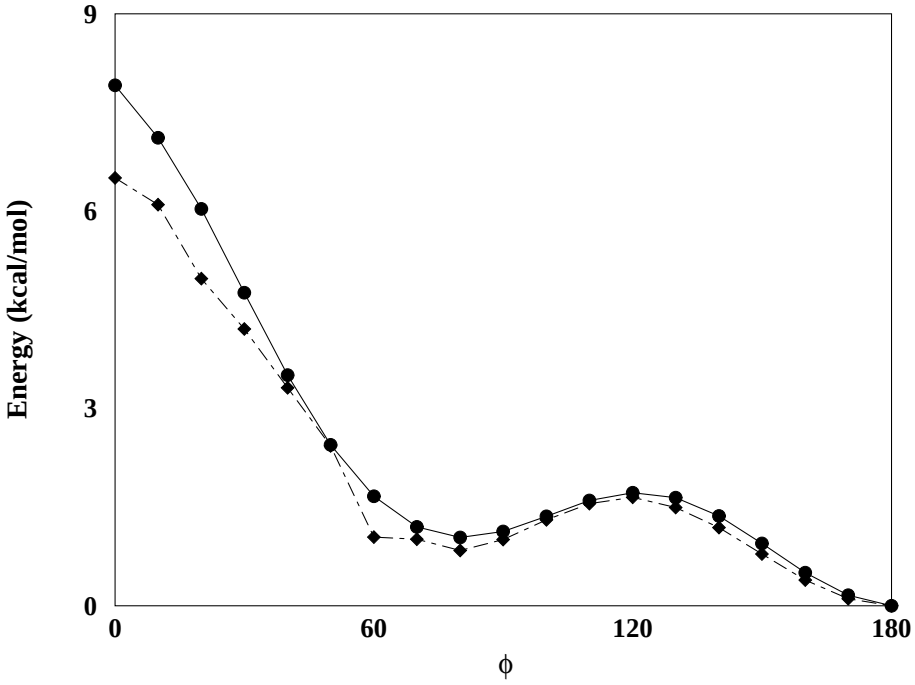

5.4 Optical response functions: Role of spacer length

The geometries [shown in Fig. 5.3 (A) with varying n] obtained from the AM1 calculations are used to compute the SCF MO energies and then the spectroscopic properties using the ZINDO/Correction vector method.

In Table 5.1. the magnitudes of the ground state dipole moment (μ_G), oscillator strength (f), the optical gap (δE) [defined as the energy difference between the ground state and the lowest energy dipole allowed state], linear polarizability ($\bar{\alpha}$) and 1^{st} hyperpolarizability ($\bar{\beta}$) are reported for the molecules from n=1 to n=12. Note that, the tumbling average quantities are reported for the optical response functions, defined as

$$\begin{aligned} \bar{\alpha} &= \frac{1}{3}\sum_i(\alpha_{ii}) \\ \bar{\beta} &= \sqrt{\sum_i \beta_i\beta_i^*}; \quad \beta_i = \frac{1}{3}\sum_j(\beta_{ijj}+\beta_{jij}+\beta_{jji}) \end{aligned} \tag{5.1}$$

where the sums are over the coordinates x, y, z $(i, j = x, y, z)$ andβ_i^* refers to the conjugate of β_i vector. All the calculations have been performed at a frequency of 1064 nm (1.67 eV) corresponding to the Nd:YaG laser. It is found that that while the linear polarizability ($\bar{\alpha}$) remains almost constant throughout the series ($\approx$ 1550), the ground state dipole moment as well as the 1^{st} hyperpolarizability ($\bar{\beta}$) show strong odd-even oscillations. Specifically, $\bar{\beta}$ shows an order of magnitude increase for odd chains compared to the even

chains. Furthermore, their values remain almost constant with the increase in the number of CH_2 spacers, n, albeit for n=odd and n=even separately. The even chains have very little dipole moment ($\approx$ 3 D) while it is orders of magnitude higher ($\approx$ 45 D) for the odd chains. The dipole moment for the single molecule, Ph-N=N-Ph-NO_2 is calculated as, $\mu_G \approx 39.20$ D. For a perfect parallel arrangement in the dipoles, the classical non-interacting picture predicts the total dipole moment as 2$\times$ single chromophore value and 0 for a perfect anti-parallel arrangement.

Table 5.1: The oscillator strength (f), optical gap (δE) in eV, ground state dipole moment (μ_G) in Debye, linear polarizability ($\bar{\alpha}$) in units of 10^{-24} esu and 1^{st} hyperpolarizability $\bar{\beta}$ in units of 10^{-30} esu for the chromophores in Fig. 5.3 (A), with increase in spacer length.

Spacer	f	δE	μ_G	$\bar{\alpha}$	$\bar{\beta}$
n=1	2.01	4.25	44.40	1500.48	537.06
n=2	2.59	4.42	3.02	1561.44	73.03
n=3	1.78	4.34	46.32	1475.04	614.24
n=4	2.52	4.43	3.36	1560.96	50.91
n=5	1.72	4.43	45.12	1539.36	647.88
n=6	2.50	4.43	3.58	1556.64	48.38
n=7	1.82	4.44	42.34	1488.96	813.08
n=8	2.66	4.46	3.50	1490.88	93.31
n=9	1.56	4.43	47.47	1540.8	636.36
n=10	1.83	4.43	2.35	1555.2	70.73
n=11	1.62	4.43	43.73	1610.4	594.89
n=12	1.84	4.43	3.84	1618.56	73.26

While for the even spacers the dipole moments are nearer to zero (the molecules are rod-shaped), the odd-spacers show much smaller value from the classical result of twice the single chromophore value. Such a trend can be easily understood: for the even chains, the dipoles are staggered and almost perfectly anti-parallel, however, for the odd chains, even though the orientations are eclipsed, the dipoles are not exactly parallel because of the sp^3 hybridization along the alkyl principle axis (the molecules are banana shaped). It is straightforward to calculate the angle (ϕ) using the

classical dipole addition formula: $\mu_{eff}^2 = \mu_1^2 + \mu_2^2 + 2\mu_1\mu_2 cos\phi$. ϕ is calculated as 110 degrees for the odd chains. Note that, although a classical dipole expression is used to find the phase angle, it comes out as a good assumption as the saturated CH_2 groups have very little electronic coupling with the π-electrons in the either ends of the bridge. For example, the actual angle for the optimized molecule with n=3 is 112 degree. Very similar to the oxygen atom in the oxo-bridged PNA dimer system, discussed previously in this chapter, the alkyl units in this case basically act as stitch between two dipoles.

With the increase in the number of alkyl units, the distance between the dipoles increases. But, the distance between the even dipoles is more than their odd counterparts as the even ones have a centrosymmetric arrangement which increases their interchromophore distances. Thus, the end-to-end distance between the dipoles also exhibit an odd-even effect (Fig. 5.5 (a)). For each even distance, $\bar{\beta}$ is smaller and for each odd distance, $\bar{\beta}$ is larger. Fig. 5.5 (b) shows the variation in the 1^{st} hyperpolarizability, $\bar{\beta}$, with respect to the number of CH_2 units. Very similar to that for the ground state dipole moment, $\bar{\beta}$ also shows a very prominent odd-even oscillation. For odd chain, $\bar{\beta} \approx$ 700 while the even chain have $\bar{\beta} \approx$ 80 (in units of 10^{-30} esu). The calculations are based on a CI basis with its dimension varying till a proper convergence is reached.

Within the two-state model, the SHG coefficient is directly proportional to the oscillator strength and the dipole moment difference and $\bar{\beta}$ is inversely proportional to the optical gap. Thus, any phenomenon that decreases the gap or increases the dipole moment difference between the ground and the

Figure 5.5: (a) Variation of interchromophore distance, d (in $\mathring{A}$), (b) 1^{st} hyperpolarizability $\bar{\beta}$ (in units of 10^{-30} esu), (c) Difference between the ground state and the excited state dipole moment, $\Delta\mu$ (in Debye) with the increase in the spacers length, n.

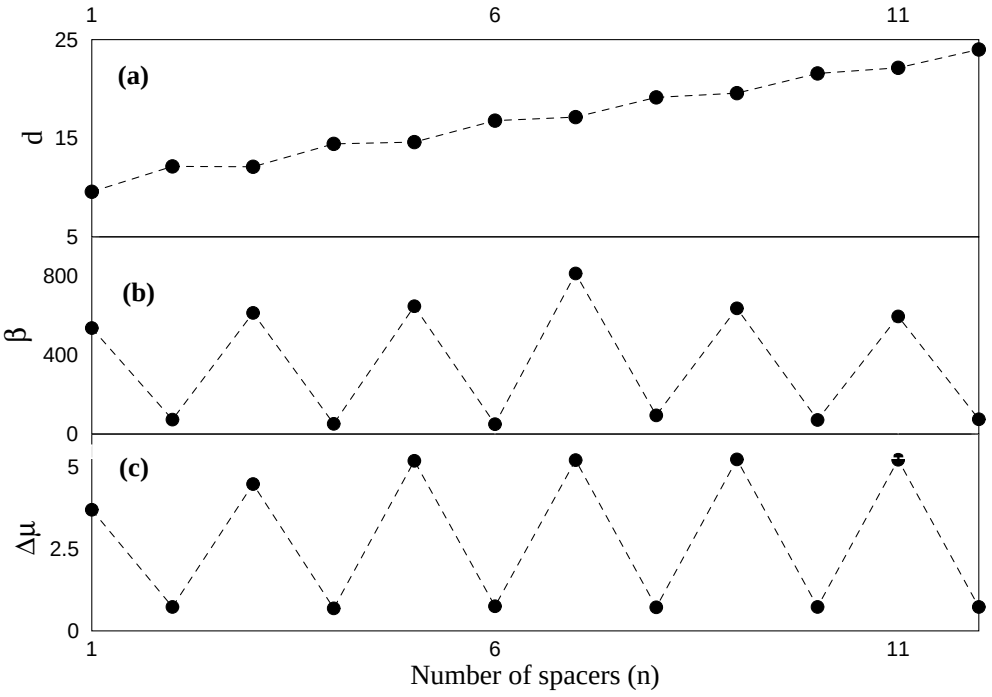

excited state or increases the oscillator strength will enhance $\bar{\beta}$. The calculations show that both the optical gap (δE) as well as oscillator strengths almost remain same for the even and odd chromophores (seen in Table. 5.1). Thus, the only factor that governs such an odd-even oscillation is the $\Delta\mu$. Fig 5.5(c) shows the variation of $\Delta\mu$ with increase in the spacer length. One can clearly see the odd-even variation in $\Delta\mu$ similar to that observed for $\bar{\beta}$. This is to say that the excited state polarization has a strong dependence on the interchromophoric arrangement.

5.5 Conclusions

To conclude, it is found that for dimers of dipolar molecules like PNA-O-PNA, the perfect side-by-side arrangement of the dipoles leads to a large hyperpolarizability, with a small torsional angle (ϕ) between the dipoles. It is shown in this chapter that one can achieve such a constrained environment by additionally connecting the dipoles by the C-C bridge.

Additionally, the odd-even fluctuation in the SHG for dipoles connected through alkyl bridge is analyzed. This phenomenon is found to be different from the variation of the physical properties like melting point in organic solids that have their origin in the van der Waal interactions among the molecules where crystal packing is the most important parameter. The potential energy analysis of twisting along the single bond shows that although the staggered form is the most stable geometry for the even chains, a thermally allowed local minima exists between ϕ=60-80, corresponding to the gauche form with helical structure. For example, it is found that for every

100 molecules in the staggered form, there are 18 molecules in the gauche form (corresponding to the Boltzmann distribution at room temperature) and even for the n=2 case, the Boltzmann weighted average of 1^{st} hyperpolarizability, β, has a magnitude of 160.8×10^{-30} esu. In the solid state due to environment effects, the possibility of existence of such a helical form (local minima) exists. As a result, for the even chains although a global minima form ensures β to be very small, supramolecular effects as in thin-films will introduce appreciable β.

This phenomenon is, however, a consequence of the interactions in a single alkyl chain. In crystals or thin films, intermolecular interactions will be important and packing efficiency will ultimately decide the final geometries. But, the fact that a simple theory based on intramolecular interactions can capture this effect indicates that at least, for these molecules, intramolecular interactions are quite important in the macroscopic scale.

Chapter 6

Non-linear optical properties of all-metal clusters and π-isoelectronic organic molecules: Charge transfer and delocalization effects

6.1 Introduction

The NLO properties of organic π-conjugated materials depend crucially on the delocalization of the π-electrons over the σ-backbone. The first and second hyperpolarizabilities, β and γ for the π-conjugated polymers increase with the conjugation length (L) roughly as L^3 and L^5 respectively [88]. Therefore, the general strategy to model NLO materials has been to increase

the conjugation length. However, there exist an upper limit for every off-resonant susceptibilities [89]. Alternative to these π-conjugated compounds has hardly been explored theoretically. But, with the gaining popularity of various *ab-initio* level methods [90], there has been a tremendous impetus in investigating the structure and electronic properties of both homogeneous and heterogeneous small clusters in recent years [91, 92].

Small Al_4 rings like Al_4M_4 and their anions $Al_4M_3^-$, M=alkali metals, have been a subject of current interest [93, 94] because of their unique characteristics and close structural resemblance with the C_4H_4. However, although C_4H_4 is an anti-aromatic species, these Al_4-clusters have recently been reported to be σ aromatic [95]. Thus, it would be interesting to ask whether these rings are better polarizable than their organic counterpart; whether the structural characteristics has any role in their polarization response functions. Organic π-conjugated systems are stabilized due to π-electron delocalizations, while the inorganic metal complexes reduce their energy through strong charge transfer. It is described in the following that these metal clusters offer a unique polarization response due to their ionic character and poor σ-π separation, contrary to conventional π-conjugated systems, leading to large optical coefficients[1].

6.2 Geometry Optimizations

The calculations are started by first optimizing the ground state geometries of the Al_4-clusters (Al_4Li_4 and Al_4Na_4). All the optimizations have been done

[1]Paper based on the work reported in this chapter has appeared in *J. Phys. Chem. A* **108**, 9527 (2004).

using the B3LYP//RHF/6-31G(d,p) method available in the GAMESS electronic structure set of codes [96]. Since, it is intended to compare the optical properties of these small four-membered rings with their organic analogue, C_4H_4, the geometry for cyclobutadiene was also optimized. The level of basis set is varied from 6-31G(d,p) to 6-311G+(d), to ensure that these geometries correspond to the global minima in the potential energy surface. Additional frequency calculations are performed to confirm the obtained structures as the ground state geometries. The final geometries indeed remain independent of the selection of the basis set. The ground state structure of C_4H_4 has a rectangular D_{2h} structure with alternate short and long C-C bonds. The structure of the Al_4 skeleton in Al_4M_4 is similar to cyclobutadiene with shorter and longer alternate Al-Al bonds and the counter-ions are so arranged that an overall C_{2h} symmetry is maintained in Al_4M_4.

Table 6.1: The bond length alteration, Δr (in $\mathring{A}$), Optical Gap (in a.u.) and the average Mulliken charge (Δq) on the ring for the clusters from ZINDO calculations.

Molecule	Δr	Gap	Δq
Al_4Li_4	0.1283	0.0819	-0.592
Al_4Na_4	0.1302	0.0909	-0.174
C_4H_4	0.245	0.2410	0.000
C_6H_6	0.000	0.2588	0.000

6.3 Results and Discussions

The linear and nonlinear polarizabilities are calculated by the Zerner's INDO method with multi-reference doubles CI (MRDCI) calculations. The MRDCI is particularly important since it includes correlation effects substantially. All the ZINDO calculations are performed with 4 reference determinants including the Hartree-Fock ground state, at an electrical frequency of 0.001 au, much below any optical resonance. The ZINDO formalism is specifically parameterized so that both the σ and π electrons are explicitly considered. In fact, this method is very essential for studying the Al_4Li_4 and Al_4Na_4 systems for which the σ-π separations are quite poor.

Table 6.1 shows the bond-length alteration (BLA), Δr (defined as the average difference between the bond lengths of two consecutive bonds), the optical gap (energy difference between the ground state and the optically active state i.e, having finite oscillator strength) and the average Mulliken charge on the Al_4 ring for all the geometries.

Figure 6.1: Plot for the electron density in Al_4Li_4.

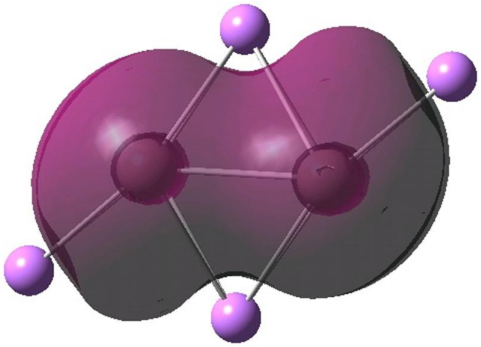

To directly compare the efficiency of these Al_4-clusters with the conventional π conjugated systems, we also calculate the optical properties for cyclobutadiene (C_4H_4) and benzene (C_6H_6) at the same level of theory. It is evident that for the Al_4-clusters, the Δr is very small compared to the C_4H_4 (anti-aromatic) but larger than C_6H_6 (aromatic, Δr =0). For the Al_4-clusters, there is a substantial amount of charge transfer from the alkali atoms to the Al atoms (negative charge), making them act as donor and acceptor respectively. In fact, charge transfer is almost complete from the four Li-atoms to the Al_4-ring. This is clearly seen from the plot of the electron density for Al_4Li_4 (Fig. 6.1). Thus, the Al_4-ring behaves as a formal 4π electron system, π-isoelectronic with C_4H_4.

Such a charge transfer induces polarization in the ground state structure and reduces the optical gap. On the other hand, the C-H bond being perfectly covalent, there is almost no charge transfer in case of C_4H_4 and C_6H_6. These thus have large optical gaps due to finite size molecular architecture.

In Table 6.2, the magnitudes of the ground state dipole moment, μ_G, the linear(α), and nonlinear (β and γ) polarizabilities for the clusters are reported from the ZINDO calculations. Note that we report the magnitudes for the tumbling averaged $\bar{\alpha}$, $\bar{\beta}$ and $\bar{\gamma}$, as defined earlier in chapter 1 (equation 1.33).

The ground state dipole moment μ_G and $\bar{\beta}$ are zero for the C_4H_4 and C_6H_6 due to its perfect centrosymmetric geometry. However, the $\bar{\alpha}$ and $\bar{\gamma}$ being odd-order polarizations, have finite values. For the Al_4-clusters, due to the C_{2h} symmetry of the ground state structure, the dipole moments and $\bar{\beta}$ are zero. The optically active states are the low-energy metallic σ-levels for the Al_4-clusters and the lowest optical gap is about 0.085 au. For the C_4H_4 and C_6H_6, however, the optical gaps are quite large (0.25 au) due to their insulating nature and the transitions are exclusively π-π^* type with no intervening σ-orbitals. Since the optical coefficients are inversely proportional to the optical gaps and proportional to the dipolar matrices, a large optical gap implies low magnitudes for the optical coefficients. C_4H_4 has the highest magnitude of BLA and optical gap and the least charge transfer on the ring structure, thereby smallest magnitude of $\bar{\gamma}$. On the other-hand, although BLA is zero for C_6H_6, due to complete π-electron delocalization, there is no charge transfer in the finite molecular structure leading to large optical gap and weak polarization. Consequently, $\bar{\gamma}$ is also very less for C_6H_6. In contrast, the optical coefficients in general are quite large for the Al_4-clusters. For example, the $\bar{\gamma}$ for the Al_4-clusters are roughly 10^4 times more than that for C_4H_4 and C_6H_6. This is because the $\bar{\gamma}$ is a third order property with 4 dipolar matrices in the numerator and 3 optical gaps in the

denominator [97].

Table 6.2: The ground state dipole moment, $\bar{\mu}_G$, linear polarizability, $\bar{\alpha}$, 1^{st} hyperpolarizability, $\bar{\beta}$ and the 2^{nd} hyperpolarizability, $\bar{\gamma}$ for the clusters and for *trans*-polyacetylene chain from ZINDO-MRDCI calculations. The units are in a.u. 'n' is the number of -$CH = CH$- units.

Molecule	μ_G	$\bar{\alpha}$	$\bar{\beta}$	$\bar{\gamma}$
Al_4Li_4	0.000	5.5×10^3	0.000	5.33×10^8
Al_4Na_4	0.000	8.7×10^3	0.000	2.00×10^8
C_4H_4	0.000	2.9×10^2	0.000	4.76×10^3
C_6H_6	0.000	5.4×10^2	0.000	8.44×10^3
$(CH{=}CH)_n$, n=1	0.000	136.3	0.000	2.78×10^4
$(CH{=}CH)_n$, n=2	0.000	421.0	0.000	4.15×10^4
$(CH{=}CH)_n$, n=3	0.000	852.4	0.000	6.17×10^5
$(CH{=}CH)_n$, n=4	0.000	1455.2	0.000	2.82×10^6
$(CH{=}CH)_n$, n=5	0.000	2203.2	0.000	8.41×10^6
$(CH{=}CH)_n$, n=6	0.000	3074.9	0.000	2.07×10^7

For a clear understanding of energy levels statistics and their characteristics, we look at the MO energies and the corresponding wavefunctions. In Figure 6.2, the frontier molecular orbital levels are plotted for (a) C_4H_4, (b) Al_4Li_4, (c) C_4H_4 and (d) Al_4Na_4. Both C_4H_4 and C_6H_6 have very large gaps and the optical transition occurs from the π to π^* levels which are well-separated from the σ levels. This explains the small $\bar{\gamma}$ for these organic π-conjugated molecule. However, for Al_4Li_4 and Al_4Na_4, the energy levels are very close to each other. In between the π and π^* levels, there are σ levels which effectively reduces the optical gap in these all-metal clusters and thereby results in a large $\bar{\gamma}$. This is also qualitatively understood from the

Figure 6.2: Ordering of the molecular orbitals energies within the cutoff of -10 eV to 10 eV for (a) C_4H_4, (b) Al_4Li_4, (c) C_6H_6 and (d) Al_4Na_4.

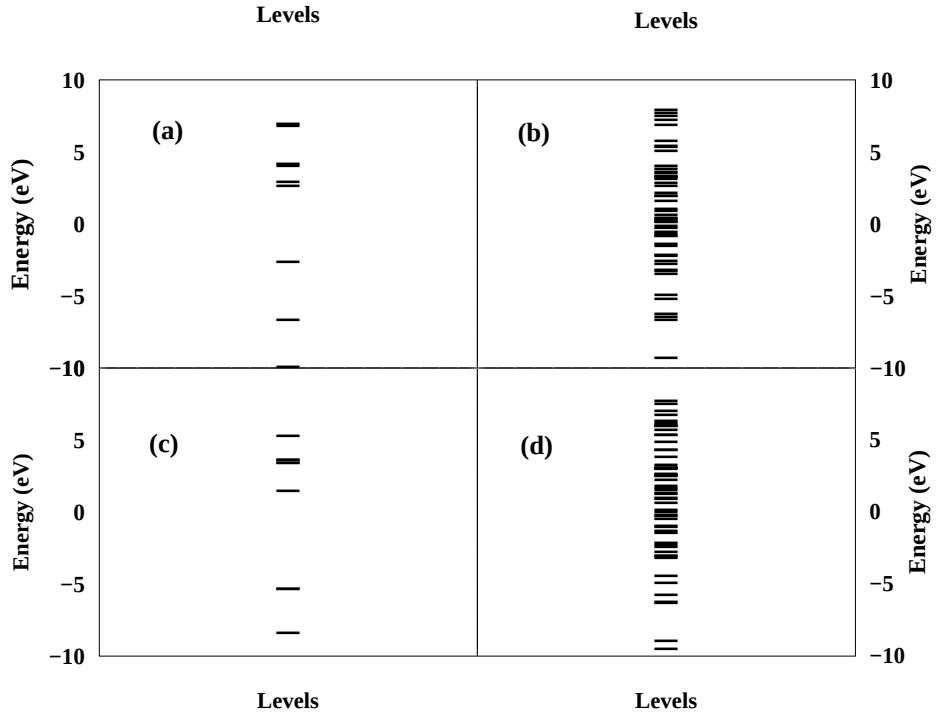

plots of the frontier molecular orbital levels. For Al_4Li_4, the π and the π^* levels correspond to the HOMO-3 and LUMO-3 levels. However, the optical transitions occur within the HOMO-LUMO gaps which are admixtures of π and σ symmetries. Thus, such a poor π-σ separation facilitates to reduce the optical gap for these systems and enhance the NLO responses. The molecular orbital plots as shown in Figure 6.3 indicate the strong π-σ mixing for the frontier orbitals.

To compare and contrast these clusters with their organic counterparts, we calculate the NLO properties of the well-known π-conjugated systems, the *trans*-polyacetylene chain, (-CH=CH-)$_n$, by varying the number of spacers, n, from n=1 to 6, and thereby extending the length of conjugation from 1.35 $\mathring{A}$ to 13.75 $\mathring{A}$. The geometries are optimized by the AM1 parameterized Hamiltonian. The linear and nonlinear polarizations are calculated at the same frequency (0.001 au) with MRDCI implementation of ZINDO and for an electric field (0.001 au). Our calculated values for the optical properties compare fairly well in trends with the experimental results that the linear (α) and nonlinear (γ) optical properties increase steadily with the increase in the conjugation-length of the chain (see Table 6.2). For example, for ethylene, γ_{expt}= 1504.9 au, for butadiene (n=2), γ_{expt}= 4566.4 au and for hexatriene (n=3), γ_{expt}= 14950.1 au [98]. Note that, our calculations are performed at a much higher frequency compared to the laser frequency used in the experiment. However, the magnitudes of all the polarization quantities are much larger for the charge-transfer complex, Al_4M_4 clusters, compared to the conventional π conjugated chains with comparable conjugation length. Only when there are very large number of spacers (n=5-6), that the magnitudes

Figure 6.3: Frontier orbitals for Al_4Li_4 (HOMO-4 to LUMO+4).

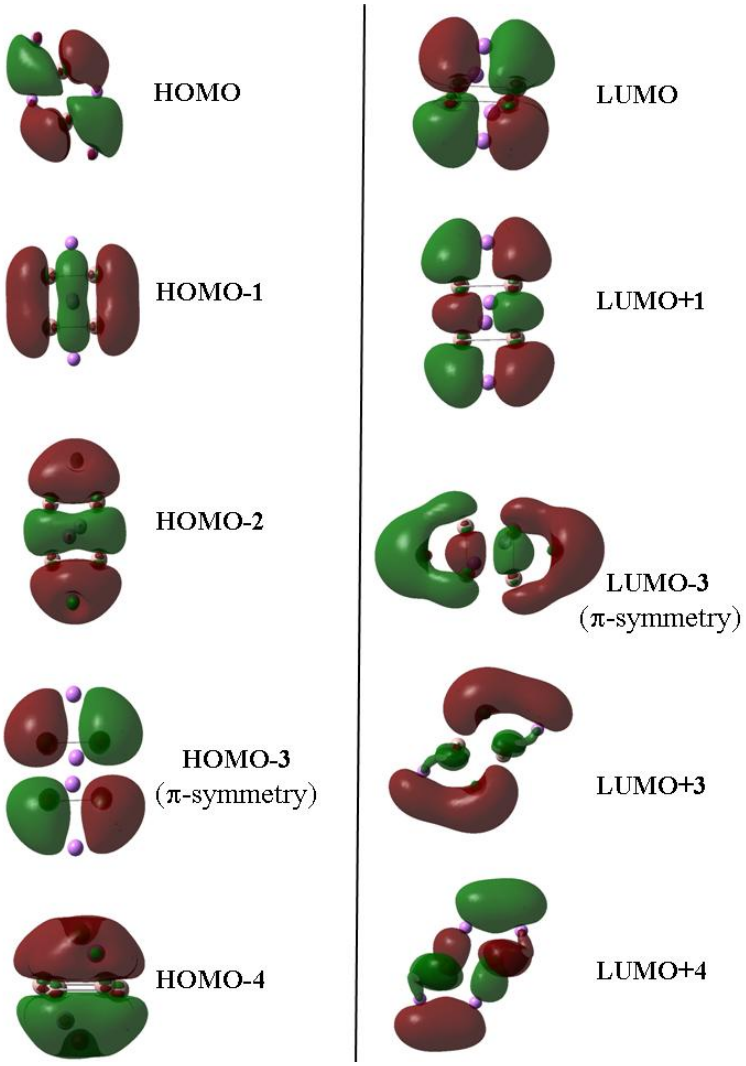

become comparable to the much smaller Al_4-clusters.

6.4 Conclusions

To conclude, our theoretical study shows that the small four membered Al_4-clusters functionalized with various metal cations provide an innovative route for selection of materials with very high nonlinear optical properties. Such large NLO coefficients for the metal-clusters arise particularly due to:

1. Charge transfer from the highly electro-positive metal atoms (Li and Na) to the Al_4 ring which become effectively 4π-electron systems.

2. Poor σ-π separation for Al_4M_4 introduces hybrid σ-levels within the π and π^* levels due to intermixing. This effectively reduces the optical gap for these systems.

Thus, these inorganic materials may compete for the next generation NLO materials. Device integration from these all-metal clusters will, however, require further stabilization in the solid-state. This issue of stabilization of all-metal clusters has been addressed in details in the eighth chapter wherein methodologies are proposed to stabilize such all-metal clusters through complexations with transition metals.

Chapter 7

A Model for σ-π separation: Critical examination of the role of σ and π electron delocalizations

7.1 Introduction

The polarization responses in π-conjugated organic molecules are mainly due to the delocalization of the π-electrons. However, for metallic clusters, both the σ and π electrons can be easily deformed due to external field. This is primarily because, in these clusters, the σ and π electronic energies are closely spaced. As discussed in the previous chapter, the very large third harmonic coefficients in the all-metal clusters like Al_4Li_4 arise specifically

due to such poor σ-π separation. Based on only the π-electron H*ü*ckel picture, it should be antiaromatic as it has 4π-electrons in its frontier orbitals. However, the core σ electrons also contribute to the frontier orbitals to a significant amount. Thus, we believe that it will be incorrect to neglect the contributions from the σ-electrons, while discussing the low-energy property of such systems.

There exist various direct and indirect methods in quantum chemistry literature for qualitatively predicting the nature of electronic delocalizations. For example, the NMR criteria based on the nucleus independent chemical shifts (NICS) [99], charge density analysis based on atoms in molecules (AIM) theory and electron localization functions (ELF) [100], aromatic fluctuation index (FLU) [101] and calculation of paratropic and diatropic ring currents [102], to name a few have been utilized to their fullest extent in describing the delocalization characteristics. However, a direct probe that measures the extent of both σ and π delocalizations together with their individual contributions is clearly missing.

In this chapter, a theoretical tool is provided for determining the dominant contributions of the σ and π electron delocalizations to the ground state geometry of these all-metal molecules. The delocalization tool is utilized to assign overall aromaticity/antiaromaticity together with σ/π aromaticity/antiaromaticity for these systems.

A set of metal clusters (Li_n) where only σ-electrons are present is also considered. The role of these electrons in stabilizing these clusters in terms of their binding energies are discussed. The variations in the binding energies

are traced back to exchange coupling between these σ-electrons [1].

7.2 σ-π electron separation scheme

A very accurate estimation of the nature of σ and π delocalizations can be obtained through a direct σ-π separation in terms of energies along the distortion coordinates of the molecular system. Theoretical advancements in such methods have been reviewed extensively in the literature [103–106]. The basic idea for all the methods is to distort the molecules both in the ground state (GS, singlet) geometry and in their highest spin state (HS) by freezing the π-electrons in a parallel orientation [107, 108]. The distortion in the HS state thus exclusively involves the σ-distortions. Similarly, if one distorts the ground state, ones derives the contributions from both the σ and π distortions. Subtraction of the distortion energies of the ground state and the highest spin state thus provides a reliable estimate of the π- distortion energies.

To demonstrate the superiority of such a method, a variety of metal clusters are considered: Al_4Li_4, $Al_4Li_4{}^{2-}$, Ga_4Li_4, $Al_4{}^{2-}$. These systems are compared with C_4H_4 and similar organic analogues at each step of σ-π analysis. These systems have either 4π, 6π or 2π electrons in their frontier orbitals and provide a diverse set for studying aromaticity or antiaromaticity. All the molecular geometries are optimized at the B3LYP/6-311G++ (d,p) level. The structures are shown in Fig. 7.1. As can be seen, the ground state geometry for both Al_4Li_4 and Ga_4Li_4 have planar rectangular geometry

[1]Papers based on the work reported in this chapter have appeared in (1). *J. Chem. Theory and Compt.* **1**, 824 (2005). (2). *Computing Letters* **1(4)**, 271 (2006).

for the ring with the Li ions occupying positions so as to maintain a C_{2h} architecture. The bond-length alteration (BLA) for Al_4Li_4 and Ga_4Li_4 are 0.12 and 0.14 $\mathring{A}$ respectively. Note that, the same for C_4H_4 is 0.24 $\mathring{A}$. The fact that the BLA for Ga_4Li_4 is more than that in Al_4Li_4 suggests that Ga_4Li_4 should be more antiaromatic than Al_4Li_4, in analogy with C_4H_4. A σ-π would thus be ideal for quantifying it.

The geometry optimized structures are distorted by ΔR (where ΔR is the difference between the long M-M and short M-M bond in the M_4 ring) so that that the distortion keeps the sum of two adjacent M-M bonds constant [Figure 7.2 (Scheme (a))]. The energy associated with the distortion is partitioned into σ and π components as $\Delta E_\pi = \Delta E_{GS} - \Delta E_\sigma$. The σ-backbone for a M_4 ring with 4π electrons can be modeled as $M_4{}^{4-}$ with a H.S configuration (S=2) with all the 4π electrons being parallel [Figure 7.2 (Scheme (b))]. Similarly, for the 2π electron systems like $C_4H_4{}^{2+}$ and $Al_4{}^{2-}$, S=1 corresponds to the H.S state. For the 6πe $Al_4Li_4{}^{2-}$, however, there are only four π-orbitals and thus a H.S configuration with S=3 is not feasible, rather two parallel spins with S=1 state in $Al_4Li_4{}^{2-}$ corresponds to the H.S state. ΔE_{HS} is thus defined as ΔE_π. For the H.S systems, UB3LYP calculations are performed at the same basis set level together with the annihilation of the first spin-contaminant.

7.3 Results for the all-metal clusters

In Fig. 7.3, the σ-energy and the π-energy as a function of the distortion parameter, ΔR, are plotted. In the inset, the core energy, V_{core} (sum of kinetic

Figure 7.1: Ground State optimized structure of (A). C_4H_4 (B). Al_4Li_4 (C). Ga_4Li_4 (D). Al_4^{2-} (E). $Al_4Li_4^{2-}$ from $Al_4Li_4Fe(CO)_3$ (F). $C_4H_4^{2+}$ (planar structure).

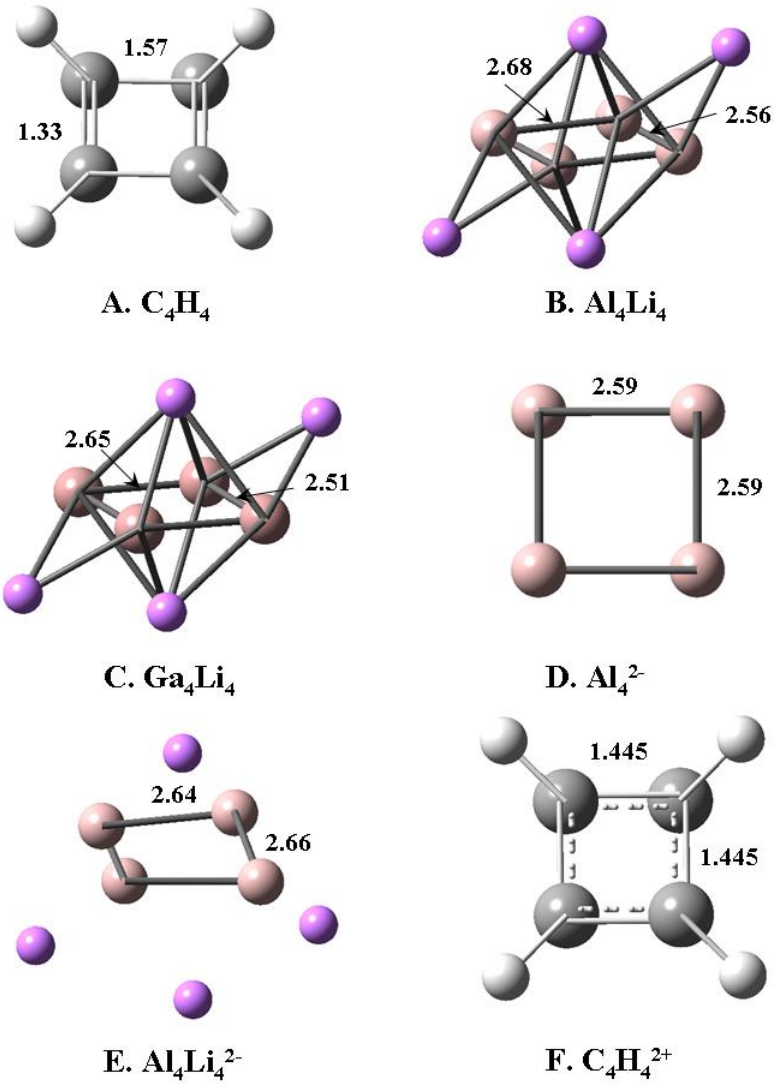

Figure 7.2: Scheme (a) The distortion mode for the M_4 rings (M=C, Al, Ga) in the ground state. Li atoms not shown for the sake of clarity. (b) The distortion in the σ-electrons involving the distortion in a high spin configuration.

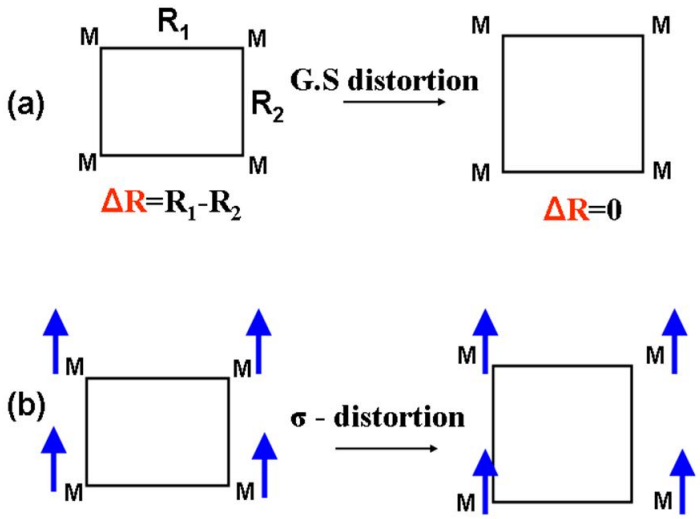

energy and nuclear-electron (ne) interactions), electron-electron interactions (V_{ee}) and the nuclear-nuclear interactions (V_{nn}) energies are plotted. For all the systems, it is found that the π-electrons have a general tendency of forming distorted structure (π-energy is most stable at large ΔR) while the σ-framework oppose the distortion and tends to equalize the bonds. The final structure and thus the aromatic/antiaromatic features will, however, crucially depend on the predomination of either of the forces. In Fig. 7.3(a), the result for the well-known C_4H_4 system is shown. In C_4H_4, the instability associated with the σ-backbone distortion is very little (4 kcal/mol for ΔR=0.1) while the stability for π- distortion is quite substantial (22 kcal/mol for ΔR=0.1), clearly overwhelming the tendency for σ-backbone equalization. Thus the C_4H_4 has a rectangular structure and is overall π-antiaromatic with a minor σ-aromatic component. Both V_{ee} and V_{nn} are destabilized with distortion while the V_{core} component is stabilized. Further analysis shows that it is the V_{ne} term in the V_{core} that favors the distorted structure. This is easy to understand as the V_{ne} component is associated with the electron-lattice interactions and leads to Jahn-Teller stabilization in the distorted structure. However, components like V_{ee} and V_{nn} stabilize the ΔR=0 structure associated with the delocalized π-electrons (for nonzero ΔR, the electron density is localized in shorter bonds).

For the all-metal system, however, the σ-π separation energy play a crucial role. For example, in Al_4Li_4, the distortion in the σ-framework leads to a destabilization of 2.5 kcal/mol while the π-framework gains energy of 3.5 kcal/mol (Fig. 7.3(b)). The ground state energy is thus stabilized by the distortion along the ring. Accordingly, Al_4Li_4 is assigned

Figure 7.3: Variation of the σ-energy (square) and the π- energy (circles), both in kcal/mol as a function of the distortion axis, ΔR for (a) C_4H_4 (b) Al_4Li_4 (c) Ga_4Li_4 and (d) $Al_4Li_4{}^{2-}$. The insets show V_{core} (green), V_{ee} (black) and V_{nn} (red) components in the ground state structures. All the energies are scaled to make the most stable geometry zero in energy and positive values in Energy-axis correspond to destabilization.

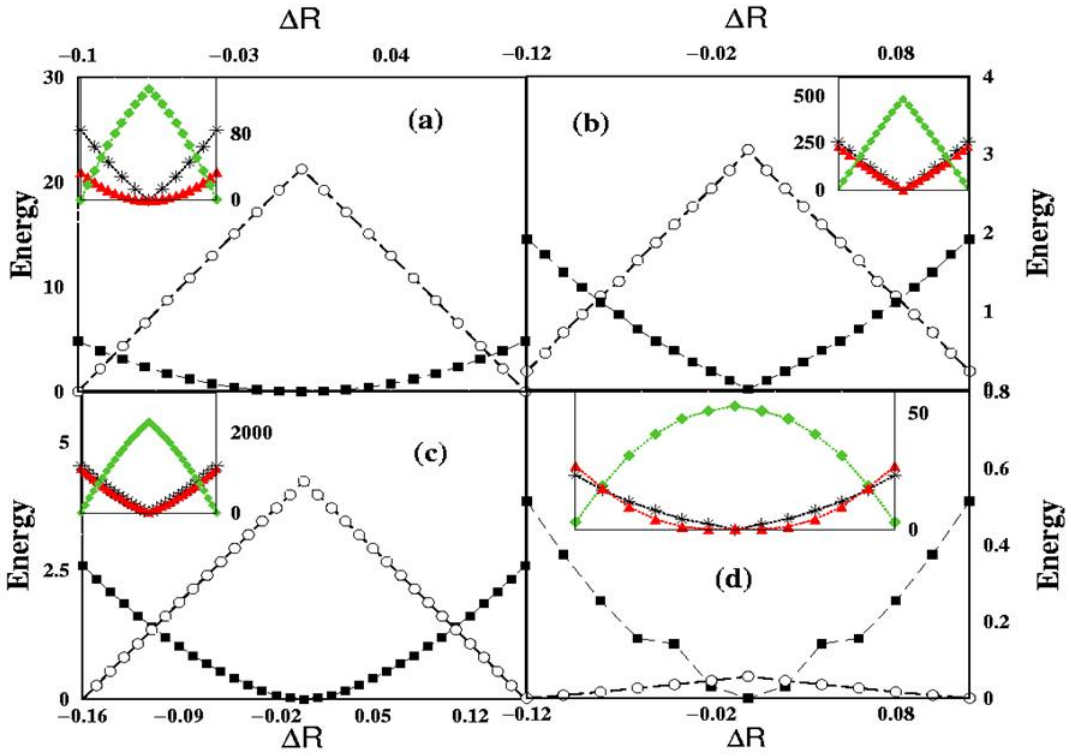

as π-antiaromatic although the σ-aromatic component is also substantial. However, as a whole, Al_4Li_4 is antiaromatic because the π-antiaromaticity exceeds the σ-aromaticity by 1 kcal/mol. The energy components also follow very similar trends like that for C_4H_4 (Fig. 7.3(b), inset). Similar conclusion is also derived for the Ga_4Li_4 where the π-stabilization associated with the distortion is 4 kcal/mol while σ-destabilization is 2.5 kcal/mol (seen in Fig. 7.3(c)). The distorted π-antiaromatic structure is thus stabilized by an amount of 1.5 kcal/mol, 0.5 kcal/mol more than that for Al_4Li_4. Thus the π-antiaromaticity follows the order: $C_4H_4 > Ga_4Li_4 > Al_4Li_4$.

The fact that this simple σ-π separation gives a very clear picture for the nature of aromaticity/antiaromaticity is evident from Fig. 7.3 (d). For, the 6π-electron system, $Al_4Li_4^{2-}$, a similar σ-π separation analysis is performed. Contrary to the previous cases, in $Al_4Li_4^{2-}$, the stabilization associated with the equalization of the σ-backbone overwhelms the instability due to π-electron localization by 0.5 kcal/mol and forces the system to be aromatic. This is of course true for C_6H_6 where σ-delocalization exceeds the π-localization by 6 kcal/mol. In Fig. 7.4(a), the energy profile is plotted for $C_4H_4^{2+}$ which shows an overwhelming π-delocalization compared to the smaller σ-localization. Similarly, for the all-metal system, Al_4^{2-}, the ground state corresponds to a square geometry with Al-Al bond length, 2.54 $\mathring{A}$. This is readily understood from the plot as the π-destabilization associated with the distortion exceeds the stability in the σ- backbone due to distortion (Fig. 7.4(b)) although again, the energy scales for the σ and π distortion are comparable. Also, as a general rule, it is found that the V_{ne} term favors distortion.

Figure 7.4: Same variation (including the inset) as in Fig. 7.3 for (a) $C_4H_4{}^{2+}$ and (b) $Al_4{}^{2-}$.

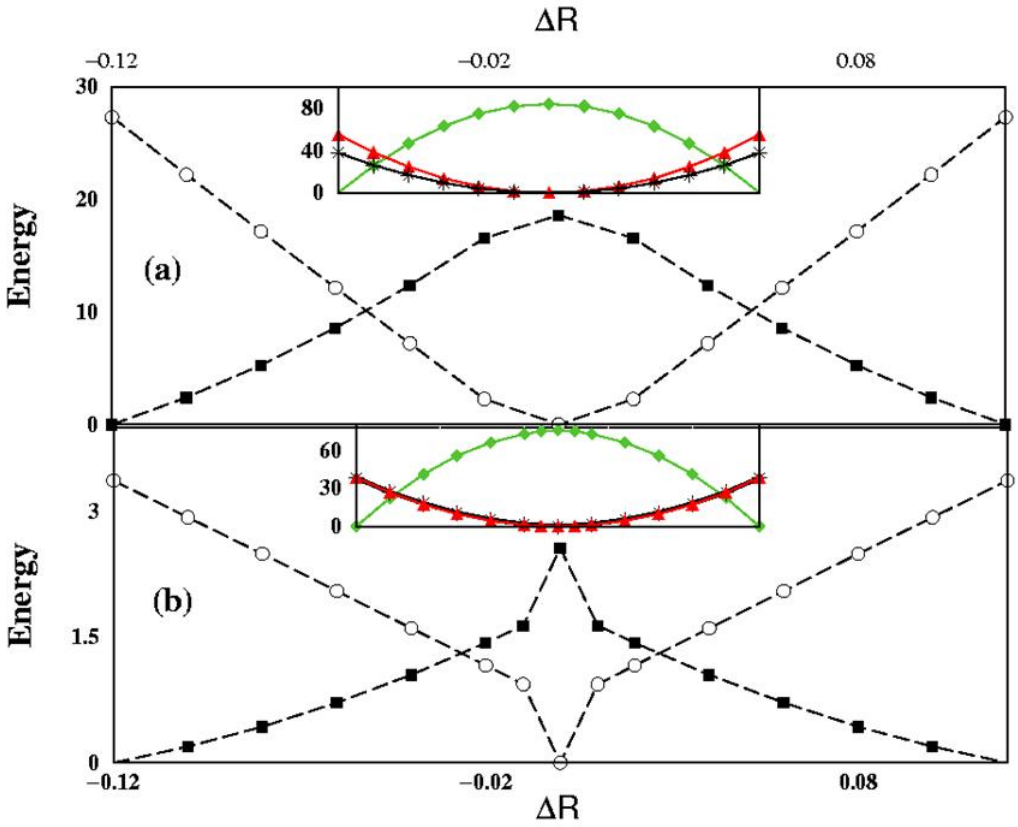

7.4 Case study for the alkali-metal clusters: $(Li)_n$

Clusters composed of atoms like the Li-atom involve bonding interactions through the σ-bonds only. However, all the single electrons in the Li-atoms ([He]$2s^1$) can be bonded only if there are even number of atoms in the clusters. For clusters composed with an odd-number of Li-atoms, one electron always remains unpaired. Also, for such clusters the geometry of the cluster may induce frustrations. Thus, one expects that the odd-membered clusters will behave very differently from their even-membered congeners. However, such effects can be observed only for small clusters where the interaction length scales differ from their bulk behavior.

The ground state geometries for $(Li)_n$, n=1-8, are fully optimized using the hybrid Becke 3 Lee-Yang-Parr (B3LYP) gradient corrected approximate density functional theory at the 6-31G+(d) basis set level. The basis set is further increased to 6-311G+(d,p) level to ensure the basis set convergence. Corresponding to each minimum energy structure, it is found that there are several geometrical isomers very close in energy. Several initial guess structures with different symmetries are thus investigated. Additional frequency calculations are performed on these clusters to confirm the ground state geometry and removal of vibrational instabilities. The ground state geometry optimized structures in $(Li)_n$ are shown in Fig. 7.5.

With the increase in the size of the clusters, these structures become progressively distorted and non-planar. The rhombus geometry in $(Li)_4$, corresponds to the largest planar structure. Further increase in the cluster size

Figure 7.5: The ground state structures of Li_n, n=1-8 clusters.

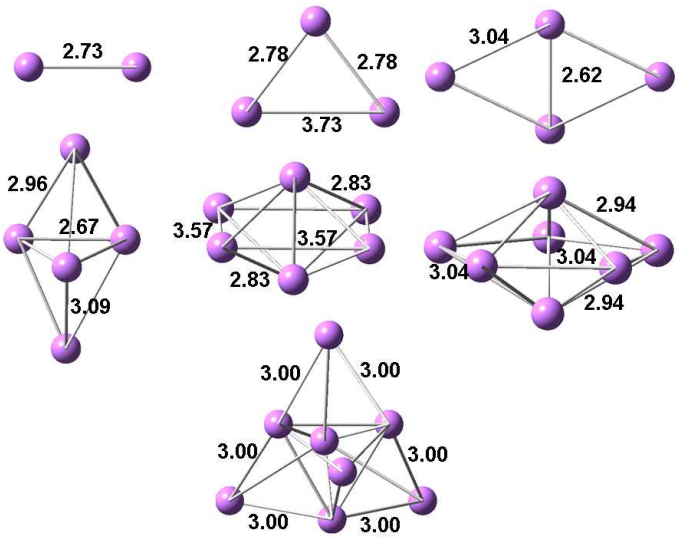

leads to formation of closed structures with $(Li)_6$ and $(Li)_7$ being octahedral and pentagonal bi-pyramidal respectively. $(Li)_8$ on the otherhand, maintains a pyramidal structure. The structure of the $(Li)_6$ cluster is of particular interest. The planar D_{6h}, benzene like structure exists as a local minimal structure and its binding energy is 73.7 kcal/mol compared to the octahedral ground state structure that has a binding energy of 102 kcal/mol.

The ground state for all the systems with n=odd (n=1,3,5 and 7) is an S=1/2 state while for n=even, the stable geometry is associated with S=0 suggesting pairing of the single unpaired electron in each Li atom for the even numbered clusters. However, for the odd clusters, such a spin pairing is geometrically forbidden and the ground state structures have frustrated spin-degeneracy since the unpaired spin can be in any Li or delocalized over the entire cluster.

To account for such a spin degenaracy, we consider the binding energy and later a spin Hamiltonian. The binding energies are defined for the odd-membered clusters as: $(B.E)_{odd}$=[nE(M_1)-E(M_n)] and the binding energies for the even-membered clusters as: $(B.E)_{even}$=[(n/2)E(M_2)-E(M_n)]. In Fig. 7.6, the binding energies for the Li_n clusters are shown (solid line, circles). One clearly observes a remarkable odd-even phenomenon in the binding energies with the odd-membered clusters being more stable than their even-membered congeners.

For a proper understanding of such an odd-even oscillation in the binding energies for these clusters, the highest spin configurations in these systems are also considered. For such a configuration the H.S geometry does not have any component of σ-delocalization and the stability of such clusters

Figure 7.6: Variation in the binding energies for Li clusters in low-spin (ground state) configuration (solid line, circles) and the same in high spin configuration (dotted lines, squares). The binding energies for odd-membered clusters are defined as $\Delta E_n(\text{odd})=nE_1-E_n$ and for the even-membered rings as $\Delta E_n(\text{even})=(n/2)E_2-E_n$ with the increase in the cluster size.

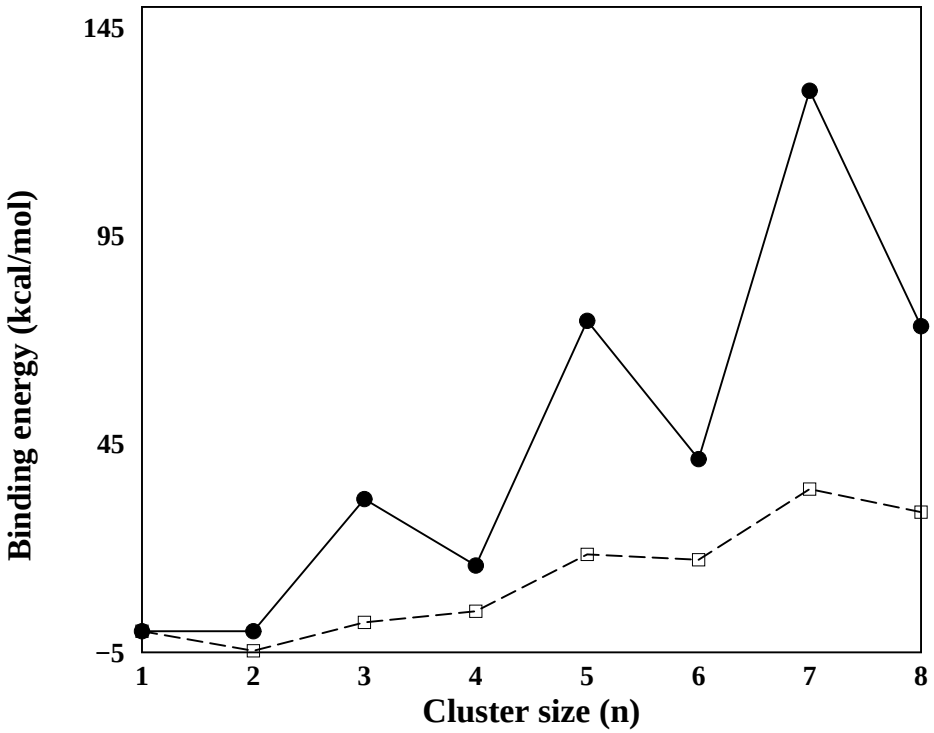

involve only the core electrons, as the σ-electrons are already frozen in a H.S configuration. Therefore, the interactions in these clusters can be formally called as ferromagnetic bonding. [109, 110].

Also in Fig. 7.6, the binding energies for these H.S structures are plotted (dotted line, squares). This is calculated using the simplistic dissociation scheme discussed above ($\Delta E_n = nE_1 - E_n$) with the energy of Li_n now corresponding to all parallel spin configuration. Note that the H.S configuration corresponds to the same geometries and only the spin state is changed. The binding energies for these H.S clusters also show a similar odd-even effect with larger binding energy slope for the odd membered rings compared to that for the even membered rings. This is quite understandable since for the odd membered systems, the ground state has a doublet spin configuration (S=1/2) with finite magnetization. Thus, the ferromagnetic state involves less destabilization as compared to that for the even membered systems where the ground state is anti-ferromagnetic. One can also notice that for the small dimer, Li_2, with H.S configuration (S=3/2), the structure is unstable by 4.6 kcal/mol, however, with the increase in the cluster size, the ferromagnetic structures become progressively stabilized and for the H.S Li_8 configuration (S=4), the stabilization energy is 28.6 kcal/mol. Although in comparison to the L.S structures, the binding energies in these ferromagnetic structures are smaller, the moderate binding energies for these ferromagnetic systems suggest that under suitable stabilizing conditions, these H.S clusters can possibly be realized.

These clusters are stabilized through both σ and core electron delocalizations. The σ-electron contributions to the stability of the structures is

analyzed by performing a σ-core separation analysis. The σ electronic energies are calculated as, E_σ=E_{GS}- E_{core}, where E_{GS} corresponds to the ground state energies for these structures. E_{core} actually corresponds to the E_{HS} energies as each Li atom has 1 valence electron and a HS configuration for these electrons suggests that these electrons are in all-parallel orientations and so are not involved in delocalization. In Fig. 7.7, the σ-electron energies are plotted as the cluster size increases. One again observes a clear odd-even phenomenon with the energies being larger for the even-membered structures compared to the odd-ones.

The advantage of separating out the σ-contribution from [He] backbone is that one can then consider simple spin- spin interaction models to critically analyze the odd-even effects in these clusters. The well-known Heisenberg model [111] with localized σ-electronic spin is used to calculate the interaction between the paramagnetic Li-centers. The interactions for an N site system can be written as:

$$H_{spin-spin} = J \sum_{ij} S_i S_j \tag{7.1}$$

where the sum runs over all pairs. Since, the ground state geometry for these systems are LS configuration, anti-ferromagnetic interaction between the electronic spins (positive J) is considered. Note that, for the odd-clusters, S_{total}=1/2 while for the even-clusters, S_{total}=0. Thus, the interaction energy for a N site system can be written as:

$$E_{spin-spin} = (J/2)[S_{total}(S_{total}+1) - NS_1(S_1+1)] \tag{7.2}$$

Figure 7.7: Variation in the σ-energies (solid line, circles) as a function of increase in the cluster size (n). The inset shows the variation of the exchange energy (in J units) with n.

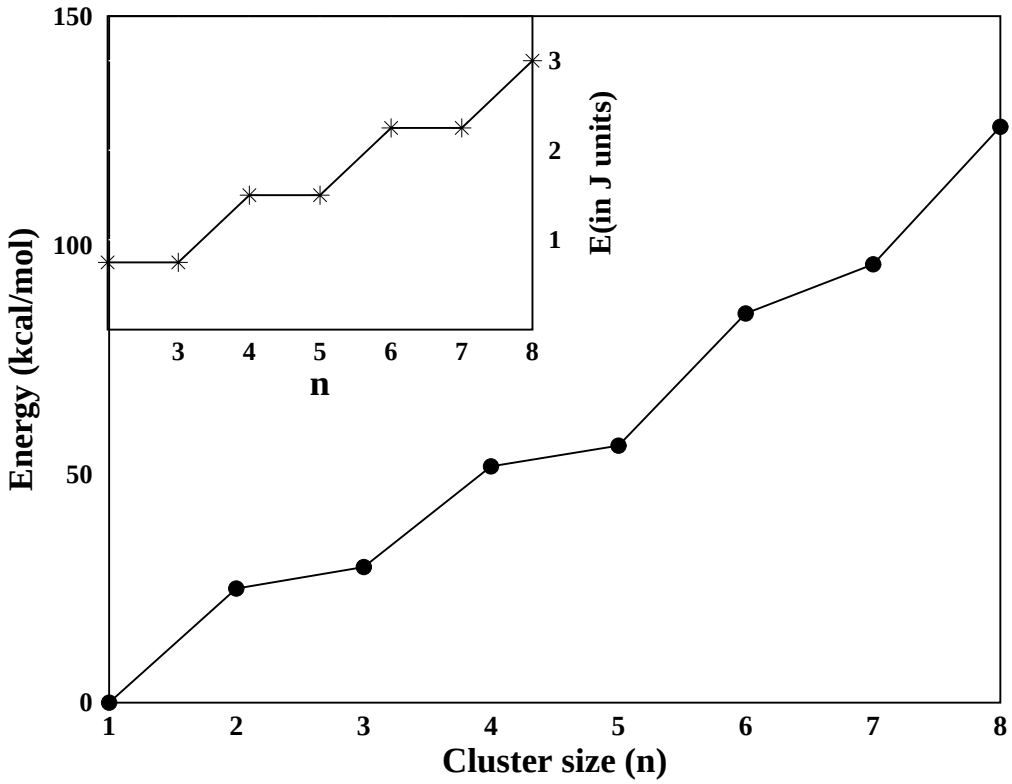

where S_1=1/2 (spin of a single Li atom). One can further simplify the above equation as:

$$E_{spin-spin} = (J/2)[S_{total}(S_{total}+1) - 3N/4)] \tag{7.3}$$

It is assumed that that these are isotropic and the interaction between each pair is same. Thus the exchange integral, J is kept constant. Although this is a drastic approximation, it certainly provides an insight for the phenomenon. In Fig. 7.7 (inset), the exchange energy is plotted with the increase in the cluster size. The odd-even oscillation is evident though the magnitude of exchange for the n^{th} and $(n-1)^{th}$ (where n is odd) are same.

7.5 Conclusions

In this chapter, a simple scheme is provided to separate out the σ and π electron contributions for all-metal clusters and core and σ electron contributions in case of alkali metal.

It is shown that all-metal molecular clusters like Al_4Li_4 and Ga_4Li_4 are predominately π-antiaromatic although there is a significant contribution from σ-aromaticity as well, due to the close proximity in σ/π energy levels in these metal clusters compared to the analogous organic systems.

It is also shown that for systems like the Li_n clusters, which possess only σ-electrons, there is a clear manifestation of odd-even oscillations in the binding energies. Such oscillations specifically arise due to frustrated and spin-paired configurations in the odd and even membered clusters respectively.

Chapter 8

Strategies to stabilize all-metal antiaromatic molecules: Complexation with 3d-transition metals

8.1 Introduction

From the discussion in the sixth chapter, it is clear that all-metal charge-transfer clusters are excellent materials for large third harmonic generation. Such large NLO effects arise specifically due to the smaller optical gap as the frontier orbitals have admixtures of π and σ electrons. In the previous chapter, a method has been developed through which the extent of the delocalizations in the π and σ levels can be explicitly and separately assigned. Based on this method, Al_4M_4 (M=Li, Na and K) are assigned as antiaromatic

species.

However, since Al_4M_4 (M=Li, Na and K) are antiaromatic, it should be difficult to isolate and synthesize. Cyclobutadiene, (C_4H_4), a 4π electron system remained non-isolated for a longtime before H. C. Longuet-Higgins and Orgel proposed in a landmark paper, the concept of stabilization of antiaromatic molecules through complexation with a transition metal to form an organometallic compound [112]. The compound was synthesized soon after [113]. In the following, we show that such a simplistic model is justified even for the small Al_4-clusters. We also propose a few other stable complexes for these all-metal species. Additionally, these compounds are compared and contrasted with their organic analogues (corresponding C_4H_4 complexes)[1].

8.2 Optimized structures for the ligands

The closed shell calculations are performed for the singlet states whereas open shell calculations are performed for the triplet state at the 6-311G(d,p) basis set level. Electron correlation has been included according to the DFT method using Becke's three parameter hybrid formalism and the Lee-Yang-Parr functionals (B3LYP) available in the Gaussian electronic structure set of codes [114].

Simple H*ü*ckel π-electron theory predicts a square geometry (triplet spin state) for C_4H_4 with equal C-C bond lengths [115]. However, inclusion of interaction with the underlying σ backbone stabilizes the C_4H_4 molecule in a singlet state with rectangular geometry. This is in-fact a classic example

[1]Papers based on the work reported in this chapter have appeared in (1). *J. Am. Chem. Soc.* **127**, 3496 (2005). (2). *Chemical Communications*, 5032 (2005).

of Jahn-Teller distortion in low-dimensional systems which allows stabilizations through bond length alternation (C_4H_4 has a BLA of 0.24 $\mathring{A}$). Within this picture, the square geometry actually corresponds to a transition state between two degenerate rectangular ground state structures. The rectangular C_4H_4 is more stable than the square geometry by 6.2 kcal/mol. Thus, a triplet square geometry is expected to be the transition state for processes such as ring whizzing, where one rectangular form is converted into the other (an in-plane rotation of 90^0), in harmony with time-resolved transition state studies for the tub-inversion in 1,3,5,7-cyclooctatetraene [116].

Since in Al_4M_4, the σ-π separation is poor, the H*ü*ckel π-electron picture becomes highly error-prone. The π electrons in this case interacts more strongly with the σ backbone because of their close proximity in energies and a distorted structure is expected as the ground state for the Al_4 rings. There are some remarkable similarities in the structures of Al_4M_4 with variation in the alkali metal ions. The ground state minimum energy form for all the molecules possess a C_{2h} symmetry and have a substantial bond length alteration (BLA) [0.124 $\mathring{A}$ for Al_4Li_4, 0.11 $\mathring{A}$ for Al_4Na_4 and 0.10 $\mathring{A}$ for Al_4K_4].

Similar to C_4H_4, the structural distortion in Al_4M_4 leading to a magnetic triplet state with D_{4h} symmetry is found to lie $\sim$ 60 kcal/mole above the ground state singlet. There also exist a low-energy triplet structure with the same geometry as the ground state (C_{2h} symmetry) at an energy only 5 kcal/mole above the ground state. This triplet geometry for Al_4M_4, however does not have a counterpart in C_4H_4. This clearly demonstrates that due to poor σ-π separation in Al_4M_4, there exist low-energy metallic states to accommodate the parallel arrangement of the electronic spins.

Existence of a very stable rectangular ground state structure together with a high energy square geometry as the transition state for the Al_4-ring similar to those for C_4H_4 suggests that the Al_4Li_4 cluster is a 4π electron system with the π-HOMO (highest occupied molecular orbital) being a non-bonding molecular orbital like C_4H_4. In the context of C_4H_4, H. C. Longuet-Higgins suggested that such a system can be stabilized if the non-bonding electrons form bonding molecular orbitals with suitable low energy d-orbitals of a transition metal. For this to happen, however, the energies of the d-orbitals should lie close to the low-energy levels of the molecule alone.

8.3 $Fe(CO)_3$ complex

A molecular complex, $\eta^4(C_4H_4)$-$Fe(CO)_3$, has been recognized through the formation of such bonding molecular orbitals and this complex has been reported to be quite stable [117]. In fact, oxidation of this complex releases the C_4H_4 ligand which is a stable source for the highly reactive cyclobutadiene molecule in organic synthesis [118]. For the Al_4M_4 systems, we have performed the ground state energy analysis on the similar systems, $\eta^4(Al_4M_4)$-$Fe(CO)_3$, using the same level of theory mentioned above. Both $\eta^4(Al_4M_4)$-$Fe(CO)_3$ and their organic analogue are found to have substantial stability (see Fig. 8.1 for structures). Al_4M_4 indeed form stable η^4 complexes with $Fe(CO)_3$. The stability of the complexes are investigated using the following fragmentation scheme:

$$\eta^4(C_4H_4)\text{-}Fe(CO)_3 = C_4H_4 + Fe(CO)_3$$

$$\eta^4(Al_4M_4)\text{-}Fe(CO)_3 = Al_4M_4 + Fe(CO)_3$$

The binding energies [defined as $E_{complex}$-$E_{fragments}$] in (Al_4Li_4)-$Fe(CO)_3$, (Al_4Na_4)-$Fe(CO)_3$ and (Al_4K_4)- $Fe(CO)_3$ are -118.85 kcal/mol, -122.92 kcal/mol and -126.28 kcal/mol, respectively. For comparison, the binding energies in (C_4H_4)-$Fe(CO)_3$ is also calculated, which is -78.44 kcal/mol. The comparable binding energies for the all-metal sandwich complexes and the organometallic complexes suggest that Al_4M_4 are very well stabilized in the complex, in-fact, even more stabilized than C_4H_4. Note that, compared to the ground state structures for the Al_4M_4, where the M ions are in interaction with the Al_4 ring, the structure for Al_4M_4 in the complex gets deformed losing all interactions with the alkali ions. This amounts to a destabilization of $\sim$ 25-30 kcal/mol (calculated as the energy difference between the ground state structure of Al_4M_4 and the single point energy for the same in the $\eta^4(Al_4M_4)$-$Fe(CO)_3$ complex). However, the interaction of the Al_4 ring with the $Fe(CO)_3$ overwhelms the loss of interaction of Al_4 ring with the alkali-ions, stabilizing the overall structure of the complex. The magnitudes for the HOMO-LUMO gaps for the(Al_4Li_4)-$Fe(CO)_3$, (Al_4Na_4)-$Fe(CO)_3$ and (Al_4K_4)-$Fe(CO)_3$ complexes decrease in the order: 3.34 eV, 2.31 eV and 1.85 eV respectively, suggesting the softer nature of the Al_4K_4 ligand.

The BLA (Δr) for both C_4H_4 and Al_4M_4 in the free geometry and when they are complexed with the transition metal have been computed. For C_4H_4, the Δr is 0.24 $\mathring{A}$ in the free state. In the complex, $\eta^4(C_4H_4)$-$Fe(CO)_3$, the Δr for the C_4H_4 ring is only 0.005 $\mathring{A}$. Thus, C_4H_4 when complexed, is a square rather than a rectangle and as expected from the π-only interaction, it behaves as aromatic $C_4H_4{}^{2-}$.

Figure 8.1: Equilibrium minimum energy geometries for (i) $\eta^4(C_4H_4)$ - $Fe(CO)_3$ and (ii) $\eta^4(Al_4Li_4)$-$Fe(CO)_3$. Bond lengths are in $\mathring{A}$. Ball color: Red=O, Violet=Fe, Black=C, Pink=Li, White=H and Light brown=Al.

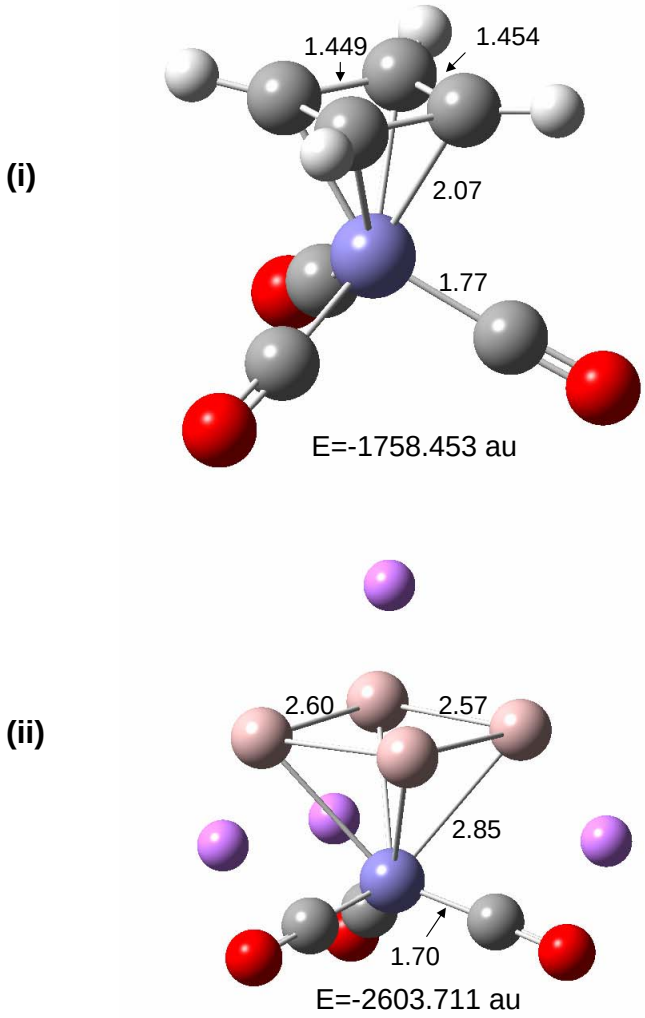

In the complexes, (Al_4M_4)-$Fe(CO)_3$, the BLA are very small [0.028 $\AA$, 0.0345 $\AA$ and 0.041 $\AA$ in $(Al_4Li_4)Fe(CO)_3$, $(Al_4Na_4)Fe(CO)_3$ and $(Al_4K_4)Fe(CO)_3$ respectively]. Such a large decrease in Δr clearly supports that the Al_4M_4 ligands have been converted into a 6π $Al_4M_4{}^{2-}$, accounting for their substantial stability due to aromaticity. The complexation induced metalloaromaticity in Al_4M_4 is schematically shown in Fig. 8.2. While a square (triplet) Al_4M_4 is much higher in energy than the rectangular (singlet) Al_4M_4, this square form with a singlet configuration is stabilized on complexation to a transition metal. Same is the case for C_4H_4, where the square form becomes stabilized upon complexation. This is similar to the origin of aromaticity in benzene, where the π-delocalized D_{6h} structure corresponds to a energy minima between two bond-altered Kekule forms with D_{3h} symmetry.

An even more clear picture is derived by performing a calculation for the nucleus-independent chemical shift (NICS) at the GIAO-B3LYP /6-311+G(d,p) level. The NICS is calculated at the center of the Al_4 ring before and after complexation with the $Fe(CO)_3$. For comparison, the same values are also calculated for C_4H_4. In C_4H_4, NICS values before (isolated C_4H_4) and after complexation ($C_4H_4{}^{2-}$) are 23.55 ppm and -15.37 ppm, respectively. The change in sign clearly shows the transition from antiaromatic to aromatic nature upon complexation. In the Al_4M_4 ligands, the NICS values are -11.55 ppm, -7.91 ppm and -7.72 ppm for Al_4Li_4, Al_4Na_4 and Al_4K_4 respectively. However, on complexation with $Fe(CO)_3$, the NICS changes to -25.44 ppm, -26.41 ppm and -26.12 ppm for Al_4Li_4, Al_4Na_4 and Al_4K_4 respectively. Although the NICS calculations tend to suggest that free Al_4Li_4 should be aromatic, based on σ-π separation analysis as reported in chapter

Figure 8.2: Schematic representation of (i) change in geometry for ring whizzing and complexation to transition metal center for A=Al in Al_4Li_4 (ΔE_1=55 kcal/mol, ΔE_2=100 kcal/mol); A=C in C_4H_4 (ΔE_1=6.2 kcal/mol, ΔE_2=78.4 kcal/mol). Similar mechanism is also valid for Al_4Na_4 and Al_4K_4. (ii) Ring whizzing in benzene.

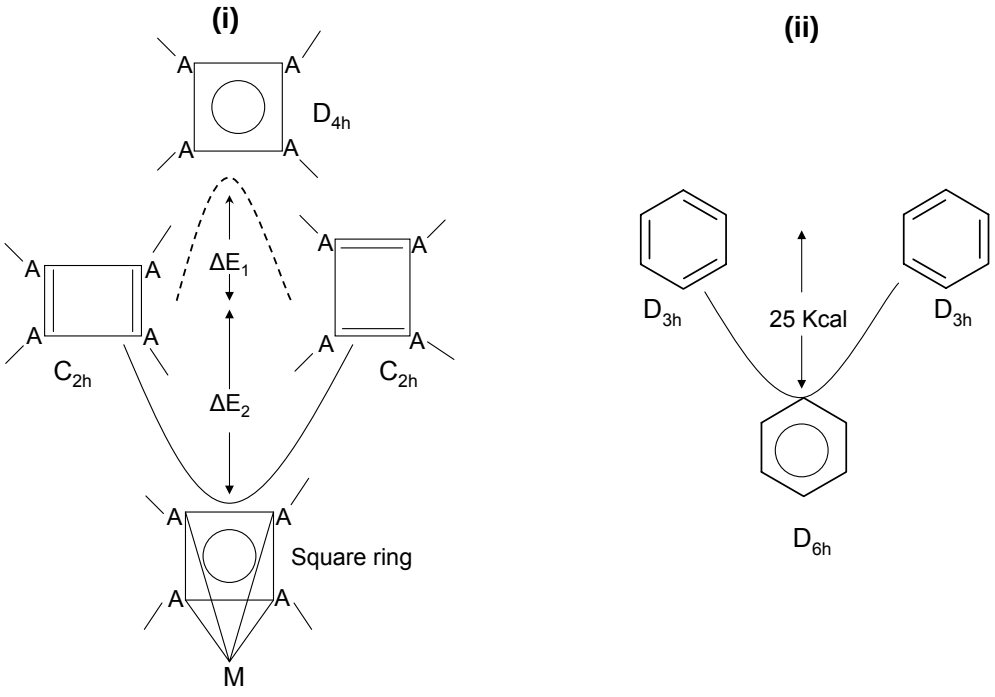

7, it is concluded that the Al_4M_4 molecules should be antiaromatic. However, the increase in NICS values with same negative sign suggests that aromaticity is induced within these clusters upon complexation, which is also expected from the π only picture of the conversion of Al_4M_4 to $Al_4M_4{}^{2-}$. Thus, complexation with $Fe(CO)_3$ induces metalloaromaticity in Al_4M_4 and thereby stabilizes the complexes, $\eta^4(Al_4M_4)$-$Fe(CO)_3$.

8.4 Metal sandwich complex

Another well known methodology in stabilizing a molecule is to form a sandwich geometry where the two molecular species can share interaction with a transition metal: cyclopentadiene is stabilized in such a geometry resulting in the ferrocene structure [119]. For C_4H_4, a simple effective electron number (EAN) counting shows that the metal in between the two ligands should have 10 valence electrons in stabilizing a sandwich of the type:$(C_4H_4)_2M$. The simplest metal with 10 electrons in the valence shell is Nickel(0). Elements in the same group like Pd or Pt have a strong spin-orbit coupling and prefer square-planar geometry (16 electron geometry). Thus a coordination number of 8 as required in a sandwich complex is not possible with Pd or Pt. After performing the geometry optimization at the same level of theory discussed above, it is found that the structure for $(C_4H_4)_2Ni$ is indeed a sandwich geometry with the two C_4H_4 rings above and below the Ni atom (see Fig. 8.3 (i)). In this complex, the Ni atom sits symmetrically inside the cavity of the two C_4H_4 rings with a distance of $1.99\mathring{A}$ from each C_4H_4 ring. The two C_4H_4 are however, staggered to each other.

Similarly, we have stabilized the Al_4M_4 clusters by introducing them in a sandwiches of the types: $(Al_4M_4)_2Ni$. The geometry for the $(Al_4Li_4)_2Ni$ is shown in Fig. 8.3 (ii) (the optimization and energy calculation at B3LYP/6-311G(d,p) level). The central Ni atom sits asymmetrically in the cavity of the two Al_4Li_4 rings. A very recent theoretical study by Mercero et al. on its aromatic analogue, $Al_4{}^{2-}$, support our claim [120]. Interestingly, the Al atoms in the rings bend towards the Ni atom and the planarity of the Al_4 ring is thereby lost. This is understood from the fact that when the 4π electrons of each of the two Al_4M_4 rings interact with the central Ni atom, the requirement of the Al atoms to be in interaction with the Li atom is no longer important. Instead, the sandwich like structure with 18 electrons provides an stabilization keeping the whole system electrically neutral. The stability of these complexes are investigated using the following fragmentation scheme:

$$(C_4H_4)_2Ni = 2\ C_4H_4 + Ni(0)$$

$$(Al_4M_4)_2Ni = 2\ Al_4M_4 + Ni(0)$$

where Ni(0) is in a ^{3}F state. The binding energies for $(Al_4Li_4)_2Ni$, $(Al_4Na_4)_2Ni$ and $(Al_4K_4)_2Ni$ are -146.054 kcal/mol, -147.12 kcal/mol and -103.12 kcal/mol respectively. For C_4H_4, this binding energy is -150.819 kcal/mol. Note that, very similar to that for the $\eta^4(Al_4M_4)$-$Fe(CO)_3$ discussed above, metalloaromaticity is introduced for these sandwich complexes too. The HOMO-LUMO gaps are 1.623 eV, 1.323 eV and 0.954 eV for $(Al_4Li_4)_2Ni$, $(Al_4Na_4)_2Ni$ and $(Al_4K_4)_2Ni$ respectively.

Figure 8.3: Equilibrium minimum energy geometries for (i) $(C_4H_4)_2Ni$ and (ii) $(Al_4Li_4)_2Ni$. Distances are in $\mathring{A}$.

(i)

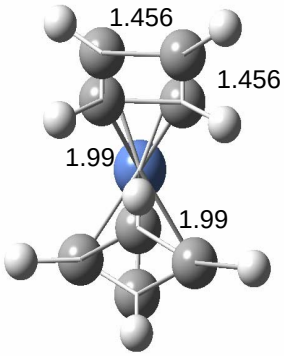

E=-1817.878 au

(ii)

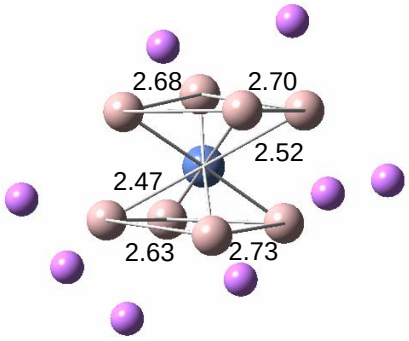

E= -3508.301 au

8.5 All-metal sandwich complexes: Substitution of C_4H_4 by Al_4M_4

In the previous section, the role of metal complexations in stabilization of all-metal antiaromatic molecules is discussed. In this section, the substitution methodologies to produce these all-metal half-sandwich and full-sandwich complexes from their conventional organometallic counterparts are highlighted. Also, a critical analysis is performed on the hybrid organic-inorganic sandwich complexes.

In Fig. 8.4, we show the substitution reactions in $(C_4H_4)Fe(CO)_3$ by Al_4M_4 to produce $(Al_4M_4)Fe(CO)_3$. The enthalpies for the reactions are highly exotherimic with ΔH=-48.8 kcal/mol, -53 kcal/mol and -56.3 kcal/mol for M=Li, Na and K respectively.

For the full-sandwich complexes, $(Al_4M_4)_2Ni$, the lowest binding energy is for $(Al_4K_4)_2Ni$. This arises from the distortion in the sandwich architecture due to the presence of the bulky K^+ ions (see structure in Fig. 8.5) as a result of which the average K^+ ion distance to the $Al_4{}^{4-}$ ring is very large (3.5 $\mathring{A}$). For $(Al_4Li_4)_2Ni$ and $(Al_4Na_4)_2Ni$, the average M^+ distance from the $Al_4{}^{4-}$ ring is 3.0 $\mathring{A}$. The binding energy for $(C_4H_4)_2Ni$ (as mentioned in the previous section) is -150.819 kcal/mol and thus unlike the cases for (Al_4M_4)-$Fe(CO)_3$, direct substitution of C_4H_4 with Al_4M_4 will be highly endothermic for the full-sandwich complexes and thus quite unfavorable. For a detailed understanding of the highly exothermic formation of (Al_4M_4)-$Fe(CO)_3$ compared to the endothermic substitution product $(Al_4M_4)_2Ni$, the HOMO orbitals for both the systems have been analyzed. The HOMO for (Al_4M_4)-$Fe(CO)_3$

Figure 8.4: Substitution reactions in $(C_4H_4)Fe(CO)_3$ by Al_4Li_4, Al_4Na_4 and Al_4K_4 to produce $(Al_4Li_4)Fe(CO)_3$, $(Al_4Na_4)Fe(CO)_3$ and $(Al_4K_4)Fe(CO)_3$ respectively. Note that all these substitutions are highly exothermic.

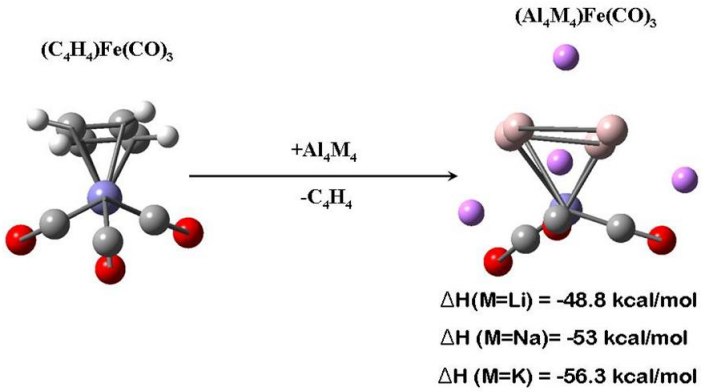

shows substantially more intermixing between the d-orbitals of the $Fe(CO)_3$ fragment and the π-orbitals of Al_4M_4, leading to stronger complexation in the case of (Al_4M_4)-$Fe(CO)_3$. The presence of three strong π-acceptor CO ligands in the $Fe(CO)_3$ fragment leads to quenching of d-orbitals on the Fe-atom and thereby facilitates stronger binding between the Al_4M_4 ligand and the $Fe(CO)_3$ fragment.

We consider here a substitution reaction of the type: $(C_4H_4)_2Ni + Al_4M_4 = (C_4H_4)Ni(Al_4M_4) + C_4H_4$. As has already been mentioned in the previous section, the Al_4M_4 (M=Li, Na and K) binds quite strongly to the metal center. Therefore, one expects that it is possible to synthesize a hybrid organic-inorganic sandwich complex. These hybrid complexes are very interesting, because, while for the C_4H_4 ligand, the interaction with

Figure 8.5: Stepwise synthesis for all-metal sandwich complexes from organometallic precursor $(C_4H_4)_2Ni$. The energy for $(C_4H_4)_2Ni$ has been scaled to zero to show the endothermic substitution reactions.

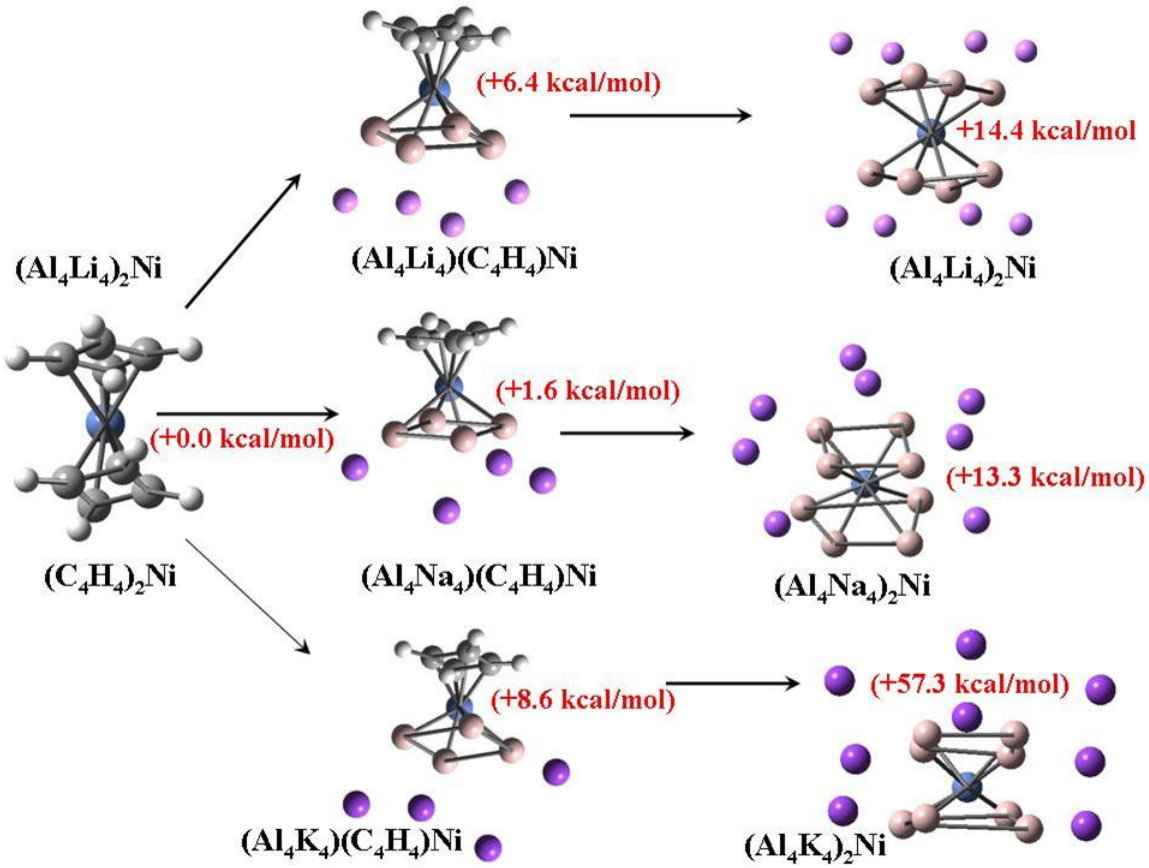

the transition metal atom involves only the π electrons, for the Al_4M_4 ligand, the interaction are through both the σ and π orbitals. Interestingly, the extent of the involvement of the σ and π orbitals in the interaction also depend on the nature of the counter ions present. The structures of these hybrid complexes are found to be quite stable. The heat of formation for $(C_4H_4)Ni(Al_4Li_4)$, $(C_4H_4)Ni(Al_4Na_4)$ and $(C_4H_4)Ni(Al_4K_4)$ are -153.93 kcal/mol, -158.82 kcal/mol and -151.80 respectively. The HOMO-LUMO gaps in the hybrid complexes are: 2.01 eV $[(C_4H_4)Ni(Al_4Li_4)]$, 1.96 eV $[(C_4H_4)Ni(Al_4Na_4)]$ and 1.35 eV $[(C_4H_4)Ni(Al_4K_4)]$. The BLA for C_4H_4 and Al_4M_4 are $0.0092\mathring{A}$ and $0.0386\mathring{A}$ in $(C_4H_4)Ni(Al_4Li_4)$, $0.0106\mathring{A}$ and $0.0168\mathring{A}$ in $(C_4H_4)Ni(Al_4Na_4)$ and $0.0033\mathring{A}$ and $0.10459\mathring{A}$ in $(C_4H_4)Ni(Al_4K_4)$ respectively. Note that, for M=K, the Al_4K_4 unit has a substantial BLA with a magnitude close to that of uncoordinated Al_4K_4 (Δr=0.10 $\mathring{A}$). This explains smaller binding energy in the hybrid complex with K^+ as the counter-ion compared to $(C_4H_4)Ni(Al_4Li_4)$ and$(C_4H_4)Ni(Al_4Na_4)$. However, compared to the $Fe(CO)_3$ complexes, these complexes are softer as the HOMO-LUMO gaps are comparatively smaller.

Thus, the synthesis of these sandwich complexes are rationalized in a 3 step reaction of the type: $(C_4H_4)Ni(C_4H_4)$ to $(C_4H_4)Ni(Al_4M_4)$ and finally to $(Al_4M_4)Ni(Al_4M_4)$ [shown in Fig. 8.5].

As we have mentioned, the intermediate complexes, $(C_4H_4)Ni(Al_4M_4)$, are quite stable and can thus be isolated. However, these substitution reactions are mildly endothermic. In this series, the heat of formation is least endothermic for both $(Al_4Na_4)Ni(C_4H_4)$ and $(Al_4Na_4)_2Ni$. So, it is proposed that $(Al_4Na_4)Ni(C_4H_4)$ and $(Al_4Na_4)_2Ni$ are the best candidates for isolation.

8.6 Conclusions

In conclusion, it has been demonstrated that all-metal species like Al_4M_4 can be stabilized by complexation with 3d-transition metals, very similar to its organic counterpart, C_4H_4. The initial poor σ-π separation in Al_4M_4 is lifted on complexation with 3d-transition metals and Al_4M_4, within the complexes, behaves like a pure π-conjugated molecule. Such a mode of stabilization of otherwise unstable and antiaromatic molecules may provide innovative means to crystallize these compounds and utilize for novel molecular-materials applications.

It has also been shown that the all-metal sandwich complexes like: (Al_4M_4)-$Fe(CO)_3$ can be synthesized readily from their organometallic analogue: (C_4H_4)-$Fe(CO)_3$ by direct substitution of C_4H_4 by Al_4M_4. For the full-sandwich complexes, however, $(C_4H_4)_2Ni \rightarrow (Al_4M_4)_2Ni$ conversion is endothermic and cannot be attained in the gas-phase by direct substitution of $2C_4H_4$ by $2Al_4M_4$. The hybrid organic-inorganic intermediate, $(C_4H_4)Ni(Al_4M_4)$ is quite stable and in the presence of additional stabilization factors like solvation, such an intermediate could be isolated.

Bibliography

[1] *Nonlinear Optical Properties of Organic Molecules and Crystals*, D. S. Chemla and J. Zyss, *Academic Press*, (1987).

[2] *Introduction to Nonlinear Optical Effects in Molecules and Polymers*, P. N. Prasad and D. J. Williams (Wiley, New York, 1991).

[3] *Lasers and Nonlinear Optics*, B. B. Laud, (New Age Int, 1991).

[4] *Nonlinear Optical Materials*, ACS Symposium Series 628, Eds. S.P.Karna and A.T.Yeates, Washington DC, 1996.

[5] Optical Nonlinearities in Chemistry, edited by D. M. Burland, *Chem. Rev.*, **94**, *special volume*, (1994).

[6] *Nonlinear Optics*, R. Boyd, 2nd Edition, Academic Press, 2003.

[7] D. J. Williams, *Angew. Chem. Int. Ed. Engl.*, **23**, 690, (1984).

[8] T. J. Marks, M. A. Ratner, *Angew. Chem. Int. Ed. Engl.*, **34**, 155, (1995).

[9] P. A. Franken, A. E. Hill, C. W. Peters, G. Weinrich, *Phys. Rev. Lett.*, **7**, 118, (1961).

[10] (a) M. Goppert-Mayer, *Annu. Phys*, **9**, 273, (1931). (b). W. Kaiser, C. G. B. Garrett, *Phys. Rev. Lett.*, **7**, 229, (1961).

[11] N. Bloembergen, Y. R. Shen, *Phys. Rev. Lett.*, **12**, 504, (1964).

[12] *Topics in Non-Linear Optics.*, Selected papers of N. Bloembergen, Indian Academy of Science, (1982).

[13] W. F. Hagen, P. C. Magnante, *J. App. Phys.*, **40**, 219, (1969).

[14] P. D. Maker, R. W. Terhune, *Phys. Rev.*, **137A**, 801, (1965).

[15] S. Fine, W. P. Hansen, *Appl. Opt.*, **10**, 2350, (1971).

[16] O. Bouevitch, A. Lewis, L. Pinevsky, J. P. Wuskell, L. M. Loew, *Biophys. J.*, **65**, 672, (1993).

[17] D. A. Kleinmann, *Phys. Rev.*, **125**, 87, (1962).

[18] D. A. Kleinmann, *Phys. Rev.*, **128**, 1761, (1962).

[19] V. Moliner, P. Escribano, E. Peris, *New J. Chem.*, 387, (1998).

[20] (a) M. Guillaume, E. Botek, B. Champagne, F. Castet, L. Ducasse, *Int. Jour. Quant. Chem.*, **90**, 1378, (2002). (b) F. Castet, B. Champagne, *J. Phys. Chem. A*, **105**, 1366, (2001).

[21] A. Datta, S. K. Pati, *J. Chem. Phys.*, **118**, 8420, (2003).

[22] J. Zyss, *J. Chem. Phys.*, **98**, 6583, (1993).

[23] G. Alcaraz, L. Euzenat, O. Mongin, C. Katan, I.Ledoux, J. Zyss, M. B-Desce, M. Vaultier, *Chem. Commun.*, **22**, 2766, (2003).

[24] C. Fave, M. Hissler, K. Senechal, I. Ledoux, J. Zyss, R. Reau, *Chem. Commun.*, 1674, (2002).

[25] B. Champagne, D. M. Bishop, *Advances in Chemical Physics.*, **126**, 41, (2003).

[26] S. Di Bella, M. A. Ratner and T. J. Marks, *J. Am. Chem. Soc.*, **114**, 5842, (1992).

[27] R. Custelcean, M. G. Gorbunova, P. V. Bonnesen, *Chemistry - A. Eur. J*, **11**, 1459, (2005).

[28] C-R. Lee, T-H. Tang, L. Chen, Y. Wang, *Chemistry - A. Eur. J*, **9**, 3112, (2003).

[29] H. A. Kurtz, J. J. P. Stewart, K. M. Dieter, *J. Comput. Chem*, **11**, 82, (1990).

[30] K. B. Sophy, S. Pal, *J. Chem. Phys.*, **118**, 10861, (2003).

[31] J. Ward, *Rev. Mod. Phys.*, **37**, 1, (1965).

[32] B. J. Orr, J. F. Ward, *Mol. Phys.*, **20**, 513, (1971).

[33] (a) S. Ramasesha, Z. G. Soos, *Chem. Phys. Lett.*, **153**, 171, (1988) (b) Z. G. Soos, S. Ramasesha, *J. Chem. Phys.*, **90**, 1067, (1989).

[34] (a) S. K. Pati, S. Ramasesha, Z. Shuai, J. L. Bredas, *Phys. Rev. B*, **59**, 14827, (1999). (b) P. C. Jha, S. Ramasesha, *J. Chem. Phys.*, **117**, 2873, (2002).

[35] B. Champagne, E.A. Perpete, J.M. Andre, *J. Chem. Phys.*, **101**, 10796, (1994).

[36] B. Champagne, *Chem. Phys. Lett.*, **261**, 57, (1996).

[37] *Polymers for Second-Order Nonlinear Optics*, edited by G. A. Lindsay, K. D. Singer (ACS Symposium Series 601, Washington D. C., 1995).

[38] E. Hanamura, *Phys. Rev. B.*, **37**, 1273, (1988).

[39] (a) *Theory of Molecular Excitons* by A. S. Davydov (McGraw-Hill, New York, 1962). (b) M. Kasha, *Rev. Mod. Phys.*, **31**, 162, (1959).

[40] (a) *Electronic Absorption Spectra: Geometry of Organic Molecules*, by H. Suzuki (Academic Press, New York, 1967). (b) G. D. Scholes, K. P. Ghiggino, A. M. Oliver, M. N. Paddon-Row, *J. Am. Chem. Soc.*, **115**, 4345, (1993). (c) *Circular Dichroic Spectroscopy: Exciton Coupling in Organic Stereochemistry* by K. Nakanishi; University Science Books, Mill Valley, CA, 1983.

[41] (a) J. Ridley, M. C. Zerner, *Theor. Chim. Acta.*, **32**, 111, (1973). (b) A. D. Bacon, M. C. Zerner, *Theor. Chim. Acta.*, **53**, 21, (1979).

[42] R. J. Buenker, S. D. Peyerimhoff, *Theor. Chim. Acta.*, **35**, 33, (1974).

[43] Z. Shuai, D. Beljonne, J. L. Bredas, *J. Chem. Phys.*, **97**, 1132, (1992).

[44] D. Beljonne, Z. Shuai, J. Cornil, D. dos Santos, J. L. Bredas, *J. Chem. Phys.*, **111**, 2829, (1999).

[45] (a) J. L. Oudar, D. S. Chemla, *J. Chem. Phys.*, **66**, 2664, (1977). (b) J. L. Oudar, *J. Chem. Phys.*, **67**, 446, (1977).

[46] M. Feyereisen, J. Nichols, J. Oddershede, J. Simons, *J. Chem. Phys.*, **96**, 2978, (1992).

[47] F. Sim, S. Chin, M. Dupuis, J. E. Rice, *J. Phys. Chem.*, **97**, 1158, (1993).

[48] (a) F. Spano, J. Kuklinski, S. Mukamel, *Phys. Rev. Lett.*, **65**, 211, (1990). (b) V. Kamalov, I. A. Struganova and K. Yoshihara, *J. Chem. Phys.*, **100**, 8640, (1996).

[49] (a) S. Yitzchaik, G. Berkovic, V. Krongauz, *Adv. Mater.*, **2**, 33, (1990). (b) S. Yitzchaik, S. Di Bella, P. M. Lundquist, G. K. Wong, T. J. Marks, *J. Am. Chem. Soc.*, **119**, 2995, (1997).

[50] (a) J. Zyss, J. F. Nicould, M. J. Coquillay, *J. Chem. Phys.*, **81**, 4160, (1984). (b) B. R. Grubbs, S. R. Marder, J. W. Perry, *Chem. Mat.*, **3**, 3, (1991).

[51] J. D. Bierlein, L. K. Cheng, Y. Wang, W. Tam, *Appl. Phys. Lett.*, **56**, 423, (1990).

[52] S. C. Abrahams, J. M. Robertson, *Acta Cryst.*, **1**, 252, (1948).

[53] J. Donhue, K. N. Trueblood, *Acta Cryst.*, **9**, 960, (1956).

[54] G. F. Lipscomb, A. F. Garito, R. S. Narang, *Appl. Phys. Lett.*, **38**, 663, (1981).

[55] G. F. Lipscomb, A. F. Garito, R. S. Narang, *J. Chem. Phys.*, **75**, 1509, (1981).

[56] B. Tieke, *Adv. Mater*, **2**, 222, (1990).

[57] (a) K. Morokuma, *Acc. Chem. Res.*, **10**, 294, (1977). (b) K. Morokuma, K. Kitaura, *Chemical Applications of Electrostatic Potentials*, P.Politzer, P.; Truhlar, D. G. Eds. Plenum Press, NY, p-215-242, (1981).

[58] S.R. Marder, J.W. Perry, C.P. Yakymyshyn, *Chem. Mater.*, **6**, 1137, (1994).

[59] K. Wu, J. G. Snijders, C. Lin, *J. Phys. Chem. B*, **106**, 8954, (2002).

[60] J. A. R. P. Sarma, J. L. Rao, K. Bhanuprakash, *Chem. Mater.*, **7**, 1843, (1995).

[61] *Chemistry of the Elements*, N. N. Greenwood, A. Earnshaw, 2^{nd} Edition, Butterworth Heinemann, (1997).

[62] (a) R. C. Guedes, P. C. do Couto, B. J. C. Cabral, *J. Chem. Phys.*, **118**, 1272, (2003). (b) C. Zhang, D. L. Freeman, J. D. Doll, *J. Chem. Phys.*, **91**, 2489, (1989). (c) S-Y. Liu, D. W. Michael, C. E. Dykstra, J. M. Lisy, *J. Chem. Phys.*, **84**, 5032, (1986).

[63] *Steriochemistry of carbon compounds*, E. L. Eliel, Mc-Graw Hill (1962).

[64] S. F. Boys, F. Bernardi, *Mol. Phys.*, **19**, 553, (1970).

[65] D. W. Scwenke, D. G. Truhler, *J. Chem. Phys.*, **82**, 2418, (1985).

[66] (a) *Calixarenes Revisited*, C. D. Gutsche, Royal Society of Chemistry, Cambridge, 1998. (b) A. Ikeda and S. Shinkai, *Chem. Rev.*, **97**, 1713, (1997).

[67] (a) M. S. Wong, X. L. Zhang, D. Z. Chen and W. H. Cheung, *Chem. Comm.*, 138, (2003). (b) M. S. Wong, Z. H. Li and C. C. Kwok, *Tet. Lett.*, **41**, 5719, (2000). (c) T. Gu, C. Bourgogne and J.-F. Nierengarten, *Tet. Lett.*, **42**, 7249, (2001).

[68] (a) E. Kelderman, L. Derhaeg, G. J. T. Heesink, W. Verboom, J. F. J. Engbersen, N. F. van Hulst, A. Persoons and D. N. Reinhoudt, *Angew. Chem. Int. Ed. Engl.*, **31**, 1075, (1992). (b) F. Vocanson, P. S. Ferrand, R. Lamartine, A. Fort, A. W. Coleman, P. Shahgaldian, J. Mugnier, A. Zerroukhi, *J. Mat. Chem.*, **13**, 1596, (2003). (c) T. Verbiest, S. Houbrechts, M. Kauranen, K. Clays, A. Persoons, *J. Mat. Chem.*, **7**, 2175, (1997).

[69] E. Brouyere, J. L. Bredas, *Syn. Metals*, **71**, 1699, (1995).

[70] E. Brouyère, A. Persoons, J. L. Brédas, *J. Phys. Chem. A*, **101**, 4142, (1997).

[71] P. D. J. Grootenhuis, P. A. Kollman, L. C. Groenen, D. N. Reinhoudt, G. J. van Hummel, F. Ugozzoli, G. D. Andreeti, *J. Am. Chem. Soc.*, **112**, 4165, (1990).

[72] S. Scheiner, *Hydrogen Bonding. A Theoretical Perspective*, Oxford University Press, Oxford, 1997.

[73] F. H. Allen, S. Bellard, M. D. Brice, B. A. Cartwright, A. Doubleday, H. Higgs, T. Hummelink, B. G. Hummelink-Peters, O. Kennard, W. D. S. Motherwell, J. Rodgers and D. G. Watson, *Acta. Crystallogr. Sect. B*, **35**, 2331, (1979).

[74] K.Tsubaki, Y.Murata, K.Komatsu, T.Kinoshita, K.Fuji, *Heterocycles*, **51**, 2553, (1999).

[75] T. Yamato, F. Zhang, H. Tsuzuki and Y. Miura, *Eur. J. Org. Chem.*, 1069, (2001).

[76] R. Sudharsanam, S. Chandrasekaran, P. K. Das, *J. Mol. Struct.* **645**, 51, (2003).

[77] H. Jiang, A. K. Kakkar, A-M. Lebuis, H. Zhou, G. K. Wong, *J. Mater. Chem.*, **6**, 1075, (1996).

[78] Y. L. Slovokhotov, I. S. Neretin, J. A. K. Howard, *New. J. Chem.*, **28**, 967, (2004).

[79] (a) V. J. Angelico, S.A. Mitcell, V.H. Wysocki, *Anal. Chem.*, **72**, 2603, (2000). (b) D. M. Alloway, *J. Phys. Chem.B*, **107**, 11690, (2003).

[80] S. K. Asha, K. Kavita, P. K. Das, S. Ramakrishnan, *Chem. Mater.*, **11**, 3352, (1999).

[81] P. Gangopadhyay, T. P. Radhakrishnan, *Chem. Mater.*, **12**, 3362, (2000).

[82] A. Datta, S. K. Pati, *J. Phys. Chem . A*, **108**, 320, (2004).

[83] D. Bahulayan, K. J. Sreekumar, *J. Mater. Chem.*, **9**, 1425, (1999).

[84] *Advanced Organic Chemistry: Reactions, Mechanisms and Structure*, Jerry March, 4th edition, (John Wiley and Sons, 1992).

[85] P. Gangopadhyay, T. P. Radhakrishnan, *Angew. Chem. Int. Ed.*, **40**, 2451, (2001).

[86] E. Botek, B. Champagne, M. Turki, J-M. Andre, *J. Chem. Phys.*, **120**, 2042, (2004).

[87] B. Philip, K. Sreekumar, *J. Poly. Sci. A, Poly. Chem.*, **40**, 2868, (2002).

[88] J. O. Morley, P. Pavilides, D. Pugh, *J. Chem. Soc. Faraday Trans.*, **285**, 1789, (1989).

[89] M. G. Kuzyk, *Phys. Rev. Lett.*, **85**, 1218, (2000).

[90] *Molecular Electronic-Structure Theory*, T. Helgaker, P. Jorgensen, J. Olsen (John Wiley & Sons, New York, 2000).

[91] B. K. Rao, P. Jena, *J. Chem. Phys.*, **113**, 1508, (2000).

[92] (a) K. Wu, X. Chen, J. G. Snijders, R. Sa, C. Lin, B. Zhuang, *J. Cryst. Growth*, **237**, 663, (2002). (b) G. Maroulis, C. Pouchan, *J. Phys. Chem. B*, **107**, 10683, (2003).

[93] S. Shetty, D. G. Kanhare, S. Pal, *J. Phys. Chem. A*, **108**, 628, (2004).

[94] A. Kuznetsov, K. Birch, A. I. Boldyrev, X. Li, H. Zhai, L. Wang, *Science*, **300**, 622, (2003).

[95] Z. Chen, C. Corminboeuf, T. Heine, J. Bohmann, P. V. R. Schleyer, *J. Am. Chem. Soc.*, **125**, 13930, (2003).

[96] M. W. Schmidt, K. K. Baldridge, J. A. Boatz et al. *J. Comput. Chem.*, **14**, 1347, (1993).

[97] S. K. Pati, T. J. Marks, M. A. Ratner, *J. Am. Chem. Soc.*, **123**, 7287, (2001).

[98] J. F. Ward, D. S. Elliot, *J. Chem. Phys.*, **69**, 5438, (1978).

[99] P.v. R. Schleyer, C. Maerker, A. Dransfeld, H. Jiao, N. J. R. v. Eikema-Hommas, *J. Am. Chem. Soc.*, **118**, 6317, (1996).

[100] (a) A. Ranganathan, G. U. Kulkarni, *J. Phys. Chem. A*, **106**, 7813, (2002). (b) J. M. Cole, R. C. B. Copley, G. J. McInyre, J. A. K. Howard, M. Szablewski, G. H. Cross, *Phys. Rev. B*, **65**, 125107, (2002). (c) *Atoms in Molecules-A quantum theory*, R. F. W. Bader, Oxford, U. K., (1990).

[101] E. Matito, M. Duran, M. Sola, *J. Chem. Phys.*, **122**, 14109, (2005).

[102] (a) Z. G. Soos, Y. Anusooya Pati, S. K. Pati, *J. Chem. Phys.* **112**, 3133, (2000). (b) S. Kuwajima, Z. G. Soos, *J. Am. Chem. Soc.*, **109**, 107, (1987). (c) Y. Anusooya, A. Chakrabarti, S. K. Pati, S. Ramasesha, *Int. J. Quant. Chem.*, **70**, 503, (1998). (d) Y. Anusooya, Z.G. Soos, *Current Science*, **75**, 1233, (1988).

[103] S. Shaik, P. C. Hiberty, *J. Am. Chem. Soc.*, **107**, 3089, (1985).

[104] Sason. S. Shaik, P. C. Hiberty, J-M. Lefour, G. Ohanessian, *J. Am. Chem. Soc.*, **109**, 363, (1987).

[105] K. Jug, P. C. Hiberty, Sason Shaik, *Chem. Rev.*, **101**, 1477, (2001).

[106] Sason S. Shaik, A. Shurki, D. Danovich, , P. C. Hiberty, *Chem. Rev.*, **101**, 1501, (2001).

[107] P. C. Hilberty, Sason. S. Shaik, J-M. Lefour, G. Ohanessian, *J. Org. Chem.*, **50**, 4657, (1985).

[108] K. Jug, A. M. Koster, *J. Am. Chem. Soc.*, **112**, 6772, (1990).

[109] S. P. de Visser, D. Danovich, W. Wu, S. Shaik, *J. Phys. Chem. A*, **106**, 4961, (2002).

[110] (a) S. P. de Visser, D. Danovich, W. Wu, S. Shaik, *J. Phys. Chem. A*, **104**, 11223, (2000). (b) S. P. de Visser, D. Danovich, S. Shaik, *Phys. Chem. Chem. Phys.*, **5**, 158, (2002).

[111] *Magnetism: Molecules to Materials IV*, Ed: J. S. Miller and Marc Drillon, Wiley-VCH, Weinheim, 2003.

[112] (a) H. C. Longuet-Higgins, L. E. Orgel, *J. Chem. Soc.*, 1969, (1956). (b) *Principles and Applications of Organotransition Metal Chemistry*, J. P. Collman, L. S. Hegedus, J. R. Norton, R. G. Finke, Oxford, (1987).

[113] (a) W. Hubel, E. H. Braye, *J. Inorg. Nucl. Chem.*, **10**, 250, (1958). (b) R. Criegee, G. Schroder, *Liebigs. Annu. Chem.*, **623**, 1, (1959).

[114] Gaussian 03, Revision B.05, M. J. Frisch, G. W. Trucks, H. B. Schlegel, G. E. Scuseria, M. A. Robb, J. R. Cheeseman, J. A. Montgomery, Jr., T. Vreven, K. N. Kudin, J. C. Burant, J. M. Millam, S. S. Iyengar, J.

Tomasi, V. Barone, B. Mennucci, M. Cossi, G. Scalmani, N. Rega, G. A. Petersson, H. Nakatsuji, M. Hada, M. Ehara, K. Toyota, R. Fukuda, J. Hasegawa, M. Ishida, T. Nakajima, Y. Honda, O. Kitao, H. Nakai, M. Klene, X. Li, J. E. Knox, H. P. Hratchian, J. B. Cross, C. Adamo, J. Jaramillo, R. Gomperts, R. E. Stratmann, O. Yazyev, A. J. Austin, R. Cammi, C. Pomelli, J. W. Ochterski, P. Y. Ayala, K. Morokuma, G. A. Voth, P. Salvador, J. J. Dannenberg, V. G. Zakrzewski, S. Dapprich, A. D. Daniels, M. C. Strain, O. Farkas, D. K. Malick, A. D. Rabuck, K. Raghavachari, J. B. Foresman, J. V. Ortiz, Q. Cui, A. G. Baboul, S. Clifford, J. Cioslowski, B. B. Stefanov, G. Liu, A. Liashenko, P. Piskorz, I. Komaromi, R. L. Martin, D. J. Fox, T. Keith, M. A. Al-Laham, C. Y. Peng, A. Nanayakkara, M. Challacombe, P. M. W. Gill, B. Johnson, W. Chen, M. W. Wong, C. Gonzalez, and J. A. Pople, Gaussian, Inc., Pittsburgh PA, 2003.

[115] *The Molecular Orbital Theory of Conjugated Systems*, L. Salem, Benjamin Inc. (1966).

[116] D. H. Paik, D-S. Yang, I-R Lee, A. H. Zewail, *Angew. Chem. Int. Ed.*, **43**, 2830, (2004).

[117] G. F. Emerson, L. Watts, R. Pettit, *J. Am. Chem. Soc.*, **87**, 131, (1965).

[118] J. C. Barobak, L. Watts, R. Pettit, *J. Am. Chem. Soc.*, **88**, 1328, (1966).

[119] G. Wilkinson, M. Rosenblum, M. C. Whiting, R. B. Woodward, *J. Am. Chem. Soc.*, **74**, 2125, (1952).

[120] J. M. Mercero, J. M. Ugalde, *J. Am. Chem. Soc.*, **126**, 3380, (2004).

Other Publications of the author

1. "*Aromaticity in Stable Tiara Nickel Thiolates: Computational and Structural Analysis*" **Ayan Datta**, Neena S. John, G.U. Kulkarni and Swapan K. Pati, *J. Phys. Chem. A (Letters)*, **109**, 11647, (2005).

2. "*Long range electron transfer across π-conjugated systems: Role of electron correlations*", S. Lakshmi, **Ayan Datta** and Swapan K. Pati, *Phys. Rev. B*, **72**, 045131, (2005).

3. "*Proton-Pump Mechanism in Retinal Schiff Base: On the Molecular Structure of the M-State*", **Ayan Datta** and Swapan K. Pati, *Syn. Metals*, **155**, 402, (2005).

4. "*Structure and Electronic Properties of the Watson-Crick Base Pairs: Role of Hydrogen bonding*", Sairam S. Mallajosyula, **Ayan Datta** and Swapan K. Pati, *Syn. Metals*, **155**, 398, (2005).

5. "*Competing Magnetic Interactions in a Dinuclear Ni(II) Complex: Antiferromagnetic O-H....O Moiety and Ferromagnetic N_3^- Ligand*" S.Sarkar, **Ayan Datta**, A.Mondal, D.Chopra, J.Ribas, K.K.Rajak, Sairam S.M. and Swapan K. Pati, *J. Phys. Chem. B (Letters)*, **110**, 12, (2006).

6. "*Stability of Cyclic $(H_2O)_n$ Clusters within Molecular Solids: Role of Aromaticity*" **Ayan Datta** and Swapan K. Pati, *Int. Jour. Quant. Chem.* **106**, 1697, (2006).

7. "*Conformational Preference in Heteroatomic Analogues of Ethane, H_3X-YH_3 (X=B, Al; Y=N, P): Implications of Charge Transfer*", Sairam S. M, **Ayan Datta** and Swapan K. Pati, *J. Phys. Chem. A*, **110**, 5156, (2006).